



UNIVERSITÀ DEGLI STUDI DI CATANIA
FACOLTÀ DI INGEGNERIA

**Dottorato di Ricerca in Ingegneria Elettronica,
Automatica e del Controllo di Sistemi Complessi
XXIII Ciclo**

Florinda Schembri

**Experimental Study for the Control of
Two-Phase Microfluidic Flows**

Ph.D. Thesis

Tutor: Prof. M. Bucolo
Coordinator: Prof. L. Fortuna

2010

To my mother, father and sister

*“Sic ergo per auxilium hominum invicem et
addicionem posterius inventorum
ad inventa prius receperunt omnes
artes et discipline complementum”*

Marsilius

Synopsis

Microfluidics is the science and engineering of systems in which fluid behavior differs from conventional flow theory primarily due to the small length scale of the system.

There are several advantages of scaling down standard laboratory setups from the decimeter scale to the 100 μm scale. One obvious advantage is the dramatic reduction in the amount of required sample. Such small volumes allows for very fast analysis, efficient detection schemes with low samples available. Moreover, the small volumes makes possible to develop compact and portable systems called Lab-on-a-Chip (LOC). LOC systems can be thought of as the natural generalization of the existing electronic integrated circuits and micro-electro-mechanical systems (MEMS).

In the complex scenario of fluid handling in micrometric scale the characterization and control of flows are active areas and several new problems arise especially when we deal with multiphase flow systems. In the complicated and multidisciplinary field of multiphase flow, the development of analytical methods and technological solutions oriented

to the creation of a firm and structured link between models and experimentation, open up the way for the study and characterization of microfluidic processes from a point of view related to system and control issues.

This PhD thesis offers a transversal view through experimental studies for the control of two-phase microfluidic flows. Starting from a brief overview on microfluidic systems and related theoretical issues in Chapter 1 numerical models and computational solutions for time consuming simulations, are considered as preliminary tools for the characterization of spatial-temporal dynamics of unknown microfluidic phenomena. Following these, Chapter 2 presents the materials and methods for the design and fabrication of polymeric optical sensing devices for microfluidic systems. Experimental approaches through original monitoring optical interfaces are discussed in Chapter 3: these monitoring systems offer the possibility to pursue ad-hoc experimentation on such phenomena. This in turn permits the extraction of significant dynamic parameters, fundamental for the validation of preliminary studies and for the creation of innovative experimental models and contributing to the field under study by both methodological and technological point of view. In Chapter 4 a detailed vision on two phase microfluidic phenomena is given through nonlinear time series analysis applied to experimental time series related to optical information extracted from microfluidic processes. In particular, time series related to two-phase (air and deionized water) flow in an in vitro microfluidic serpentine mixer are the basis for embedding space reconstruction, trajectory divergence analy-

sis, and the evaluation of important parameters such as the Maximum Lyapunov exponent and the d-infinite. This study makes possible to capture significant nonlinear features for different experimental conditions, and it is useful for a deep insight on two-phase flow dynamic patterns in complex micro-channels. In particular, through different results on such time series it can be shown how the dynamics of bubbles changes significantly with a variation of the input flow rate (constant and periodic flow rate). The most significant result is the identification of relation maps allowing the classification of the flow dynamics, and opening the way for the control of the bubble flow by signal processing. Finally a mathematical model is proposed in the last Chapter (Chapter 5). The parameters of that model are estimated by an optimization procedure based on standard genetic algorithm.

Contents

1	Two-phase flow in microfluidics	1
1.1	Introduction	1
1.2	The governing equations	3
1.2.1	The continuum hypothesis	3
1.2.2	Conservation of mass and momentum.....	4
1.2.3	Conservation of energy	6
1.2.4	Reynolds number	6
1.2.5	Capillary number	7
1.3	Droplet-bubble formation and breakup.....	7
1.4	Computational fluid dynamics	9
1.4.1	Numerical models.....	10
1.4.2	Parallel computing on GRID architecture	11
1.5	Conclusions	16
2	Technology for miniaturized poly(dimethyl siloxane) optical devices	17
2.1	SU-8 photoresist	18

2.2	Poly(dimethyl siloxane)	19
2.3	Soft lithography	20
2.4	Notions of geometric optics	21
2.4.1	Optical waveguides, mirrors and lenses	21
3	Poly(dimethyl siloxane) micro-optical sensing devices for microfluidics	27
3.1	Monitoring systems: on-chip and off-chip approach	28
3.2	SISO sensing systems	32
3.2.1	Design and fabrication	32
3.2.2	Ray-tracing and experimental light path characterization	37
3.2.3	Dynamic characterization toward flow monitoring ..	40
3.2.4	Conclusions	47
3.3	MISO sensing systems	53
3.3.1	Design and fabrication	53
3.3.2	Static characterization	57
3.3.3	Dynamic characterization	59
3.3.4	Conclusions	67
3.4	Poly(dimethyl siloxane) light splitters	68
3.4.1	Introduction	68
3.4.2	Splitter based on TIR condition	69
3.4.3	Splitter based on partial refraction	70
3.4.4	Ray-tracing and experimental characterization	73
3.4.5	Conclusions	78

4	Nonlinear time series analysis of two-phase microfluidic flows	79
4.1	Introduction	79
4.2	Experimental setup and campaigns	84
4.2.1	Constant input flow	84
4.2.2	Periodic input flow	86
4.3	Dimensionless parameters	90
4.4	Nonlinear time series analysis	91
4.5	Results	94
4.5.1	Constant input flow	94
4.5.2	Periodic input flow	98
4.6	Conclusions	104
5	Two-phase flow identification	107
5.1	Experimental microfluidic two-phase flow	107
5.2	The Chua's oscillator	111
5.3	Microfluidic process identification	114
5.3.1	Synchronization of nonlinear systems	114
5.3.2	Parameters estimation via genetic algorithm	117
5.4	Results	120
5.5	Conclusions	124
6	Concluding remarks	125
7	Acknowledgements	129
	References	131

Two-phase flow in microfluidics

The aim of this chapter is to give a proper understanding of the physical aspects involved in two-phase microfluidic systems: from the theoretical point of view to the development of numerical solutions for the flow field.

1.1 Introduction

A microfluidic system is a network of fluidic channels and other components such as valves and pumps. It typically occupies an area of one square centimeter, with the typical channel widths on the order of 10-100 μm . For comparison, a human hair has a thickness of approximately 50 μm and the diameter of red blood cells are about 7 μm . From a practical point of view even smaller dimensions in a lab-on-a-chip (LOC) are not necessarily advantageous, since the requirement for easier handling as well as measurements can impose some restrictions. However, if the goal is to develop systems for single molecule detection, the sub-micrometer is unavoidable, and one enters the new

and exciting field of nanofluidics [64]. The channels are filled with fluids which can have different properties such as density, viscosity, electrical and thermal conductivity, diffusion coefficients, surface tension etc. Microfluidic flows are readily manipulated using many kinds of external fields (pressure, electric, magnetic, capillary, and so on).

As dimensions shrink, the relative importance of surface to volume forces increases. Such manipulations of flow can be achieved either by forces applied macroscopically, e.g., at appropriate inlets and outlets, or can be generated locally within the microchannel by integrated components. In all cases of two-phase flow microfluidics there are two types of fluids in the system - a carrier fluid and a dispersed phase (or sample). The carrier is usually the transporting liquid while the dispersed phase could be both a liquid or a gas. Both carrier and dispersed fluid are usually placed on the chip through separate reservoirs.

Flows of gas-liquid (*bubble flow*) or liquid-liquid (*droplet flow*) mixed phases are familiar from many macroscopic systems and they represents new trends in bio-analysis through microfluidic systems. When discussing multiphase flows in microdevices there are likewise a myriad of new questions that arise in even simple configurations. In general, the fluid-dynamic response is commonly characterized in terms of the Reynolds and Capillary numbers of the flow. Moreover it is frequently of interest to determine the size of droplets of the dispersed phase [66] or the speed at which the dispersed phase moves relative to the continuous phase. In the perspective of control systems [31], when two different phases are injected the resulting flow can be stable but, al-

ternatively, new phenomena can occur: quasiperiodic [2], chaotic flow [65], ordered or disordered patterns [16] etc. The richness and beauty of hydrodynamic phenomena in microfluidic systems is spawned by the nonlinear term in the Navier-Stokes equation [9].

1.2 The governing equations

1.2.1 The continuum hypothesis

In this thesis all fluids discussed are Newtonian and are treated as continuous isotropic matter (mean molecular fields). The continuum description could however be questioned because of the small length scales present in microfluidics. A way of defining deviations from the continuum description is through the Knudsen number

$$K_n = \frac{\lambda}{L}, \quad (1.1)$$

where λ is the mean-free-path of the molecules and L is a characteristic length scale. L should be chosen to include gradients in the velocity field. For liquids λ is approximately the intermolecular length L_{mol} (bond length). The volume occupied by one molecule L_{mol}^3 is easily approximated, yielding

$$L_{mol} = \left(\frac{M_{mol}}{\rho N_A} \right)^{1/3}, \quad (1.2)$$

where ρ is the density, M_{mol} the molar mass, and N_A is Avogadro's number. For water $\lambda=L_{mol}\approx 0.31$ nm. The Knudsen number identifies

the continuum regimes and the governing equations.

A more intuitive way of justifying the use of the continuum approximation is through a precision criterion. At sufficiently high precision fluids are never continuous. The concept of a continuous velocity field does, e.g., only makes sense for small changes in the center of mass, of a small characteristic volume, due to random fluctuations in velocities. Another example could be to determine the mass density to a certain relative precision r .

1.2.2 Conservation of mass and momentum

Let us consider a volume V on which external forces f act. The equations of motion can be derived by considering the flow of fluid out of the volume, Landau-Lifshitz [35]. Integral conservation laws of mass and momentum are respectively

$$\frac{d}{dt} \int_V \rho dV + \int_S \rho \mathbf{u} \cdot \mathbf{n} dS = 0, \quad (1.3)$$

$$\frac{d}{dt} \int_V \rho \mathbf{u} dV + \int_S [\rho \mathbf{u} (\mathbf{u} \cdot \mathbf{n}) - \boldsymbol{\tau}' \cdot \mathbf{n}] dS = \int_V \mathbf{f} dV, \quad (1.4)$$

where $\mathbf{u}(x,y,z,t)=(u,v,w)$ is the velocity field, ρ is mass density and \mathbf{n} a normal vector directed out of the volume. For Newtonian fluids the stress tensor $\boldsymbol{\tau}'$ is

$$\tau'_{ik} = -p\delta_{ik} + \tau_{ik}, \quad (1.5)$$

where the normal component p is pressure and τ the viscous stress tensor

$$\tau_{ik} = \mu(\partial_k u_i + \partial_i u_k) + \left(\lambda - \frac{2}{3}\mu\right)\partial_l u_l \delta_{ik}. \quad (1.6)$$

The scalars μ and λ are called coefficients of viscosity.

By applying Gauss' theorem to Eqs.1.5 and 1.6 we obtain respectively the equation of continuity and the Navier-Stokes equation

$$\frac{D\rho}{Dt} = -\rho\nabla \cdot u, \quad (1.7)$$

$$\frac{\rho Du}{Dt} = -\nabla\rho + \nabla \cdot \tau + f, \quad (1.8)$$

with $D/Dt = \partial_t + u \cdot \nabla$ being the convective derivative.

In case of incompressible fluids $D\rho/Dt=0$ and Eqs. 1.7 and 1.8 simplify to

$$\nabla \cdot u = 0, \quad (1.9)$$

$$\frac{\rho Du}{Dt} = -\nabla p + \mu\nabla^2 u + f. \quad (1.10)$$

while the viscous stress tensor becomes

$$\tau_{ik} = \mu(\partial_k u_i + \partial_i u_k). \quad (1.11)$$

Combining the Navier-Stokes equations and the equation of continuity we have four equations and four unknowns. In general, finding an exact analytical solution for these equations is very difficult.

1.2.3 Conservation of energy

In viscous flows the energy is dissipated through irreversible processes into heat. The temperature of the system will increase until an equilibrium between heat generation and heat transport is obtained. The conservation of energy is given by, Landau-Lifshitz [35],

$$\partial_t \left(\frac{1}{2} \rho u^2 + \rho e \right) = -\nabla \cdot \left[\rho u \left(\frac{1}{2} u^2 + h \right) - u \tau - k \nabla T \right], \quad (1.12)$$

Here e and h are respectively internal energy and enthalpy per unit mass, $\kappa(T)$ thermal conductivity and T temperature. The left hand side of Eq. 1.12 is the rate of change in mechanical and thermal energy respectively, while the right hand side is the divergence of the energy flux. The first term in the brackets represents the mass transfer due to the fluid motion (kinetic energy $\rho u^2/2$ and enthalpy ρh , per unit volume); the second term is the internal friction due to the viscosity. The last term represents the heat conduction due to temperature gradients.

1.2.4 Reynolds number

A measure for the ratio between inertial and viscous forces is the Reynolds number defined as

$$Re = \frac{Lu}{\nu}, \quad (1.13)$$

where L and u is a characteristic length and velocity, respectively, while ν is the kinematic viscosity. The Reynolds number at the transition between laminar and turbulent flow is of the order 10^3 , depending

on the geometry and type of flow. For a Poiseuille flow in a tube the critical Reynolds number $Re_{crit} \geq 2000$. In microfluidics the flow is almost always laminar due to the micro length scales $L \approx 100 \mu\text{m}$, small velocities $u \approx 1 \text{ mm/s}$ and kinematic viscosity $1.00 \times 10^{-6} \text{ m}^2/\text{s}$ yielding a Reynolds number of $Re \approx 0.1$.

1.2.5 Capillary number

Between immiscible fluids a surface tension γ affects the dynamics of the free surface. Capillary number is a dimensionless parameter found whenever interfacial stresses compete with viscous stresses

$$Ca = \frac{\eta u}{\gamma}, \quad (1.14)$$

where u is the average flow velocity, η is the dynamic viscosity and γ is the surface tension between the two phases. In microscale, the capillary number is small and surface effects are dominant. Thus it plays a crucial role in the characterization of multi-phase flows.

1.3 Droplet-bubble formation and breakup

New trend in microfluidics is the use of droplets/bubbles in analytical systems [27]. Droplets/bubbles of sample fluids can be dispersed in microchannels using the instability between two immiscible phases. Thus the basic condition for droplet/bubble formation is that sample fluid and the carried fluid are immiscible. The behaviour of droplet formation and the size of the dispersed droplet are determined by two

parameters: the capillary number (Ca) and the fraction of the sample flow. This is defined as the ratio between the volumetric flow rate of the sample fluid and the total volumetric flow rate V_{fluid} of both phases:

$$r = \frac{V_{sample}}{V_{sample} + V_{carrier}}. \quad (1.15)$$

At low capillary numbers, the droplets of the sample flow are formed at the junction [43]. The size of the droplets and the distance between them are reproducible. For the same fraction r , increasing the capillary number decreases the droplets size. Increasing the capillary number further a laminar side by side flow occurs beyond the junction before separating in droplets [43]. For droplet/bubble systems controlled by external flows, the design of the channel geometry is used to control the forces that create, transport, split and fuse droplets/bubbles [54]. The basic physical mechanism that breaks a liquid jet into droplets under the action of surface tension is the Rayleigh-Plateau instability. A detailed review of this instability is given in [19]. The instability is caused by pressure fluctuations inside the liquid due to small variations in the local curvature; such variations grow to eventually break the liquid film into drops, through a so-called finite time singularity. Standard processes use high shear forces to generate droplets, e.g. by rotor-stator, ultrasonic or high-pressure homogenizing systems. Droplets/bubbles can also be generated by exploiting microchannel geometries, such as the surface tension controlled break-off issued from tiny orifices [22]. In general, several microfluidic methods exploiting

different geometries and temporal dynamics of input flows for the production of droplets/bubbles have been presented [54].

1.4 Computational fluid dynamics

By about 1990 Computational Fluid Dynamics (CFD) had become an indispensable tool in almost every branch of science and engineering: aerospace, marine, automobile, electromagnetism, environmental, nuclear power, weapons, weather forecasting, oceanography, space physics, cosmology, bioengineering, micro- and nano-technology etc... The effectiveness of CFD in each of these areas increased by three or four orders of magnitude per decade. The gains were about equally due to hardware (bigger and faster machines) and software (operating systems, algorithms). CFD involves the numerical solution of sets of Partial Differential Equations (PDEs), which have many idiosyncracies. There is not yet (and probably never will be) any universal method of solution, and all methods, except for the very simplest problems, require some expertise on the part of the user.

In the case of microfluidic systems CFD allows respect to experiments to have very detailed information, powerful visualization on very small scales both in space and time while the main drawbacks are: modeling of uncertainties, limited accuracy by available resources, problems with disparate length/time scales and very time consuming simulations. In the following it is reported an example of two-phase microfluidic flow

obtained through numerical simulation on a GRID infrastructure (Consorzio Cometa, INFN, Catania, Italy) [26].

1.4.1 Numerical models

There are two main numerical methods for simulating multiphase flow in microfluidics: interface tracking methods and interface capturing methods [13]. The latter class of methods are ideal for simulating immiscible two-phase systems.

Interface tracking methods

In interface tracking methods (or sharp interface methods) the computational mesh elements lie in part or fully on the fluid-fluid interfaces. Such methods, including boundary integral methods, finite element methods, and immersed boundary methods, are a very accurate instruments for simulating the onset of breakup and coalescence transitions but encounter difficulties in simulating through and past the transitions.

Interface-capturing methods

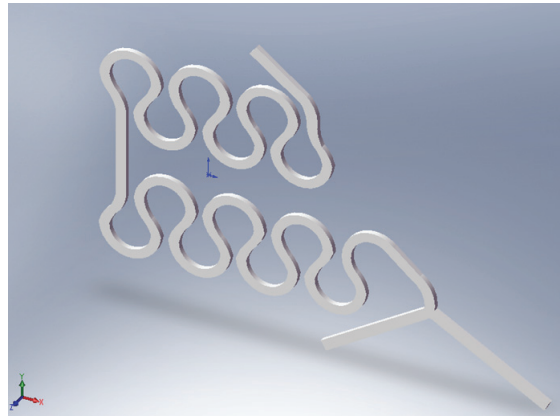
Simulations of breakup and coalescence transitions using interface capturing methods, i.e lattice Boltzmann and lattice gas, constrained interpolation profile, level set, volume of fluid, coupled level set and volume of fluid, partial miscibility-model, and phase field methods, do not require mesh cut and connect operations because the mesh elements do not lie on the interface, but rather the interface evolves through the mesh. The fluid discontinuities (e.g. density, viscosity) are smoothed and the surface tension force is distributed over a thin layer near the

interface to become a volume force (surface tension being the limit as the layer approaches zero thickness). Interface capturing methods are then ideal for simulating breakup and coalescence in immiscible two-phase microfluidic systems (and moreover the effect of surfactants) and for three or more fluid components.

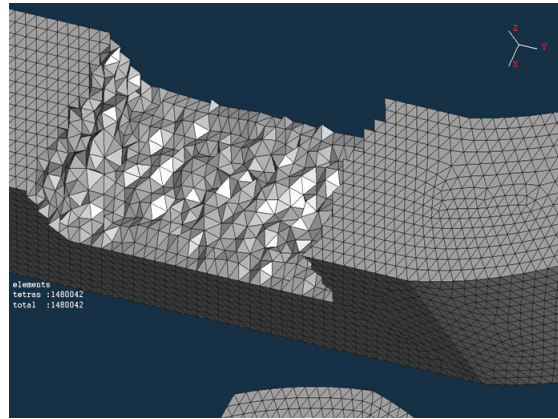
1.4.2 Parallel computing on GRID architecture

Numerical modeling of a two-phase (air/water) flow in a serpentine micromixer is considered. Computational Fluid Dynamics (CFD) solution are exploited, allowing a detailed and quantitative characterization of spatial fluid dynamics as the bubbles' formation process. Because of the two phase flow numerical simulations were very time consuming on a single calculator due to the hardware restrictions a spatial domain parallelization has been necessary. Fluent (Ansys, 6.3.26,[20]), a well parallelized CFD software, has been used on a GRID infrastructure (*computational grid*) with the advantage of reducing the computing time by mesh and data partitioning on 48 subdomains (48 cores). The Fluent-GRID environment has been chosen to model the two phase flow process (air-water) in a serpentine micromixer (see Fig. 1.1(a)). Fluent software can be exploited for parallel processing involving the use of the message passing interface (MPI) and mesh partitioning. Thus Fluent software is adaptable to run on GRID architecture with an Infini-Band interconnection network.

The modeling process of the two phase flow in the serpentine involves several steps: from geometry creation to codes development for



(a)



(b)

Fig. 1.1. (a) Solution domain. (b) The superficial and volumetric mesh used in the model.

the submission on GRID of the parallel CFD jobs.

Spatial Domain and Mesh

A fundamental step toward the numerical simulation has been the 3D CAD of the solution domain. The serpentine mixer is 121 mm long between confluence and outlet and it has a $640 \times 640 \mu\text{m}$ section. The serpentine geometry has been created through the software SolidWorks

(Dassault Systmes, SolidWorks Corp.). A 3D view of the serpentine geometry is show in Fig. 1.1(a). Mesh creation is particularly delicate because it determines the accuracy of the flow pattern results. An ad hoc mesh of the micromixer has been set up by means of the software Beta CAE ANSA (Beta CAE Systems SA). In the case here considered 302.820 triangular elements have been chosen as superficial mesh of the micro-serpentine, while an unstructured CFD tetrahedral mesh of 2.724.041 elements as the volumetric mesh. In Fig. 1.1(b) an hollow into the serpentine mesh shows the internal tetrahedral mesh. After mesh definition, the boundaries have been differenced (air inlet, water inlet, etc..) by adding an identification number.

Numerical Model

The numerical model involves the Navier Stokes equation to model the laminar flow, and the direct numerical Volume of Fluid (VOF) method to model the free surface of the two immiscible fluids (water and air) in the microchannel by solving a single set of momentum equations and tracking the volume fraction of each of the fluids throughout the domain. In the VOF method, the fluid location is recorded by employing a volume-of-fluid function which is defined as unity within one fluid regions and zero elsewhere. Constant velocities with linear profile have been applied at the two inlets: 0.05 m/s for water and 0.1 m/s for air. These input velocities determine bubbles formation. The other boundary conditions have been set as: pressure outlet, wetted and not wetted walls (air inlet). According to Courant number limitations the time step has been fixed to 0.0002. The Courant number is the ratio of a

time step value to a cell residence time leading the numerical stability of the algorithm.

Implementation on GRID

For submitting the job on GRID a Fluent journal file has been created mainly to read the case and data files of the model and set automatically the time step value and the number of iterations in the successive Fluent launch on GRID. Several files have been necessary to solve the microfluidic two phase flow model on GRID.

One of the most important is the bash script file called *mpi.pre.sh*. It is an input file created in order to submit and control the Fluent job on the worker nodes. In particular the *mpi.pre.sh* script has the objective of preparing machine file for Fluent, launch other scrip to support the job, copy on the Worker Nodes (WN) the Fluent case and data files, launch Fluent and waiting for job results. Thanks to this script the results (images, case-data files) are automatically uploaded in the storage elements (SE). Another fundamental file to job submission is the JDL file. In particular, this file allows to set the number of cores, required for the simulation, on the Computing Element (CE).

Results

In the case here considered, 48 cores have been chosen to speed up the simulation process taking 22 s for one time step compared to 5 minutes needed on a Intel Core2 Quad, 2.4GHz. The processed iterations have been 800.000, having in total 8 s of simulation. The simulation output amounts to about 50 GB of data that have been downloaded on the user interface (UI) space and then post-processed. Several variables and

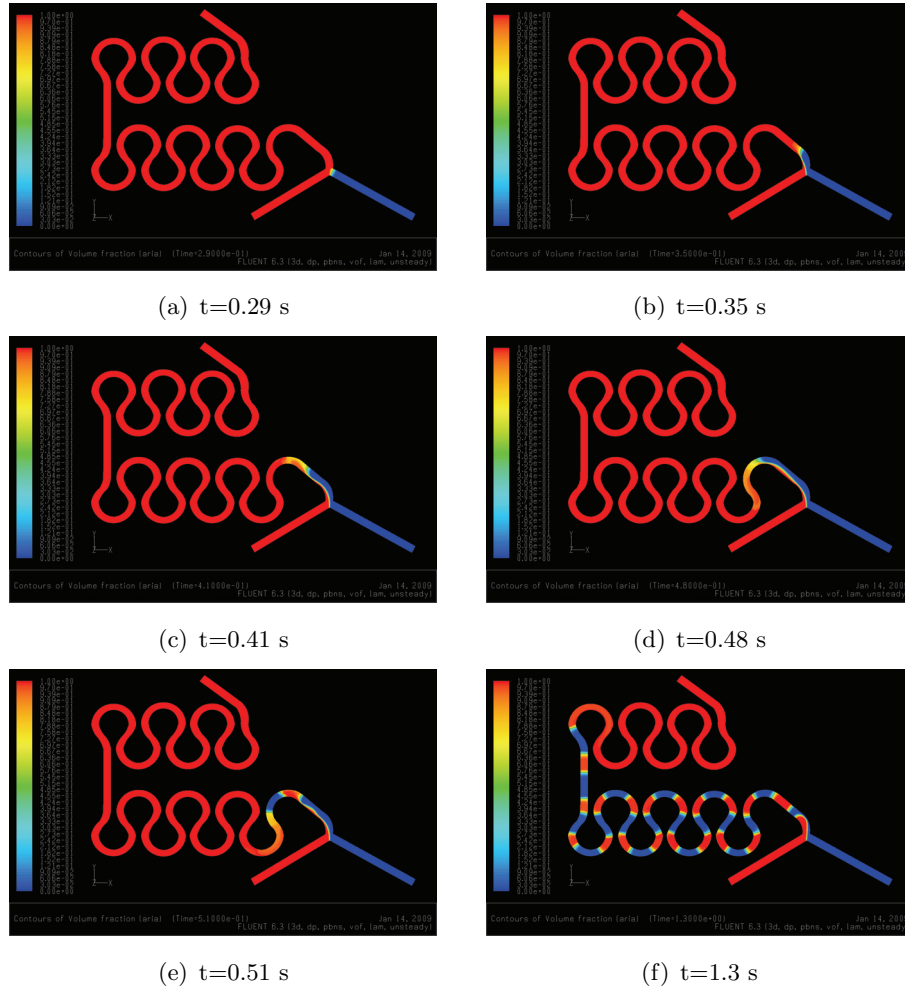


Fig. 1.2. Coutour of air fraction in the two-phase flow simulation.

parameters could be extracted from the simulation results such as air and water contours, velocity field, stream line flux etc. A significant result is shown hereafter: the process of bubbles' formation.

The process of bubbles' formation is nonlinear because it involves a flux instability between the two immiscible phases. In Fig. 1.2 are shown some snapshots of the air contours at different times. It can be possible

to see that air stream elongates, then develops a neck until the break up. The image in Fig. 1.2(f) in particular shows the flow pattern of the created bubbles.

1.5 Conclusions

In this chapter we have explored the governing equations of microfluidic systems derived from the fundamental equations describing the rate of change of the flux densities of mass, momentum and energy. Moreover the main parameters (Reynolds and capillary number) are detailed. A brief overview on the physical processes involved in bubbles/droplets formation is given.

The nonlinear term of the Navier-Stokes equation make its mathematical treatment complex and difficult. In fact the solutions of the equation have never been fully characterized, this fact open the way to numerical simulations. A numerical approach on a parallel architecture (GRID) is described for time consuming simulations involving the analysis of two-phase flow on a complex microfluidic channel. A Fluent-GRID environment has been exploited considerably improving the time performance and allowing complex analysis on a micro-channel with 3D domain.

Technology for miniaturized poly(dimethyl siloxane) optical devices

Technologically polymers are interesting because they offer a fast and cheap way of producing microsystems, as can be sensors, actuators, chips for microfluidics, etc. Substituting silicon as structural materials for polymers and building polymer based micro-systems, will allow a drastic reduction of the production cost, together with a huge increase of the technological flexibility. The allowed technological flexibility is of fundamental importance in the emerging field of microfluidic based applications. In this chapter the main aspects for the design and the technology involved in the production of micro optical systems for monitoring microfluidic flows, are illustrated. The complete designs and functionality of these innovative devices are detailed in Chapter 3.

2.1 SU-8 photoresist

SU-8 is a negative tone photoresist based on EPON SU-8 resin and it is the material used to create the mold for the soft lithography procedure explained in the following paragraphs.

The resist has two important properties suited for ultra-thick applications needed for microfluidics. First its low molecular weight; which implies that it can be dissolved in a variety of organic solvents to form very high concentrations mixtures. Second, the layer has very low optical absorption in the near-UV spectrum. This low optical absorption implies that the light is able to reach the bottom part of the resist layer. Additional, during exposure, the refractive index increases, creating a waveguide effect and hence achieving the vertical walls. The basic step to create the mold are in synthesis:

- Preparation of the substrate;
- Spin coating;
- Relax;
- Soft-bake;
- Exposure;
- Post exposure bake;
- Relax;
- Development;
- Hard-bake.

2.2 Poly(dimethyl siloxane)

Poly(dimethyl siloxane)(PDMS) is a commercially available clean room compatible type of silicone rubber with a wide range of applications in microfluidic systems, as can be sensors, microvalves, microfluidic channels, etc. PDMS has some unique properties, as for example an extremely low T_g of around $-125\text{ }C^\circ$, which yields a ultra low elastic modulus, ranging from 100 kPa and 5 MPa. As it is an incompressible fluid, its Poisson's ratio is 0.5, which implies a huge amount of possible applications. Its coefficient of thermal expansion is very high as well as its biocompatibility and its chemical inertness. For fluidic devices results very interesting given the fact that, although in principle is hydrophobic, it is possible to oxidize its surface, generating an hydrophilic material and also allowing two pieces of material to bond between them.

In order to obtain PDMS, it is possible to acquire directly solid films already prepared or to prepare the elastomer by mixing a PDMS prepolymer, e.g. Sylgard 184 (Dow Corning) with its curing agent in a given portion, for example 10:1 in volume, although it can be different. After the mixing, some air bubbles are present in the viscous fluid, so a vacuum procedure is usually performed in order to get rid of them. By placing the mixing at relative low pressure, e.g. 0.1 mbar, the gas is extracted. Once the material is free of bubbles, it is poured on the substrate to be replicated and it is cured at high temperature during some time. The temperature and time depend one on the other, i.e. the

higher the temperature the shorter the required time. Some standard values are $80\text{ }C^{\circ}$ and 20 minutes. After curing, PDMS is ready to be used. PDMS is resistant to high temperature and it can present good optical properties. On the other hand it is difficult to repair and it is relatively difficult to bond (it need for instance surface treatment).

2.3 Soft lithography

Soft lithography provides an alternative set of techniques for micro-fabrication. It does not have the limitations of using material that are photosensitive, and it can be applied to non-planar surfaces. Soft lithography includes a suite of techniques that use physical contact between a topological patterned stamp and a substrate. The stamp is made of soft materials, hence it is not rigid. The most used material are the elastomer poly(dimethyl siloxane) and silicon rubbers. The fabrication of the stamp is done by pouring a prepolymer of the elastomer onto a master having relief structures on its surface. The prepolymer is then cured and subsequently peeled off. The stamp is usually used to replicate its relief structures in a polymeric material. This can be made by pouring the polymer onto it to generate a replica or transfer the relief onto a substrate after removing the excess of polymer. All these techniques are then based on the use of the stamp as a mould, transferring the shape into a polymer or prepolymer that becomes solid and stiff after curing, exposing to UV, etc... Soft lithography techniques have five characteristics that are useful for the microfabrication of functional de-

vices:

- They are fast. It often takes less than 24 hours to go from a design to a prototype device.
- They are inexpensive: do not require the use of expensive equipment or infrastructure.
- They allow the patterning of a range of functional materials (metals, polymers, molecules, and biological organisms) directly onto surfaces.
- They can be used to pattern non-planar surfaces.
- They are simple to use and do not require specialized training.

On the other hand, reproducibility and number of defects are two of the main drawbacks that this technique presents.

2.4 Notions of geometric optics

In this section the main optical laws used for the design of waveguides, mirrors and lenses of PDMS micro-optical monitoring systems, treated extensively in Chapter 3, are explained giving an introduction to how controlling light.

2.4.1 Optical waveguides, mirrors and lenses

An optical waveguide can be defined as a dielectric structure that transports an electromagnetic wave with a wavelength in the UV, visible, or infrared range. The confinement of light in a certain region happens if the light travels in a medium of high refractive index (core), which is surrounded by a material of low refractive index (cladding) that acts

like a trap for the light. In this way the light will be driven by total internal reflection (TIR). The light propagation, governed by Maxwell's equations, happens in discrete modes depending on the waveguide dimension. A single-mode waveguide has a dimension in the same order of the wavelength of the light traveling inside it [55]. In this thesis (see Chapter 3), multimode waveguides will be considered, where simple ray tracing can be used for describing the light propagation. A straight waveguide with a refractive index n_1 , surrounded by a cladding of refractive index n_2 is considered. In the case of the designed optical microsystems we use PDMS ($n_1=1.41$) as core material and air as cladding ($n_2=1$).

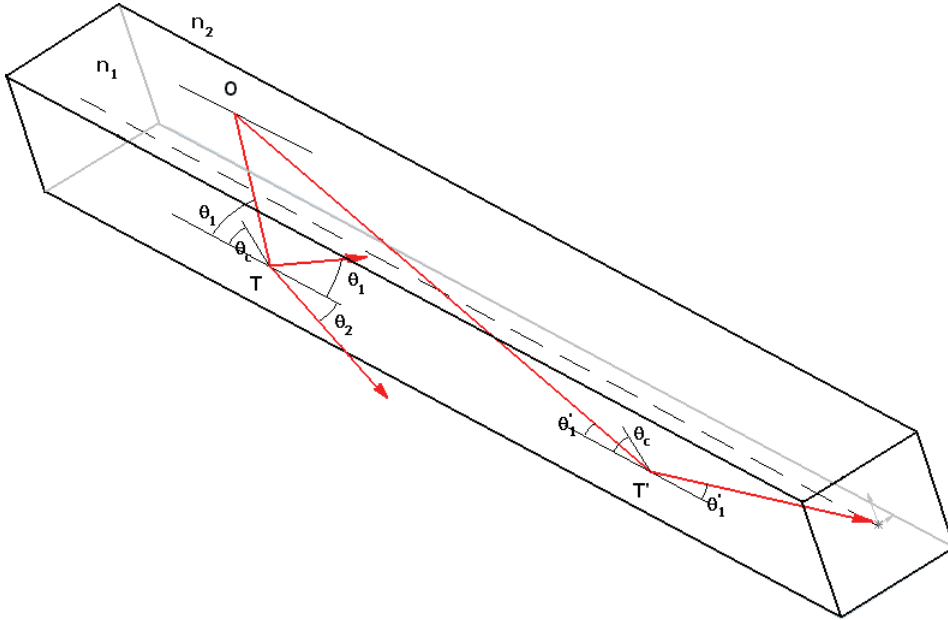


Fig. 2.1. Schematic three-dimensional view of waveguide and propagation of light at different angles.

In Fig.2.1 a straight waveguide with a refractive index n_1 , surrounded by a cladding of refractive index n_2 is considered. A ray that originates at point O at the interface of the waveguide making an angle θ_1 with the waveguide axis will touch the opposite interface at a point T and it will be refracted forming an angle θ_2 with the waveguide axis. The relation between the angles of refraction and incidence is governed by the Snells law

$$n_1 \cos(\vartheta_1) = n_2 \cos(\vartheta_2) \quad (2.1)$$

At certain values of θ_1 and θ_2 will be zero. This occurs when $\theta_1 = \theta_c$, where θ_c is the critical angle.

$$\theta_c = \cos^{-1} \left\{ \frac{n_2}{n_1} \right\}. \quad (2.2)$$

The incident ray will be totally internally reflected if $0 \leq \theta_1 \leq \theta_c$ and is partly reflected and partly refracted if $\theta_c \leq \theta_1 \leq \pi/2$. It is obvious that for having an efficient waveguide the light must travel at angles smaller than the critical angle to achieve the so called total internal reflection (TIR) and this is mainly a limitation to the modes that can be coupled into a waveguide. For the design of mirrors the same theoretical concept discussed for waveguides hold. As for lenses (see Fig.2.2) ray optics theory can be used to estimate the behavior of the light from a light source through media of different refractive indices. Considering the radius (R) of a lens, the radius (r) and numerical aperture (NA) of the light beam, the relative position between the light source and the lens

(x_0) , the refractive index (n_1) of the material used between the light source and the lens, and the refractive index of the medium in which the light propagates after the lens (n_2), the theoretical trajectory of the light can be estimated by

$$\theta_2 = \frac{n_1}{n_2}\theta_1 - \frac{n_2 - n_1}{n_2 R}y \quad (2.3)$$

where θ_1 is the angle created by the light source with the x axis and y is the height at which the ray meets the lens. The height y can be calculated considering the intersection between the line representing a specific ray and the circle representing the lens, while the angle θ_2 can be calculated knowing the numerical aperture of the light source and the refractive index of the plug.

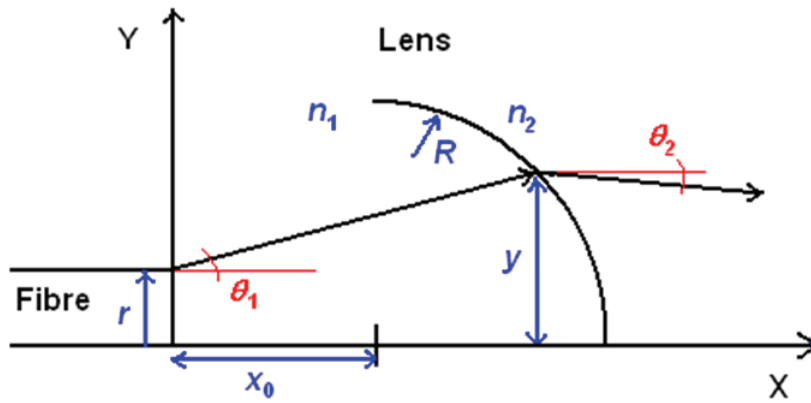


Fig. 2.2. Two dimensional representation of light propagating from a source with a specific numerical aperture through a lens.

Though, we must consider that ray optics is an approximate theory which is based on having paraxial rays, that means the light travels at

small inclinations (such that $\sin(\theta) \approx \theta$) around an optical axis about which the optical components (in our case the lens) are centered. According to the paraxial approximation for a plane convex lens the focus length will be

$$f = \frac{R}{n_{lens} - 1} \quad (2.4)$$

The deviation from paraxial approximation will result in the formation of a caustic curve that will focus within an area more than a point giving aberration [55].

Poly(dimethyl siloxane) micro-optical sensing devices for microfluidics

In this chapter it is described the design and miniaturization of a Single-Input-Single-Output (SISO) polymeric optical interface for flow monitoring in biomicrofluidics applications based on poly(dimethyl siloxane) technology, providing optical transparency and compatibility with biological tissues. Design and ray tracing simulations are presented as well as device realization and optical analysis of flow dynamics in microscopic blood vessels. Optical characterization of this polymeric micro-interfaces in dynamic experimental conditions provides a proof of concept for the application of the device to two-phase flow monitoring in both in vitro experiments and in vivo microcirculation investigations. The SISO optical system it is then extended to Multi-Input/Single-Output (MISO) systems toward advanced monitoring systems that guides and merges the spatially distributed flow information into a single output signal, which maintains memory of the spatial coordinates by using wavelengths as fingerprints of distributed locations in

the microfluidic channel. Moreover the possibility of efficient light splitting opens the way to complete PDMS micro-optical monitoring systems.

3.1 Monitoring systems: on-chip and off-chip approach

Phenomena occurring in multiphase microfluidic devices, such as DNA processing, particle encapsulation, mixing of fluids, or analysis of in vivo conditions, such as red blood cell (RBC) flow, platelet motion in the microcirculation, involve the visualization and monitoring of cells, gas bubbles, or liquid droplet transported through micrometric channels. Optical techniques play a crucial role in these biochemical analysis [10][51][17][34][37][38]. The need therefore arises for accurate and high sensitivity two-phase flow characterization at the microscale level, requiring noninvasiveness and real-time performance and good spatial resolution [37][38][17]. The use of bulky microscopes to acquire images and data of the flow in microfluidic device is expensive and unefficient for high sensitivity purposes and low limit of detection for both absorbance, fluorescence and chemilluminescence measures [34].

In the past methods for flow detection in microfluidic systems have been introduced. For example the dual slit methodology exploits the optical contrast between different phases of the fluids, or between fluids and particles, and is used for measuring the transit time between two optical windows of particles (i.e., RBCs) or, in general, of two-phase

fluids [63]. It yields flow velocity on a single channel/vessel with a spatial resolution, which is flexible and dependent on the characteristics of the optical setup. Moreover, compared to other methodologies, the implementation of the dual-slit method is based on a relatively simple experimental setup, involving optical magnification, detection (by means of photodetectors), and processing units performing cross-correlation between signals; this renders it suitable for real-time velocity evaluation in *in vitro* devices and in experimental animal preparation [48]. Methods generating 2D profiles of microfluidic flow are also considered suitable for characterizing spatio-temporal dynamics in the microfluidics environment. An example of these techniques based on the Doppler principle, enhanced high resolution-laser Doppler imaging, performing flow measurements using the principle of light scattering and the spectral analysis of the scattered signal [36][25]. An alternative method is particle imaging velocimetry (PIV) algorithms, a CPU-based implementation applied to digital images acquired by a high speed digital camera. PIV assesses particle flow velocity profiles and has been used extensively in experimental fluid mechanics [57]. Real-time image processing based on parallel analog processing (cellular nonlinear networks) has also been found to be suitable for microfluidic environment characterization [47]. These techniques are based on optical access to the fluid under study: They require optical magnification interfaces, i.e., standard microscopy, in order to obtain the highest spatial and temporal resolution to match with the dimensions of optic sensors. They may also need a complex experimental setup in order to obtain optical

alignment to the microcirculation field and to allow simultaneous measurements, such as oxygen distribution, together with morphological analyses, such as vessel network functional density and dynamic vessel diameter.

A new concept of optical sensing is developing toward the reduction of the equipment, the complexity and more important minimizing the amount of external (off-chip) macroscopic and expensive components [50].

Costs' reduction is another issue and bicompatible and high integrated microfluidic systems based on Poly(dimethyl siloxane) layers and optical fibers seem the starting point for low-cost photonic Lab on a Chip systems. In particular Poly(dimethyl siloxane)-based microsystem have been developed for the flexible and robust nature of Poly(dimethyl siloxane), its high light transmittance over a large frequency range and its relative low cost [18]. Thus using micro-optical system is possible to increase the level of automation and integration in the design of complex self-sufficient microfluidic platforms. It has been proved that very accurate PDMS microstructures such as microlenses and waveguides are possible and have the advantages of low light attenuation [11][12]. New technological solutions for flow optical detection based on polymeric micro-optics were approached in previous works [37][38] to reduce the size of the entire experimental setup as well as to improve the performance of optical spectroscopy detection and at the same time to increase the intensity of fluorescent response. A compact and complete PDMS system (monolithic integration of lenses, alignment of optical

fibers and microfluidic device, optical readout) for absorption and pH measures was designed and tested in [37][38]. Another issue is full integration of light sources and photodetections. It has been demonstrated that droplets size, droplets frequency and shape can be efficiently detected in a microfluidic system with photodiode-based detection of light intensity [44]. This approach based on time series analysis is a powerful tool for providing a feedback signal to the droplets formation process toward automatic analysis.

The optical devices, here proposed, are all based on off-chip detection approach in microfluidics. The designed micro-optical systems comprise an assembled of micro-optical components (lenses, mirrors and waveguides) that control efficiently the light path. The modular optical design and technological solution proposed here are suitable for a wide range of microfluidic geometries and applications. The SISO devices consist in disposable polymer-based optical interfaces that may be applied directly to the microfluidic process in both *in vivo* and *in vitro* experimentation, in order to permit single channel/vessel flow characterization [50]. They exploit the optical properties of PDMS and also they integrate microgeometries for optical fiber insertion. Moreover, such a design, compared to others, responds to the practical need for a disposable optical interface which, superimposed on the microfluidic sample, either *in vitro* or *in vivo*, allows other optical measurements to be performed simultaneously without interfering with their experimental setup.

As for MISO devices the novelty is the possibility to obtain a single

multi-wavelength optical signal offering real-time information about spatially distributed flow profile through a compact and portable system. Also as optical detection systems they could be integrated in the microfluidic device for velocimetry calculation, such as the dual slit methodology or the novel calculation based on Fourier transformation [42]. The off-chip approach allows the use of the optical devices as portable systems also for in-vivo system monitoring (microcirculation study). Thus the micro-optical interfaces here presented could be also considered in general a valid alternative to macro-optical systems (microscope) toward portable and cheap optical instrumentation for microfluidic device (on-chip approach). It is worth to notice that the designs of the micro-optical components and devices presented in this chapter can be used to monitoring a wide range of microfluidic two-phase flow systems.

3.2 SISO sensing systems

3.2.1 Design and fabrication

The aim of this first design is to detect optical information in microfluidic systems and to leave the area under observation accessible to other types of optical processing and analysis. The devices are based on a low cost material, PDMS, known for its biocompatibility and high optical transmittance in the UV-near infrared (UV-NIR) region. The design of the micro-optical interface (see Fig. 3.1) includes an optical slit (S), a mirror (M) angled at 40° , a PDMS/air total internal reflection (TIR)

waveguide (WG), a biconvex lens (FL), and a fiber optic self-alignment system (F1), as described in Fig. 3.1(a). Air cylinders, called here as pillars (P), surround the entire device in order to protect the functional part, consisting in the slit, mirror and waveguide, from environmental light, while providing it with mechanical robustness. Such a configuration would allow to work at any angle of light direction. The air/PDMS structure of the devices makes them transparent and, therefore, makes both the microfluidic area for the in vitro and the live tissue optically accessible by simply changing the observation focal plane. Moreover, design variations are shown in Figs. 3.1(b)(d). The structure has two functional configurations (Fig. 3.2(a)) allowing light guiding for bidirectional interaction as detection (sensors) or as source (illuminating device) interface between the device and the microfluidic environment. The first configuration, here called as outwav (OW), is the interface between the microfluidic flow target to be analyzed and the detectors (Fig. 3.2(b)). The second functional configuration, inwav (IW), converts the device into an interface between a light source and a target (Fig. 3.2(c)).

OUTWAV

The optical information is generated by a light source (F2) that backlights the area under analysis and is captured inside the slit ($S=70 \mu\text{m}$). Light is reflected by the micro-air-mirror (M) angled at 40° and is confined into the waveguide (WG), which directs it toward the output fiber optic insertion (F1) passing through a focusing biconvex lens (FL) to correct the numerical aperture (NA) of the rays and make them

suitable for fiber optics detection (F1).

INWAV

The light can be emitted by any source and then inserted through fiber optics into the alignment system insertion (F1). The light is guided through the waveguide (WG) and then mirrored (M) in the direction of the targeted microfluidic system through the slit (S).

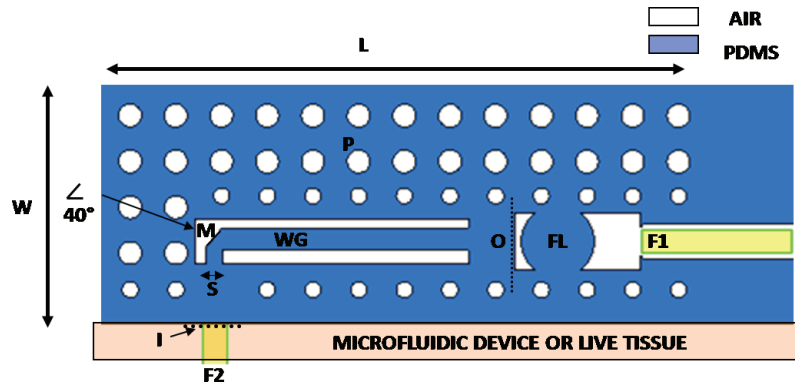
Design variations

In the detection configuration (OW), the slit size can be designed to regulate the amount of light that the device can capture. Figures 3.1(b) and (c) represent two variations in the size and geometry of the basic slit design in Fig. 3.1(a). In these variations, the slits are smaller [(b) $S=25 \mu\text{m}$ and (c) $S=50 \mu\text{m}$] and present a tilted structure at an angle of 40° in order to be selective and to reflect away the beam of light not coming from the microfluidic spot to be measured. Further design variations are possible for the OW configuration, in order to optimize the collection of light by the focusing lens (FL) and by the fiber optic positioned in the alignment system (F1). The orientation of this lens (Fig. 3.1(d)) can be designed in accordance with the angle of the light beam coming from the waveguide.

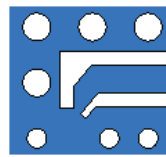
Fabrication

The device was fabricated through soft lithography [18] using SU8 masters. Additionally, in this work, the technological simplicity was kept to one photolithographic level. Scanning electron microscope (SEM) pictures of the SU8 master (thickness of $120 \mu\text{m}$) are shown in Fig. 3.3. In particular, the walls of the critical optical components, such as the

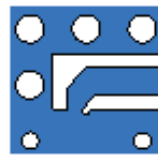
mirror (Fig. 3.3(b)) and the lenses (Fig. 3.3(c)), are required to be smooth and straight, in order to avoid undesired light scattering when replicating this master with PDMS polymer.



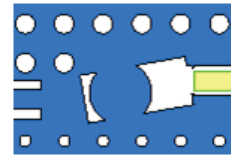
(a) SISO PDMS optical system



(b) $S=25 \mu\text{m}$

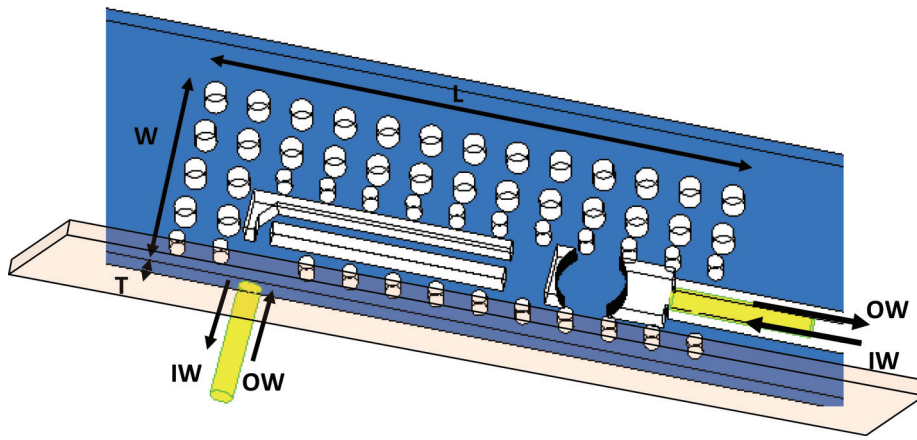


(c) $S=50 \mu\text{m}$

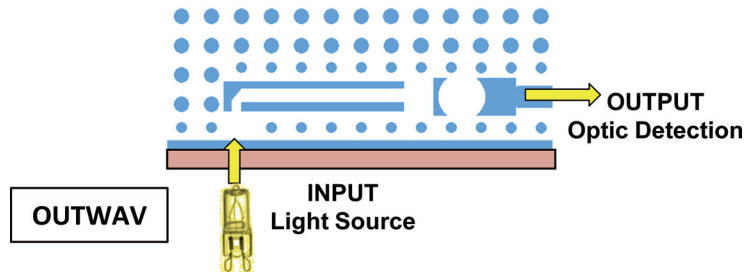


(d) Variation in the orientation of the FL

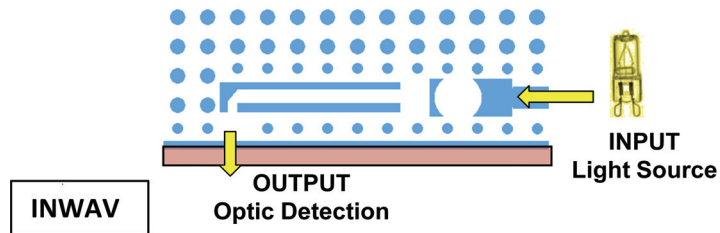
Fig. 3.1. (a) Section of the device (with $L=2.5 \text{ mm}$, $W=1 \text{ mm}$ and with thickness $T=120 \mu\text{m}$. S is the slit $70 \mu\text{m}$. M is the 40° mirror; WG is the TIR optical waveguides ($100 \mu\text{m}$ width). FL is the biconvex focusing lens ($160 \mu\text{m}$ radius of curvature). $F1$ is the fiber optic insertion and self-alignment system ($125 \mu\text{m}$ diameter). $F2$ is the fiber optic positioned in front of the slit. P is the pillar mirror. O is the output surface. I is the input surface. [(b) and (c)] Variations in the slit design with slit orientation angle at 40° . (b) $S=25 \mu\text{m}$ and (c) $S=50 \mu\text{m}$. (d) Variation in the orientation of the FL according to the angle of the rays coming from the waveguide.



(a) 3D Device



(b) outwav



(c) inwav

Fig. 3.2. Micro-optical interface functional configurations. (a) 3D view of the device and of the direction of the optical information. (b) OW configuration. (c) IW configuration.

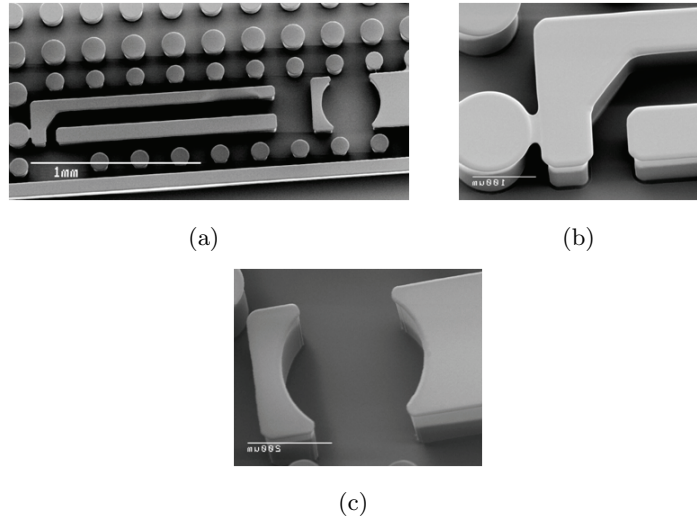


Fig. 3.3. SEM images of the SU8 master with $120\mu\text{m}$ thickness and slit $S=70\ \mu\text{m}$. (a) Picture of the entire functional geometry. (b) Details of the slit ($S=70\ \mu\text{m}$) and of the mirror (M). (c) Details on the focusing lens (FL).

3.2.2 Ray-tracing and experimental light path characterization

Experimental measurements were performed for static characterization and the results were compared with ray tracing simulations (Trace-Pro, Lambda Research Corp., Littleton, MA). The simulated ray-traced light path was determined for both configurations, considering the OW as a detector interface and the IW as a light source interface. In the simulation, the source optical fiber was approximated with a cone of light with $\text{NA}=0.22$ and a source area corresponding to the core size with diameter of $105\ \mu\text{m}$. Results shown in this section, in Figs. 3.4, 3.5, and 3.7, represent the light rays that have a power of at least 70% of the source power and that are incident on the output surface.

The experimental setup consists of a tungsten halogen lamp used as light source (Ocean Optics, H-2000, Dunedin, FL), the light being inserted into the device through a multimode fiber optic with a core diameter of $105\ \mu\text{m}$ and $\text{NA}=0.22$ (M15L01 SMA-SMA Fiber Patch Cable, Thorlabs, Dachau/Munich, Germany); a second identical fiber optics was used as light collector. The positions of the optical fibers acting as source and as light collector are described in Figs. 3.2(b) and 3.2(c) according to the configurations used (OW or IW). The experimental photographs of the light path can be interpreted considering the fact that the light spots visible to the camera are the ones related to light, which is not guided, while the areas where light propagation is not visible are the ones where light is properly guided toward the output.

OUTWAV

For OW configuration the simulation (Fig. 3.4(a)) shows that only the fraction of light from the source (F2) that passes through the slit is captured and then mirrored. It is then confined inside the waveguide and projected on the focusing lens, and directed to the output fiber optic (F1) with the appropriate NA. The OW experimental path in Fig. 3.4(b) shows, in accordance with the simulation, how the light coming from the source fiber optics (F2) is selected and captured by the slit (S), then reflected and bent by the mirror (M) and confined into the waveguide (WG) reaching the output surface (O) at a specific angle. The lens (FL) then focuses and redirects light to the output fiber optics (F1).

INWAV

Conversely, simulation of the IW source interface configuration (Fig. 3.5(a)) shows how light coming from the fiber optics (F1) is focused and coupled into the waveguide by the focusing lens and subsequently redirected by the mirror, at an angle close to 90° . The IW configuration experiment in Fig. 3.5(b) shows the inverse path of light coming from the source in F1, focused and confined in the WG by the lens FL. According to the simulation, part of the light is reflected by the mirror (M) toward the slit (S) and toward surface I of the fiber optics F2 at a specific angle. As an additional analysis of the device design in the IW configuration, a simulated near field of the light emerging from the slit is shown in Fig. 3.6(a). It can be seen that the predicted profile has an approximately rectangular shape corresponding to slit size S ($120 \times 70 \mu\text{m}^2$). This was experimentally visualized by means of an objective (10x) positioned on surface I to capture and magnify the light coming from the slit and projected onto a charge coupled device (CCD) array (Pixelfly, PCO Imaging, Kelheim, Germany). Figure 3.6(b) shows a normalized spatial profile in a color-coded 2D visualization consistent with simulation of the near field profile.

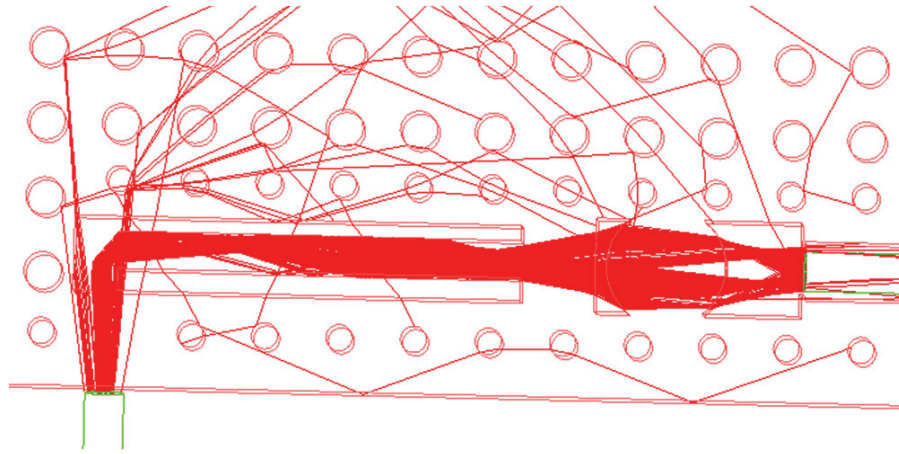
Design optimization

Simulations were performed to optimize parameters, such as the orientation angle of the slit in design variations (Figs. 3.1(b) and (c)) and the tilting angle for the lens FL. In particular, we show light paths simulation for a variation in the design considered to regulate the amount of light captured by the slit. The configurations shown in Fig. 3.7 include

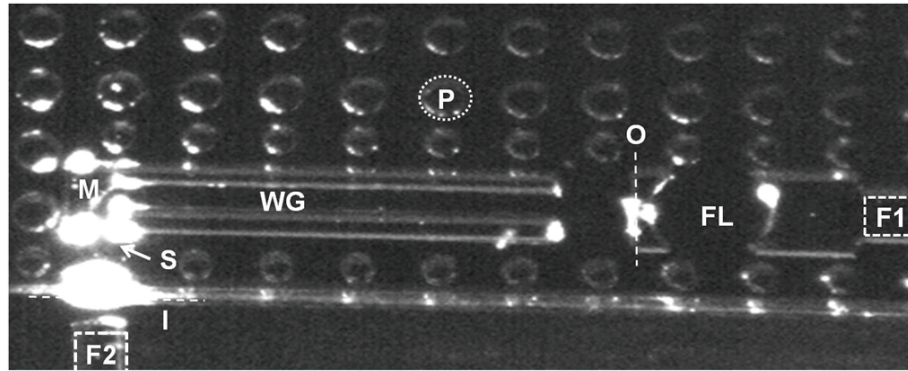
the slit sizes (a) $S=25 \mu\text{m}$ and (b) $S=50 \mu\text{m}$ with slit tilting angle at 40° (Fig. 3.1(b)) and the (c) $S=70 \mu\text{m}$ with straight slit. The slit angle allows for a more efficient rejection of rays. The input rays are, in fact, reflected out with a certain angle instead of being transmitted as in the case of a regular slit with no angle of tilting. In addition, static measurements on the efficiency of the light collection were performed and total losses for OW and IW were measured. The losses were calculated by comparing the power of the light rays, incident to the output fiber optic with the power of the light beam coming from the source fiber optics (input light). The losses thus take into account the selectivity of the slits and, therefore, the losses graph shows a clearly decreasing trend when the slit size increases (Fig. 3.8). This confirms the result that the slit is selective to light and filters out unwanted information. The simulation and the experimental results are consistent. Slight differences might be due to the fact that in simulation, the geometries are ideal with sharp corners, while in the PDMS devices, the geometric angles are smoothed due to soft-lithography fabrication limitations.

3.2.3 Dynamic characterization toward flow monitoring

The static optical characterization permits assessment of the efficacy of the proposed micro-optical devices, both as a detector and as a source interface, in the microfluidics environment. Results are presented here for the dynamic characterization of two-phase flow in both the in vitro and the in vivo experimental setups in relation to the OW configuration.



(a)

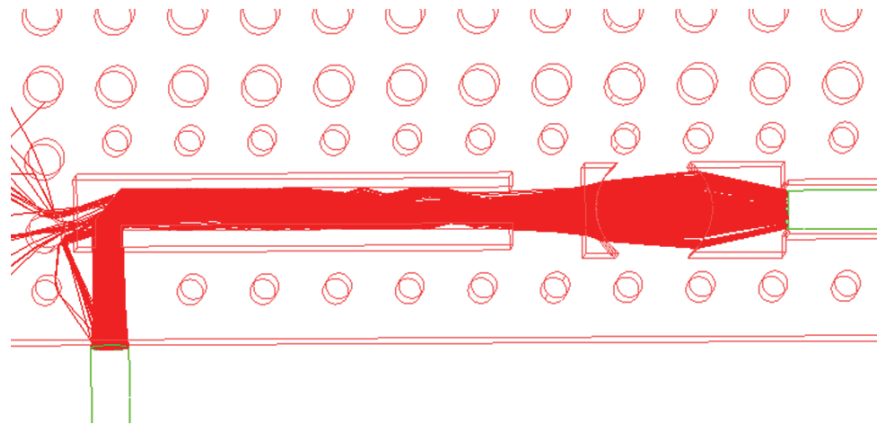


(b)

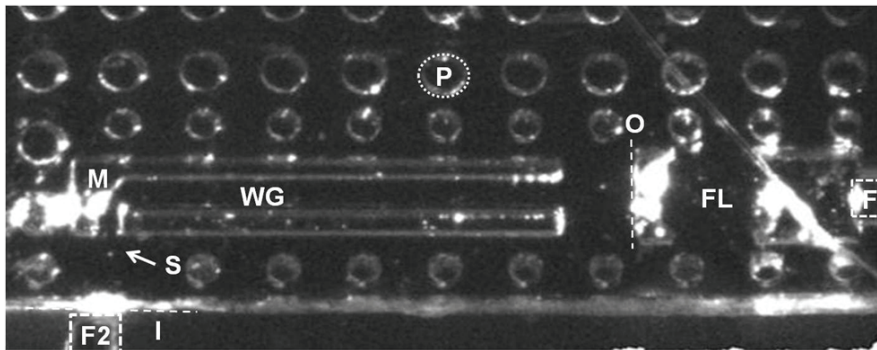
Fig. 3.4. Static optical characterization for PDMS device in OW configuration ($S=70 \mu\text{m}$ and thickness $T=120 \mu\text{m}$). (a) Ray tracing simulation of the light path. (b) Picture of the light path on the PDMS device.

Flow detection in in-vitro microfluidic system

The dynamic response of the device as detector interface (OW configuration) was tested, measuring light variation due to air bubble passage carried by ethanol, in a microfluidic mixer. A diagram of the setup for dynamic two-phase flow detection is shown in Fig. 3.9. It consists of



(a)



(b)

Fig. 3.5. Static optical characterization for PDMS device in IW configuration ($S=70 \mu\text{m}$ and thickness $T=120 \mu\text{m}$) Ray tracing simulation of the light path (only rays with a power of at least 70% of the source power).(b) Picture of the light path on the PDMS device.

a microfluidic y-junction serpentine mixer with $640 \times 640 \mu\text{m}^2$ section (Snake Mixer Slide, ThinXXS, Zweibrcken, Germany), whose inputs are connected to two pulsate piezoelectric pumps (TwinPump Slide, ThinXXS, Zweibrcken, Germany) injecting ethanol and air, respectively. A white tungsten halogen lamp was used as light source (LH-2000, Ocean Optics) and the light was projected onto the microfluidic

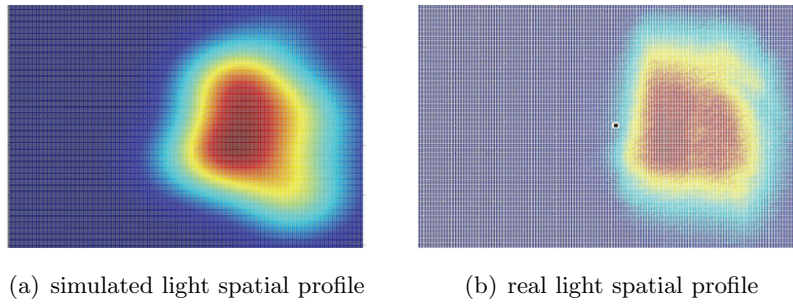


Fig. 3.6. Color-coded light spatial profile on surface I (Fig. 3.1(a)) for IW configuration. (a) Light profile found by ray tracing simulation. (b) Experimental light profile collected by a 10x objective and a CCD camera.

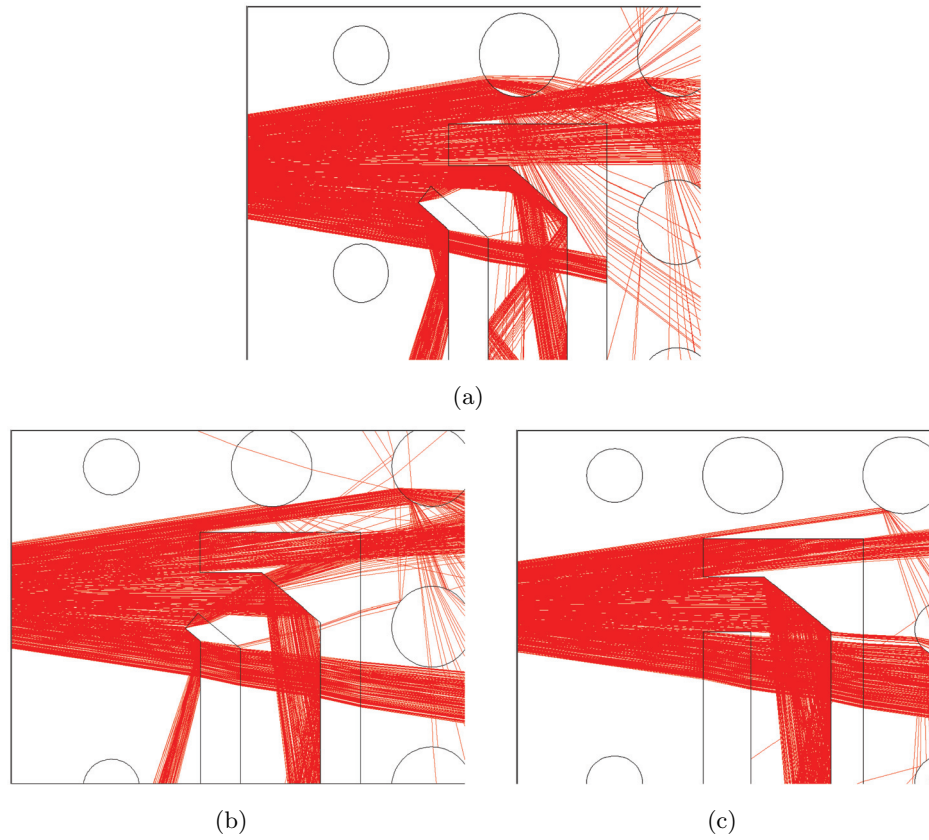


Fig. 3.7. Ray tracing simulation for OW configuration with slit sizes (a) $S=25 \mu\text{m}$ and (b) $S=50 \mu\text{m}$ with tilted slit, and (c) $S=70 \mu\text{m}$ with straight slit.

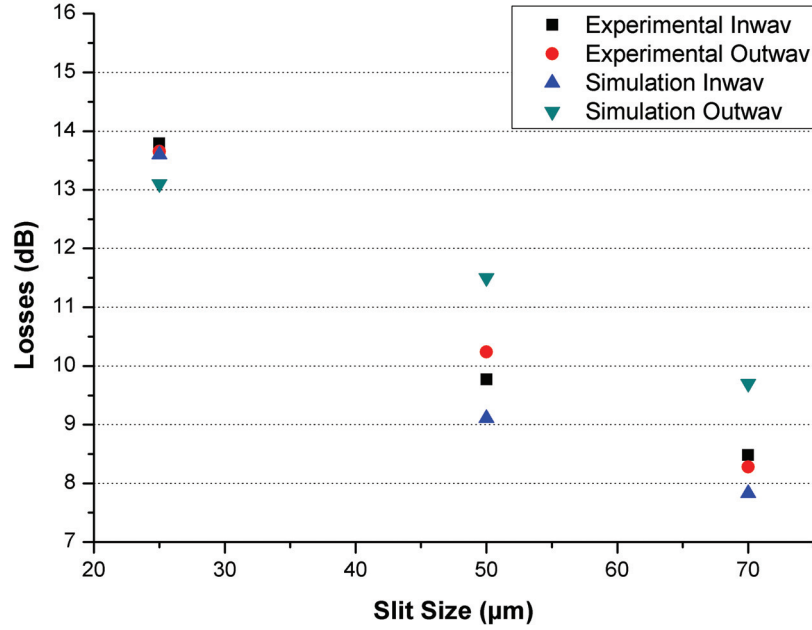


Fig. 3.8. Losses (dB) versus slit size: experimental and simulated.

device through a multimode fiber optic with a core diameter of 105 μm and $\text{NA}=0.22$ (M15L01 SMA-SMA Fiber Patch Cable, Thorlabs); a second identical fiber optic was used as light collector and then connected to a power-meter (model 1930 F-SL, Newport, Irvine, CA) for light power detection. Details of the experimental setup are shown in Figs. 3.9(a) and 3.9(b). The dynamically recorded light power variation due to the bubble passage is shown in Fig 3.10. The comparison between a reference experiment with a single-phase flow (ethanol) into the channel, and a two-phase flow (ethanol-air) experiment, shows the ability of the device to detect optical fluctuations with a signal to noise

ratio $S/N \approx 16$ dB and its suitability for multiphase flow detection and characterization.

Toward in vivo microcirculation flow monitoring

Flow dynamics of blood in experimental microcirculation was evaluated to test the efficacy of the micro-optical interface in non-noise-controlled environments, as an alternative to standard microscopy. The microcirculation was observed in surgical animal preparations. Optical access to microvessels was obtained through a transparent window chamber surgically implemented in the dorsum of hamsters (skinfold chamber) [41]. Fur was removed as well as some of the skin layers in order to make the skinfold transparent to light and suitable for in vivo microvascular experimentation. The hamster is placed in a tube to minimize movements and the tube is fixed to the stage under the microscope objective. Observation of the transilluminated animal tissue was simultaneously performed by means of intravital standard microscopy and by positioning the polymeric micro-interface on the tissue, as shown in Fig. 3.11 and Fig. 3.12. The microscopic vision allowed dynamic recording of image sequences of microvessels through a CCD camera and supported the positioning process of the micro-optical device on the microvessel. A micromanipulator was used to position the device on a specific microvessel, and then removed to allow the measuring process to be performed (Fig. 3.12). The alignment of the optical interface with the microcirculatory location under observation is obtained by means of microscopic upper views of the microdevice superimposed on the live tissue and taken using different focuses. The variation in focus exploits

the transparency characteristic of the polymeric technology, allowing visualization of the device during the positioning and aligning processes. Figure 3.13(a) shows the approximate position (red square is the region of interest) of the optical-interface slit. This setup allows the performance of simultaneous image recordings without interfering with optical measurements in the microcirculation field. The frame sequence (Fig. 3.13(b)) extracted from the video recording with intervals of 200 ms, and related to the region of interest, shows how the optical fluctuations are not visible to the naked eye. Optical signals from the polymeric micro-interface, used as detector in the OW configuration and superimposed on the live tissue in correspondence to a microvessel, are acquired by connecting the output fiber optics (F1) to a fiber coupled photodiode detector (PDA100A Si visible-NIR 4001100 nm, Thorlabs). They are subsequently digitalized through an acquisition board (NI PCIMIO16E, National Instrument, Austin, TX, USA) and filtered using a low pass filter with a bandpass frequency of 40 Hz to reduce power line noise. The microvessel under observation was simultaneously imaged by microscopy and dynamic video for flow dynamics characterization. Image processing was performed in order to obtain a dynamic optical intensity signal related to the region of interest, where the polymeric interface slit was positioned (red square on image in Fig. 3.13). Figure 3.14 shows the results of comparing the photodiode signal from the micro-optical interface in OW configuration, and the optical signal obtained from the video by averaging the digital intensity information on the slit area ($70 \times 70 \mu m^2$). The bold line represents the

photodiode signals and the thin line is the optical information obtained from the video, considering the sample rate as 30 Hz. For comparison purposes, both signals were normalized to obtain a zero mean and standard deviation equal to one. These signals provide information on the blood flow in the selected optical slit and other low frequency physiological phenomena, such as heart rate, vasomotion, and muscle activity. Both signals show oscillations at low frequencies, in the range between 0 and 10 Hz (Fig. 3.15)[62]. The effect of the natural movements usually present in *in vivo* tissue as well as other biological and instrumentation noises may be avoided by the improvement of the setup. Also, power line noise analog filters and a controlled transillumination light might be at the basis of a better discrimination of the blood flow signal over the background phenomena.

3.2.4 Conclusions

The design of the polymeric optical interfaces here proposed represents a miniaturization and optimization of standard optical setup designs that can be integrated in the implementation of flow monitoring systems in biomicrofluidics and that, in general, offer possibilities for new optical setups and technologies for monitoring and controlling multiphase microfluidic systems. The device designed presents two functional configurations allowing for bidirectional interaction, as a detector or as a source interface between the device and the microfluidic environment; it was fabricated using low-cost technology, requiring only one photolithographic step to define all its components. The realization of

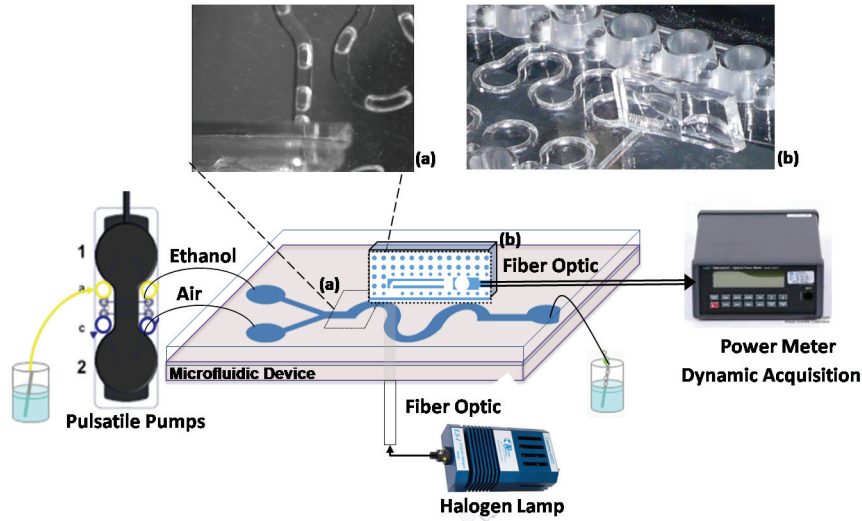


Fig. 3.9. Experimental setup for dynamic characterization of two-phase flow in a microfluidic device. Photographs of details in (a) upper view of the two-phase ethanol/air flow in the microfluidic device; (b) the micro-optic interface in the OW configuration positioned on the microfluidic mixer.

the proposed device prototype provides a proof of concept and demonstrates its efficiency in both simulated and experimental tests, in *in vitro* and *in vivo* experimentations, for static optical characterization and for dynamic flow monitoring. The polymeric micro-optic interface, exploiting an advanced configuration, includes light mirroring, guiding, focusing, and collimation, and aims to work at any angle of light direction, with a robust fiber optics self-alignment system, in order to leave the area under observation accessible to other types of optical processing and analysis. Furthermore, the air/PDMS structure of the device makes it transparent and, therefore, both the microfluidic area for the *in vitro* and the live tissue can be optically accessible,

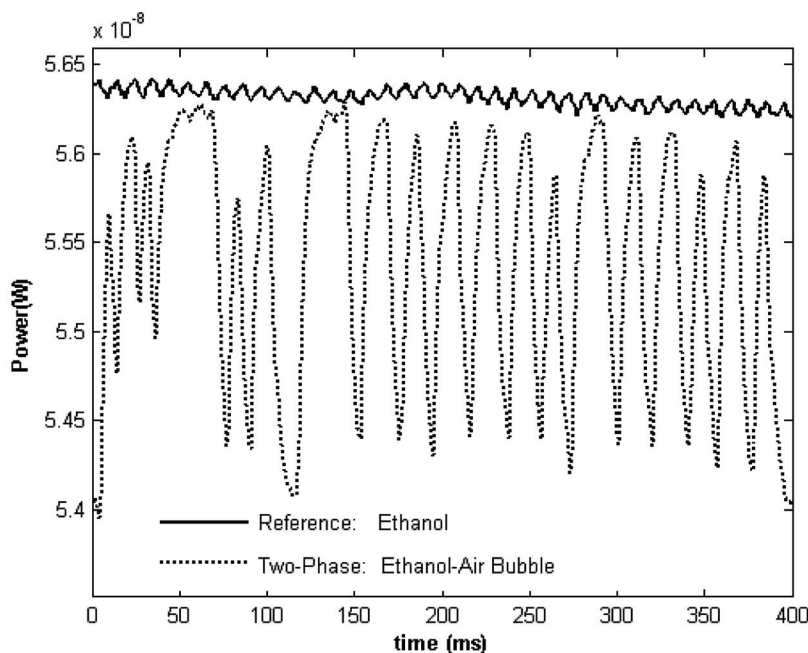


Fig. 3.10. Light power dynamic response due to the bubble flow measured by the power meter.

simply by changing the focal plane for observation. Thanks to such features, the device design, compared to others, responds to the practical need for a disposable optical interface which, superimposed on the microfluidic sample, either *in vitro* or *in vivo*, allows other optical measurements, such oxygen concentration, functional capillary density, or other morphological measurements, to be performed simultaneously without interfering with their experimental setup. Such a complete approach represents an advancement in solving issues related to sensing system in microfluidics. The design of these polymeric optical interfaces, in fact, makes them portable and easily attachable to microfluidic

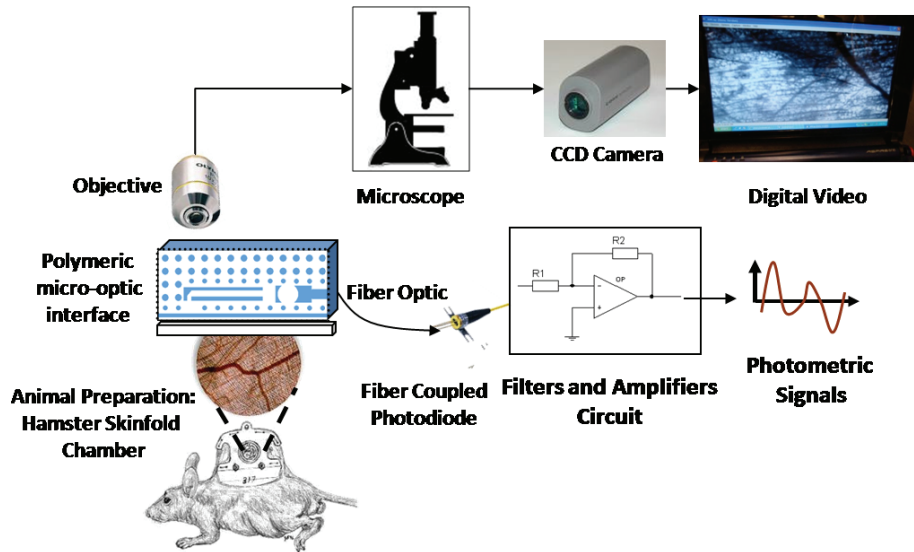


Fig. 3.11. In vivo flow monitoring system.

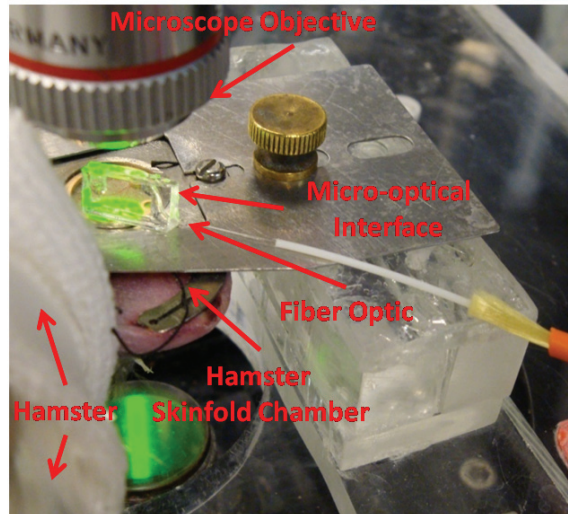


Fig. 3.12. In vivo flow monitoring system photograph. Micro-optical interface on live hamster tissue for the acquisition of photometric signals.

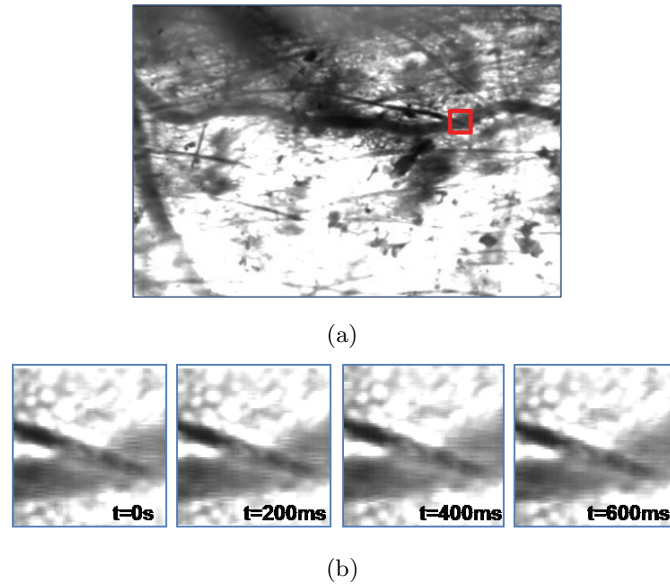


Fig. 3.13. Microcirculation fields under the polymeric device with digital $70 \times 70 \mu\text{m}^2$ slit. (a) Entire frame and region of interest (red square). (b) Frame sequence related to the region of interest at intervals of 200 ms.

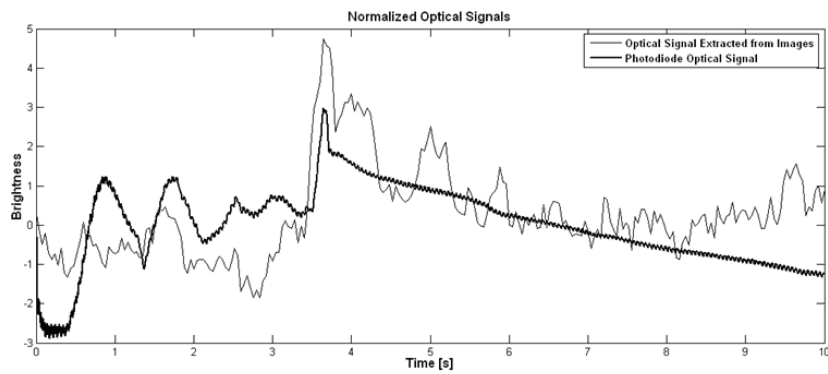


Fig. 3.14. Comparison between the normalized optical signals resulting from photodiodes acquisition and the digital slit obtained from image sequence analysis.

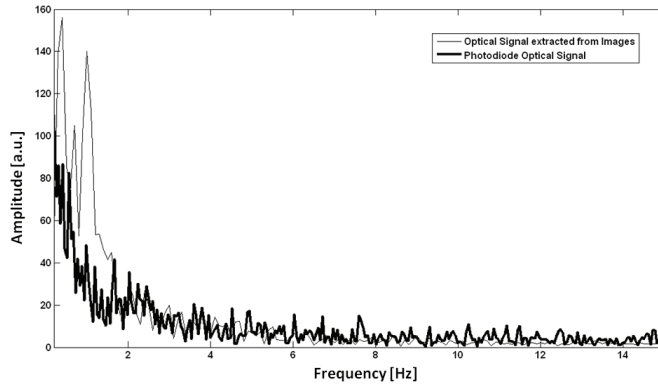


Fig. 3.15. Spectral components of the photodiode signal and of the time series extracted from the image sequence.

devices or to animal skin, thus providing the opportunity for a continuous monitoring of the flow processes, regardless of the experimental setup and disturbances. They would allow laboratories without specific or advanced optical equipment to start research activity on fluid and particle flow in microfluidic processes. Concluding, this optical systems are a proof of concept, demonstrating that the devices are efficient and show high signal to noise ratio in controlled conditions (in vitro dynamic experimentation); it also presents encouraging results, however, in the extremely noisy in vivo environment. We consider these results, along with the idea of integrating two or more interfaces for dual slit method implementation, a significant basis for continuing work in this direction toward a surely ambitious target of flow monitoring in an in vivo environment.

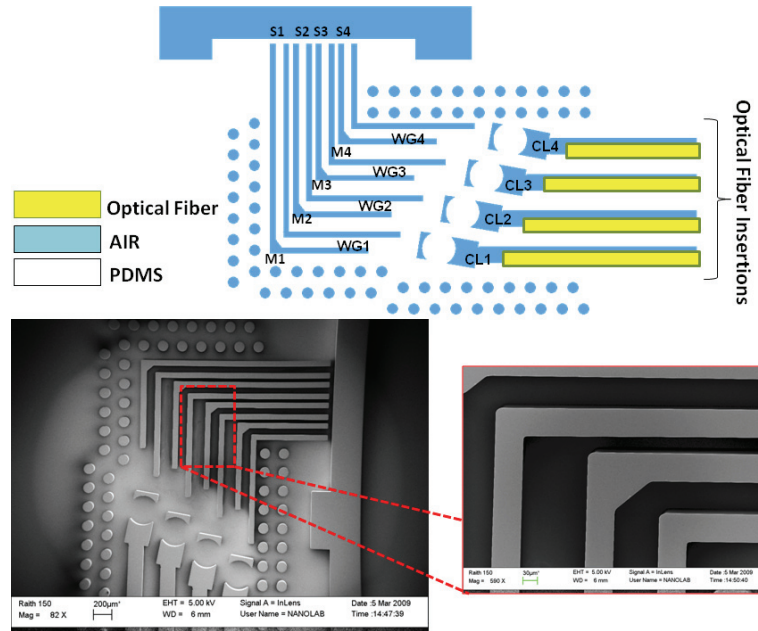


Fig. 3.16. Input micro-optical device. The top figure shows four insertions for the input optical fibers, the collimating lenses ($CL_{1,2,3,4}$), the PDMS waveguides ($WG_{1,2,3,4}$), the air mirrors of length $97 \mu\text{m}$ ($M_{1,2,3,4}$) and the output slits ($S_{1,2,3,4}$). The slit size is $70 \mu\text{m}$. The bottom inset on the left depict the SEM check of the input device in the master while on the right the SEM indicates the particular structure of both mirrors and waveguides.

3.3 MISO sensing systems

3.3.1 Design and fabrication

The optical devices, here presented, exploits PDMS/air interface to generate total internal reflection (TIR) and a particular deflection of light beams by means of the difference in refractive indices between air and PDMS ($n_{air}=1$, $n_{PDMS}=1.41$) so that mirrors, 2D focusing or collimating lenses could be designed. The complete optical system involves two parts: an input device used to illuminate the microfluidic channel

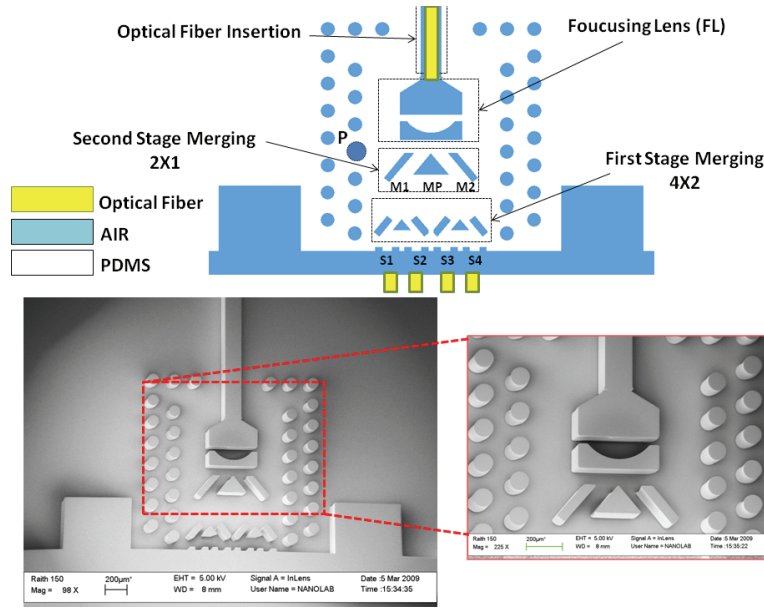


Fig. 3.17. Output micro-optical device. This device merges four light paths coming from ($S_{1,2,3,4}$) in a unique beam by means of two stage merging (4x2 and 2x1). A block including two straight mirrors of length $275 \times 50 \mu\text{m}$ $M_{1,2}$ and a mirror prism MP ($250 \times 200 \mu\text{m}$) is needed to combine two light path in one. The light is then focused by a focusing lens (FL) toward the output optical fiber. The pillar mirrors with diameter of $100 \mu\text{m}$ (P) are used to protect the device from the out coming light. The SEM picture at the bottom depicts the structure of the device in the master.

areas with light beams at different wavelengths ($\lambda_1, \lambda_2, \lambda_3, \lambda_4$) and an output device that aligned with the input device allows to collect and merge the light beams for the detection of the flow dependant optical signal. The input device is detailed in figure 3.16. Four insertions for input optical fibers ending with a 2D collimating lens are needed to correct the numerical aperture (NA) of the optical fiber minimizing beam divergence and providing parallel beams at the output lens. Then the four light beams are guided through waveguides ($WG_{1,2,3,4}$) that

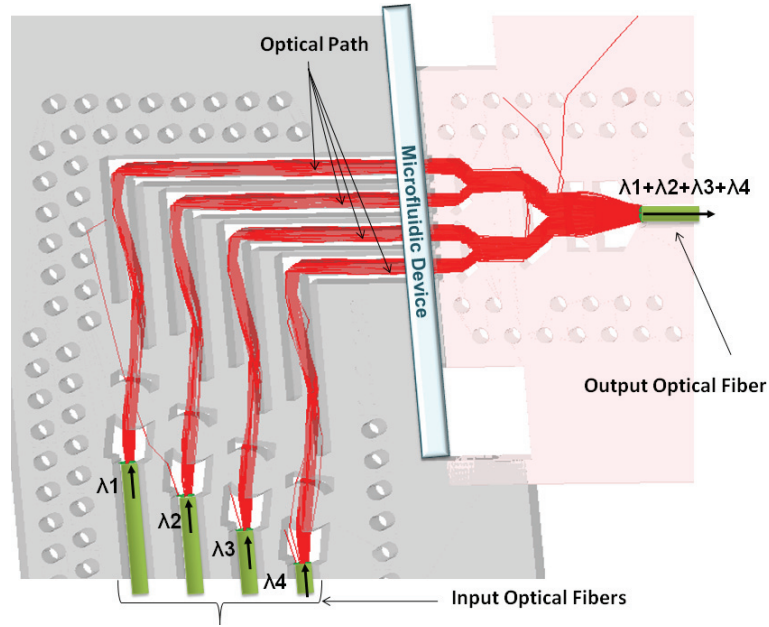


Fig. 3.18. Ray-tracing of the complete optical setup: four light beams of different wavelength are focused and redirected toward the microfluidic channel. The transparency of the microfluidic channel allows the rays to pass through the device. The out coming light is then collected and merged toward the output optical fiber.

include mirrors (M) inclined at an angle of 40° to the horizontal axis for light reorientation toward the output slits. Thus the four beams are directed to four areas on the centerline of the microfluidic channel and after transmission they are captured by four windows (slits - $S_{1,2,3,4}$) of the output device detailed in Fig. 3.17. In the output device the light beams are merged by two stage merging. In the first stage the optical signals related to the window S_1 and S_3 are merged respectively with the optical signals coming from S_2 and S_4 . The obtained signals are merged together in the second stage. The mirror prisms, indicated in Fig. 3.17 as MP, perform the merging while mirrors ($M_{1,2}$) are needed

for light reorientation towards the mirror prism facets. The first stage merging is a replication of a second stage merging so it has the same design (see Fig. 3.17). A focusing lens (FL) is used to match the NA of the output optical fiber. Circular air pillars (P) are included in the designs of both devices to protect the optical path from external light by scattering the light away from the information signal. In addition, self-alignment systems are disposed to facilitate the output fiber optic insertion.

Optical simulations were performed (TracePro, Lambda Research Corp.) to optimize and validate the design providing also power measures necessary to a whole characterization of the devices. The simulation in Fig. 3.18 shows clearly the light path (colored in red) from input to output for the complete configuration. The simulation shows also that the waveguides exhibit good confinement of light, bringing the parallel beams to four different locations along the micro-fluidic channel. Moreover the divergence-free beams allow reliable absorbance measures of the specimen. The transmitted portion of the light is then collected by the output device (on the right part in figure 3.18) that merges together the four light paths to a single beam that finally is collected by means of the output optical fiber. The memory of the spatial locations is maintained through the four wavelengths of the input signals that are maintained in the output signal.

Fabrication process

Poly(dimethyl siloxane) material (Sylgard 184 elastomer kit, Dow Corning, Midland, MI, USA) was chosen to fabricate the optical devices

for its several advantages: biocompatibility, transparency in the visible range, low cost, low toxicity, and high reliability. A single photolithography step is needed to build the SU-8 (SU8-25, MicroChem Corporation, Newton, MA, USA) master so that a constant height of $120\ \mu\text{m}$ was achieved. The height was chosen so that the devices have a minimum dimension required to insert easily the optical fibers in the alignment system. The rapid-prototyping allows to fabricate the devices within one day [18]. The device is realized through a simple micromolding technique called soft-lithography that has been deeply studied. Soft lithography provide an alternative set of techniques for microfabrication and it uses physical contact between a topological patterned stamp and a substrate (master).

3.3.2 Static characterization

Halogen light source connected to a multimode optical fiber was used to illuminate one by one the input slits of the output device (Fig. 3.17). The output optical device is the critical part of the complete system because of the multiple total internal reflection needed for light beams merging. The light power was evaluated experimentally at the output fiber (see Fig. 3.17) connected to a power-meter (Newport,1930F-S). The input power was $16000\ \text{nW}$. The obtained results were compared with the power obtained by ray-tracing simulations. The power has been calculated from ray-tracing simulations into different conditions: when the output fiber is perfectly inserted in the alignment system and when there is a rotation of 4° respect to the collimating lens. Asserting

that the experimental measures of the power agree with the simulated power with a mismatching of the fiber we calculate then the power losses of the device. Fig. 3.19 depicts the light attenuation (in dB) for each slit. The difference of light losses between the symmetric slits can be explained by a weak misalignment between the output fiber and the focusing lens as explained before. A mean loss of ≈ 18 dB was found experimentally, and it could be explained with the multiple light's reflections in the mirrors of the micro-optical device. The efficiency of the input device has been tested in the previous section.

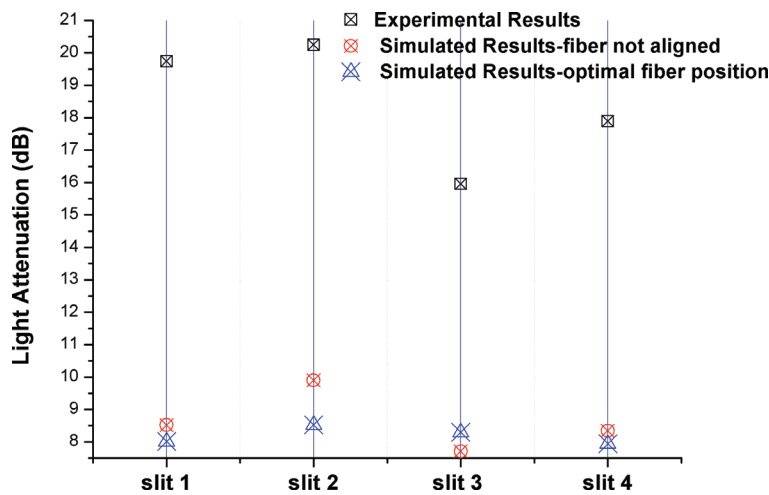


Fig. 3.19. Out coming light attenuation for each slit. The losses are calculated from experimentation and simulation by measuring the power of the light at the output fiber. The mismatching between the slits indicates a slight misalignment of the output fiber. It is also indicated by means of simulations the losses in case of perfect insertion of the output fiber.

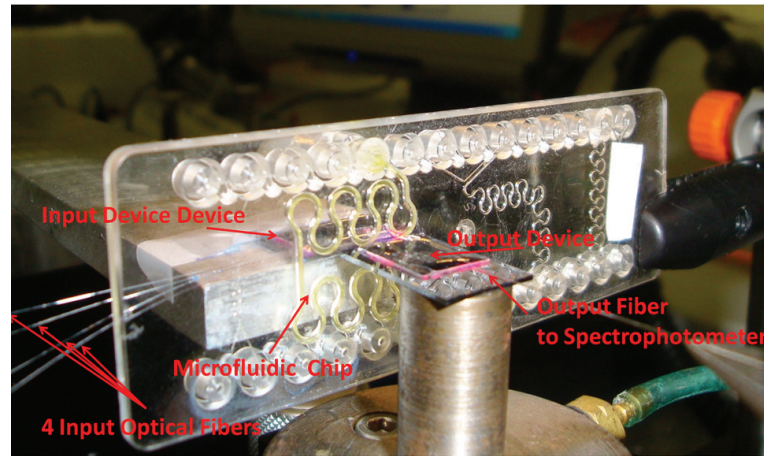


Fig. 3.20. Experimental setup for optical detection system in the microfluidic two-phase flow system.

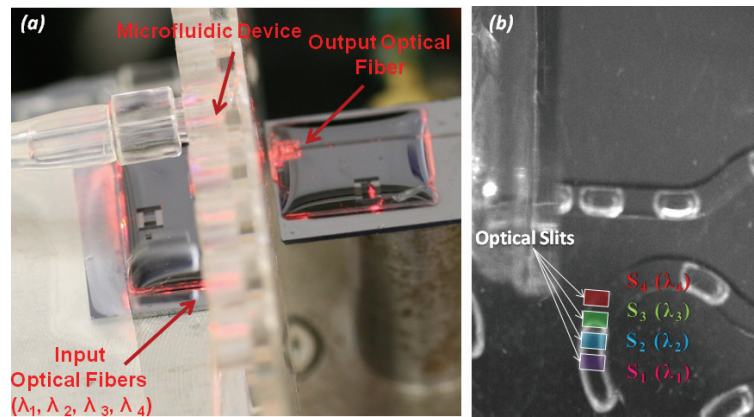


Fig. 3.21. (a) Particular of the experimental setup. The selected areas of the microfluidic device are sandwiched between the input and output optical device. (b) Slits' locations in the microchannel.

3.3.3 Dynamic characterization

Experiments were carried out superimposing the micro-optical device on a serpentine microfluidic y-junction mixer. The two-inlets serpentine mixer (Thinxxs Microtechnology) is $640 \mu\text{m}$ in width and in height. A

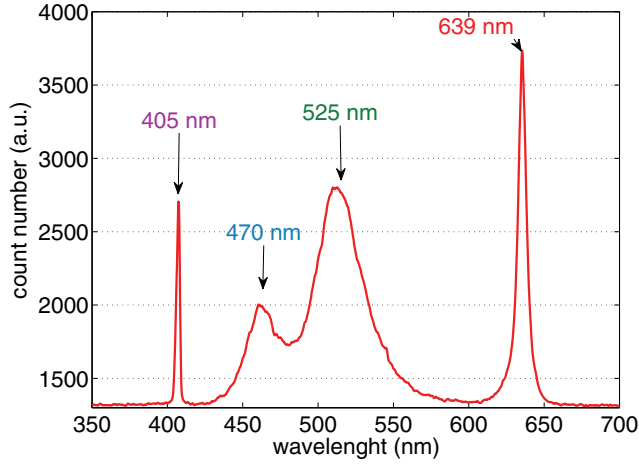


Fig. 3.22. Typical output spectrum representing four peaks at different wavelengths. Each wavelength is representative of a slit's position in the microchannel: *slit*₁ - 405 nm, *slit*₂ - 470 nm, *slit*₃ - 525 nm, *slit*₄ - 639 nm.

picture of the experimental setup is reported in Fig. 3.20. It shows a sandwiched structure: the microfluidic device is positioned between the input and output optical device. In figure 3.21(a-b) it is indicated more clearly the sandwich setup and slits positioning in one curve of the micro-mixer.

Ethanol-air two-phase flow was generated by means of two syringe pumps (Nemesys) connected to the channel's inlets and providing constant flow rate. Multimode fibers with a numerical aperture (NA) of 0.22, a core diameter of 105 μm , and a clad diameter of 125 μm were used. Two fiber-coupled lasers ($\lambda_1=405$ nm, $\lambda_4=639$ nm) and two SLEDs ($\lambda_2=470$ nm, $\lambda_3=525$ nm) were used as sources and a spectrophotometer (Ocen Optics) was connected to the output optical fiber to collect the out coming photons for the successive flow analysis. The

output spectra was then dynamically captured every 50 ms, in a time windows from 20 to 30 s and post-processed to detect amplitude fluctuations of the spectrum's peaks associated to the four wavelengths. An example of spectrum is shown in Fig. 3.22. The wavelengths of the four peaks are indicated in that figure while on the y-axis are indicated the number of photons (count).

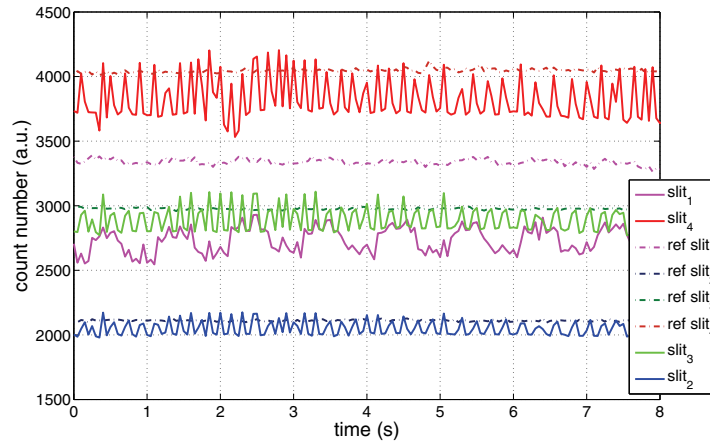


Fig. 3.23. Results of a two-phase flow experiment for constant input flow: air $5 \mu\text{l/s}$ and ethanol $24 \mu\text{l/s}$. The reference signals represent ethanol flowing at $24 \mu\text{l/s}$.

A variety of experiments were conducted varying the flow rate of air or ethanol. The first experiment was conducted keeping the air flow at $5 \mu\text{l/s}$ and ethanol at $24 \mu\text{l/s}$. Fig. 3.23 reports the time variation for the spectra peaks' amplitude related to all slits (S_1 , S_2 , S_3 , S_4) compared with a reference signal obtained for the experiment with constant ethanol flowing in the microchannel ($24 \mu\text{l/s}$) as shown in Fig. 3.23 (reference signals). It is worth to notice that the time signals related to

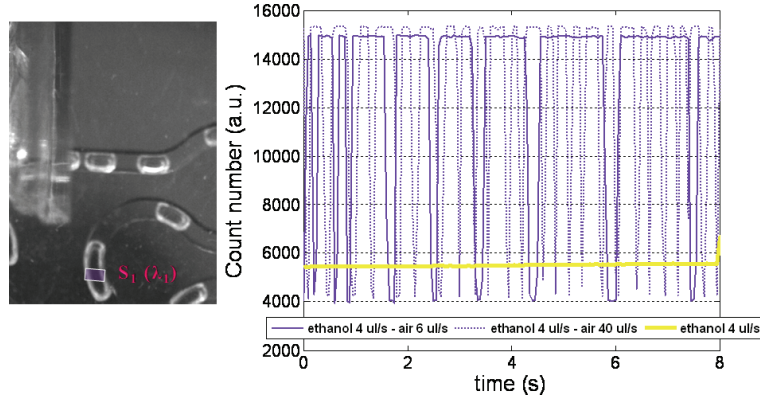


Fig. 3.24. Signals related to bubbles' passage at two different velocities. The signals are recorded for the $slit_1$ associated to λ_1 .

slit S_1 and S_4 show a better amplitude variation than the signals coming from S_2 and S_3 . This fact is related to the different light sources: SLEDs for S_2 and S_3 and lasers for S_1 and S_4 so laser sources provide a powerful input signal than that of SLEDs so are suited for experimental studies in microfluidics. Asserting the different functionality of the four slits, in Fig. 3.24 it is shown the variation of the output time signal related to S_1 when the air flow is decreased from 40 to 6 $\mu\text{l/s}$ in a time window of 8 s. From visual inspection it is clear that increasing the air flow rate the bubbles' passage through S_1 increases. The carrier flow (ethanol colored with Potassium Hexacyanoferrate($K_3\text{Fe}(\text{CN})_6$)) was considered to obtain a reference signal. Yellow ethanol is used in this experiment to minimize the out coming light of wavelengths $\lambda_2=470$ nm and $\lambda_3=525$ nm and thus to increase the sensitivity of the other wavelengths.

The last experiments involve the dynamical response of the device in

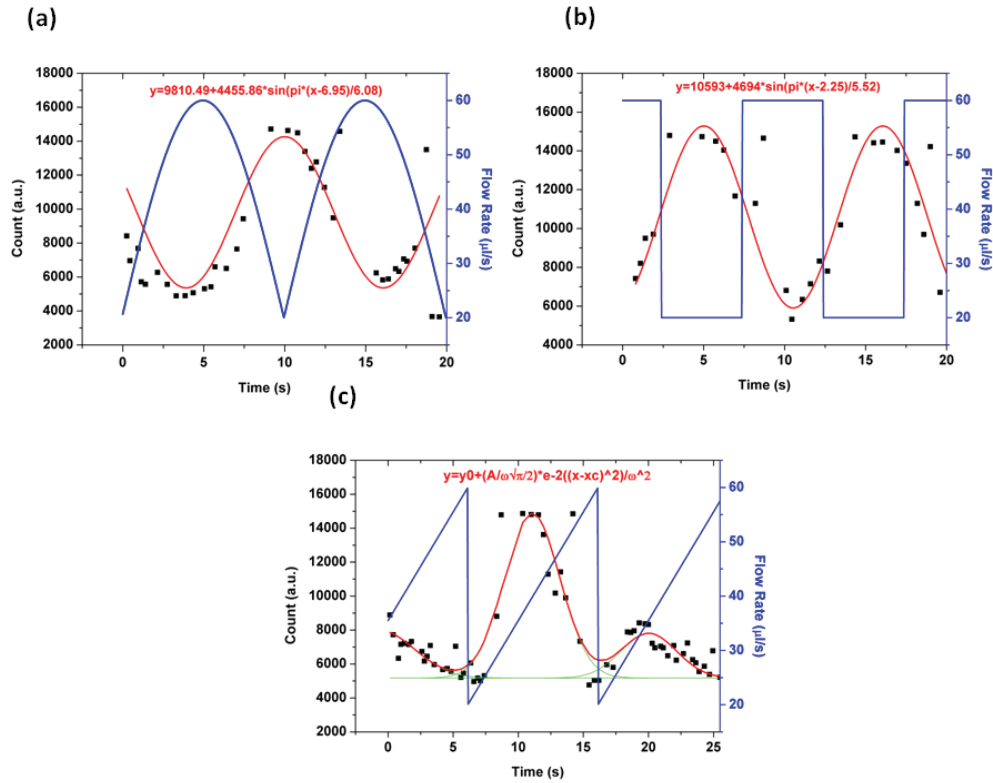


Fig. 3.25. Fitting of the maximum peaks in the data flow acquisition in S_1 for (a) sinusoidal, (b) square, and (c) saw-tooth air flow rate (ethanol flow rate is maintained fixed at $4 \mu\text{l/s}$). The bubble flows for sinusoidal and square input are both fitted with a sinusoidal function, while the bubble flow for saw tooth generate a flow that can be fitted with two Gaussian functions.

real-time when it is applied a time varying input flow rate. A variety of air flow rates have been applied at the channel's inlet to prove the efficiency of the optical system to acquire dynamically flow variations. Sinusoidal, square, and saw tooth flow rate function with minimum flow rate of $20 \mu\text{l/s}$, maximum flow rate of $60 \mu\text{l/s}$, time period $T_p=10$ s and time step of $T_s=0.3$ s are applied as air flow while yellow ethanol

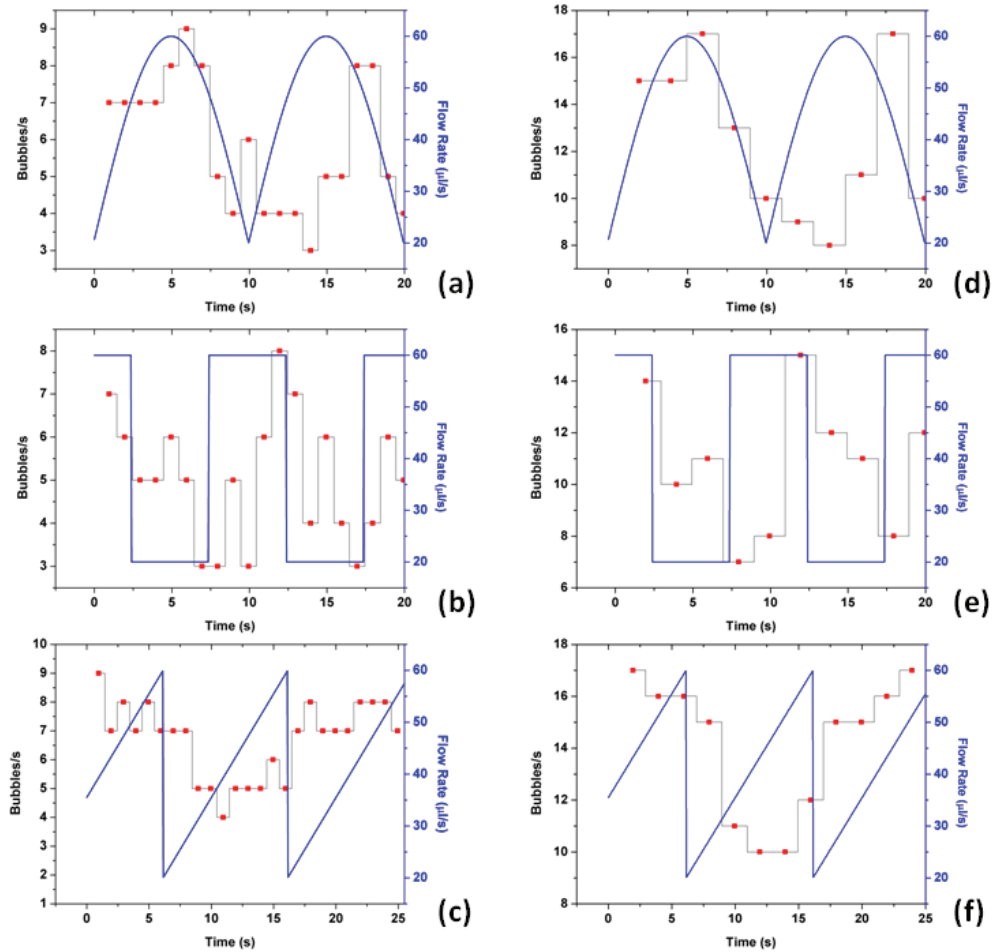


Fig. 3.26. Number of bubbles that flow in slit S_1 each 1 s for: (a) sinusoidal, (b) square, and (c) saw-tooth air flow rate. Number of bubbles that flow in S_1 each 2 s for: (a) sinusoidal, (b) square, and (c) saw-tooth air flow rate. The ethanol flow rate is maintained fixed at $4 \mu\text{l/s}$.

flushes at constant flow rate ($4 \mu\text{l/s}$). Maximum peaks versus time relative to the spectrometer acquisition of the bubble flow obtained for air flow rate sinusoidal (Fig. 3.25(a)), square (Fig. 3.25(b)), and saw tooth (Fig. 3.25(c)), are shown in figure 3.25 only for slit S_1 . It is vis-

ible how the maximum peak amplitude is modulated by the periodic air flow variations (see blue line in Fig. 3.25): flow rate and maximum count relative to bubbles flow is inversely proportional, because if the air flow rate increases the bubbles speed up and as consequence the spectrometer count a minor number of photons. The response of the bubble flow to the applied flow rate function can be explored by fitting the point values of the maximum count. In Fig. 3.25(a,b,c) red lines represent the fitting functions. For sinusoidal and square air flow rate the bubbles flow can be fitted with a sinusoidal function $y=y_0+A\sin(\pi(x-x_c)/w)$. It is worth to notice that the fitting functions for sinusoidal and square input flow rate have approximately the same parameters ($y_0=9810.49, A=4455.86, x_c=6.95, w=6.08$ for sinusoidal input and $y_0=10593, A=4694, x_c=2.25, w=5.52$ for the square input). A great difference is evident looking on Fig. 3.25(c) for saw-tooth flow rate. Two levels of peaks can be noticed so a multi-peak fitting approach has been chosen; two Gaussian functions interpolate the output flow data. Asserting the variability of the bubble flow in relation to the air flow rate it is interesting to quantify the number of bubbles flowing for each second through slit S_1 . So we considered the total number of bubbles that passes the first slit (S_1) in 1 s and also in 2 s in relation to the varying flow rate. The analysis related to the number of bubbles in 1 s gives the possibility to investigate on the optical acquisition system sensitivity to bubble passage while the analysis for 2 s gives information on the response time and the typology of that response in terms of bubbles' quantity. As for the first analysis in Fig. 3.26(a,b,c)

on the y-axis the quantity of bubbles sensed through slit S_1 are shown in relation to time (x-axis) for sinusoidal (Fig. 3.26(a)), square (Fig. 3.26(b)) and saw-tooth (Fig. 3.26(c)) air flow rate. Each 1 second is possible to notice how the flow rate variation affects bubbles production. The maximum number of bubbles associated to the maximum flow rate ($60 \mu\text{l/s}$) is for all the varying flow rate of 8-9 bubbles/s while the minimum is 3-4 bubbles/s for $20 \mu\text{l/s}$. In order to reduce the variability of the bubbles we performed a successive analysis in which the bubbles are quantified each 2 seconds. This analysis allows to emphasize the response of the microfluidic two-phase flow system in time and to quantify also the delay time between flow rate application and response. In this context is important to consider the position of the optical system in the microchannel. The first slit S_1 is positioned at a distance of ≈ 105.58 mm from the confluences. Taking into account the sinusoidal flow rate in Fig. 3.26(d) it can be noticed that the response is subjected to a delay that increases in the second period of the sinusoid. A delay of 1 s is reached in the first period while in the second period increase to 3 s. As for the square function a delay of ≈ 4 s can be seen in Fig. 3.26(e) in relation to the second period of the input flow. Also for the saw-tooth flow rate a delay of ≈ 4 s can be noticed looking on the second period of the flow rate wave. We can conclude that the response time of the two-phase flow system is ≈ 4 seconds. Consequently the quantity of bubbles that are sensed by the micro-optical system can be detected by analyzing only the amplitude variation of the out coming signal so it is possible to create an associ-

ation between amplitude of the time signal and the temporal passage between two successive bubbles. This method can be also exploited for velocity measurements of bubbles/droplets in microfluidic device.

3.3.4 Conclusions

The design of the MISO polymeric devices presently proposed, for spatial distributed flow monitoring, represents a miniaturization and optimization of advanced macroscopic optics design. Its main feature is represented by the extraction of optical signals which provide information on flow profile, respecting the spatial distribution of the information and exploiting the wavelength as a fingerprint of the spatial position. Moreover these devices allow a multi-wavelength response of the sample in the microfluidic device in an unique measure. Possible applications are wide and range from sensing in biological fluid flow, for example in the in vivo microcirculation, to bubbles/droplets' flow in microfluidic systems. The optical systems could be used for laser-induced fluorescence detection confirming the versatility of the proposed micro-system. The designed poly(dimethyl siloxane) devices could be also used in the reversed configuration as a light splitter for monocromatic measures and the integration into poly(dimethyl siloxane)-based microanalysis systems.

3.4 Poly(dimethyl siloxane) light splitters

3.4.1 Introduction

The capability of evaluating spatially distributed flow properties at the micrometric scales level has various application in the field related to the Laboratory on a Chip (LOC) [4]: from dynamic velocity measurements to the characterization of spatial profiles. Various multiple-point detection schemes have been presented for different applications as particle velocity measurements in capillary electrophoresis [29]. Also applications in research and in industry in other important fields as communications and fiber optics technology [29] exist. Several commercial solutions exist as light splitters and coupler for digital information transfer and managing through fiber optics. The standard splitting is based on interference principles or on multi-splitting micro-channels. The first solution involves microchannels guiding light in specific path. This solution can be implemented through different technological processes. Multimode interference (MMI) splitters [33], suitable for use in integrated optical fluorescence array sensing, with particular applications in lab-on-a-chip (micro-TAS) technologies. Such solution represent an important basic block for photonic and optoelectronic integrated circuits due to their simple structure, low excess loss, large optical bandwidth, and low polarization dependence. Their limit is related to the fact that the typical length of standard design MMI splitter/combiners is longer than desired for functions that require the output waveguides be spaced far enough apart to minimize optical and

electrical interaction. In order to overcome limits due to rigid designs due to channels network or long MMI splitters, in this work we propose channel-free solutions for light splitting. In particular we present two designs variations of light splitters which are respectively based on Total Internal Reflection (TIR) and on partial refraction of light on air/PDMS interfaces.

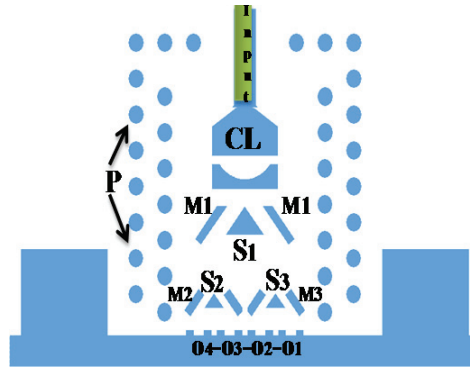
3.4.2 Splitter based on TIR condition

The advanced design, shown in Fig. 3.27(a), is a light splitter allowing the division of one input beam into four output beams. A self-alignment system is disposed to facilitate the input fiber optics insertion. A collimating lens (CL) is then used to correct the numerical aperture of the input optical fiber. The first prism (S1) works as splitter under condition of TIR. It is positioned at the center of the input light beam in order to split in two and redirect the resulting light beams towards the two mirrors (M1). They redirect light towards the second set of splitting provided by prisms (S2, S3), which perform division of beams as well, exploiting the mirrors M2 and M3 for redirecting light towards the outputs (O1,2,3,4). Circular air pillars (P) are included in the design to protect the optical path from external light. The scanning electron microscope (SEM) picture of the SU8 master (thickness of $120\mu\text{m}$) is shown in Fig. 3.27(b). The measures of this device have been shown in the previous section.

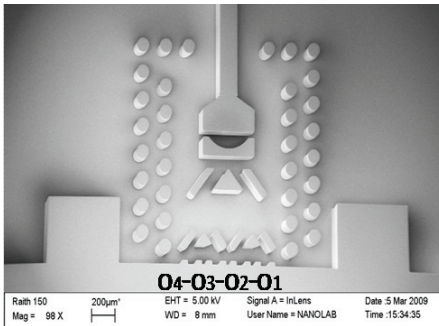
3.4.3 Splitter based on partial refraction

The design of the splitter based on partial refraction (Fig. 3.28(a)) allows the division of one input light beam into three output beams. The input optical fiber enters in the self-alignment system, followed by a collimating lens (CLin) for adjusting its numerical aperture. The heart of the entire design is represented by the single irregular prism (P1). Its geometry works by means of two surfaces, and performs, in principle, the division of the input beam into three output beams, each with one third of the input original power. The strength of this design is represented by the very small size of the prism (367 μm maximum width and 695 μm total height). The functional principles are shown in details in Fig. 3.28(b): the first surface (surf1) causes the reflection (R1) of one third of the incident input beam (In) and the transmission (T1) of two third of it. The second surface (surf2) causes the reflection (R2) of one half of the incident beam (T1) and the transmission of the resulting beam (T2). The geometry of the prism includes an enlarged bottom in order to allow the beam R2 to travel toward the output surface (surf3) with no interference with the walls. The three beams (R1, R2, T2) coming from the prism P1 need to be readjusted in order to be suitable as output of the splitters: collimated and with a specific width of 70 μm . The lens CL3 collimates the beam R1 towards the output aperture O3. Its distance from the prism depends on the desired size of the output beam. The mirror M2 (1.3 mm x 50 μm) and the lenses FL2 and CL2 are meant to redirect, resize and collimate the beam R2 towards the output O2. The mirror M3 (1 mm x 50 μm) and the lenses

FL3 and CL3 redirect, resize and collimate the beam T2 towards the output O3. This configuration also includes a set of circular air pillars (P) as a shield from the background light. The SEM pictures of the SU8 master are shown in Fig. 3.28(c). Two photos are necessary for imaging the entire device due to the SEM microscope specifics.



(a) Design



(b) SEM

Fig. 3.27. Splitter based on TIR condition. (a) Design. The blue part indicates air while white PDMS. (b) SEM picture of the SU8 master.

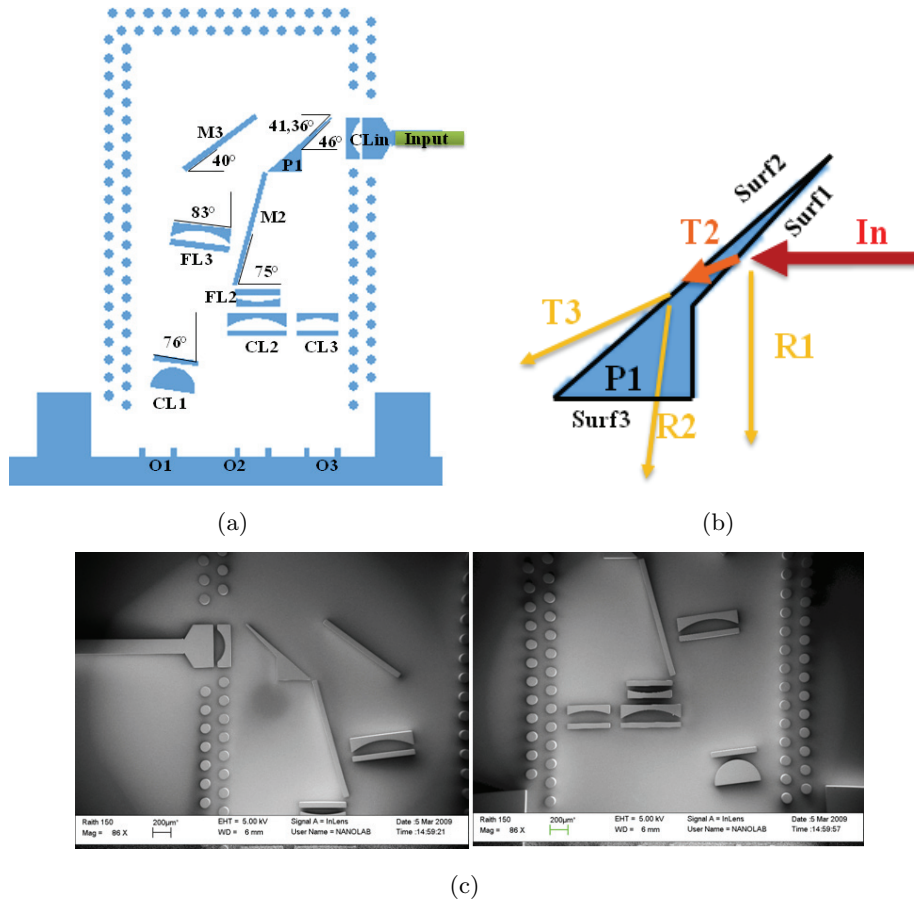


Fig. 3.28. Splitter based on partial refraction condition. (a) Design. The blue part indicates air while white PDMS. (b) Details on the prism P1 and functional principles. (c) SEM pictures of the master: upper part (on the right) including input system, lens CLin, prism P1, mirror M2, lens CL2 and CL3 and bottom part (on the left) including: mirror M1, and the lenses (CL1, CL2, FL2, CL3, FL3) to adjust the beams to the desiderate dimension and localization.

3.4.4 Ray-tracing and experimental characterization

Optical simulations were performed (TracePro, Lambda Research Corp.) to optimize and validate the splitters' design. The simulated ray-traced light path was determined for both configurations, the TIR-based and the refraction-based splitter. In the simulation, the optical fibers light sources were approximated with a cone of light with N.A. = 0.22 and a source area corresponding to the core size with diameter of $105\mu\text{m}$. Results shown in this section represent the light rays that have a power of at least 70% of the source power and that are incident on the output surface. In addition, experimental measurements were performed for static characterization and performance analysis and results were compared to the ray tracing simulations. The experimental setup consists of a tungsten halogen lamp used as light source (Ocean Optics, LH-2000), the light being inserted into the device through a multimode fiber optic with a core diameter of $105\mu\text{m}$ and numerical aperture N.A. = 0.22 (Thorlabs, M15L01 SMA-SMA Fiber Patch Cable); a second identical fiber optics was used as light collector. The positions of the fiber optics acting as source are described in Fig. 3.27(a) and Fig. 3.28(a). The fiber used as light collector was positioned in contact to the single output openings (O1,2,3,4 for the TIR splitter and O1,2,3 for the partial-refraction splitter). The analyses on the power efficiency were carried out connecting the collector optical fiber to a spectrophotometer (Ocean Optics, HR4000). Moreover, predisposition for light spots characterization was included in the experimental setup. A picture of the experimental setup is shown in Fig. 3.29.

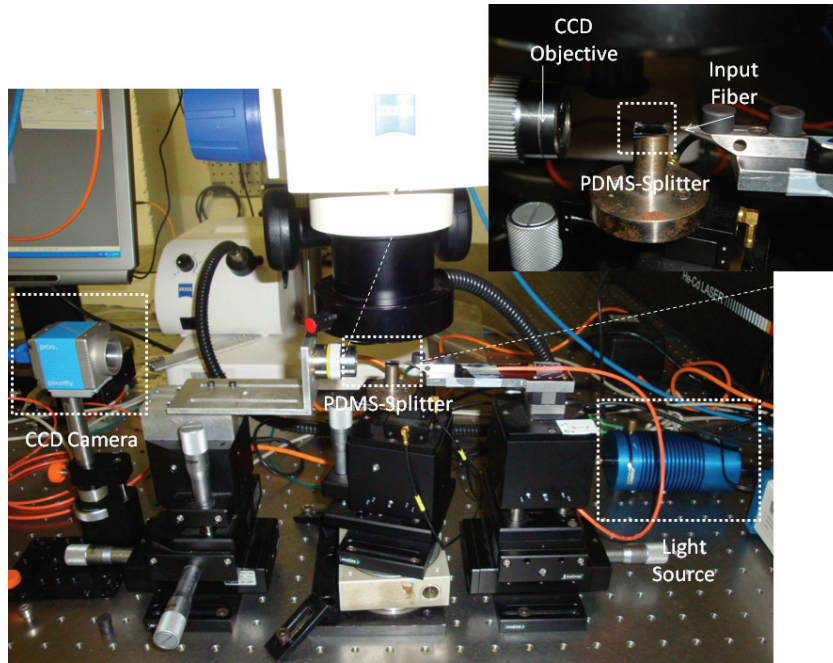


Fig. 3.29. Experimental setup.

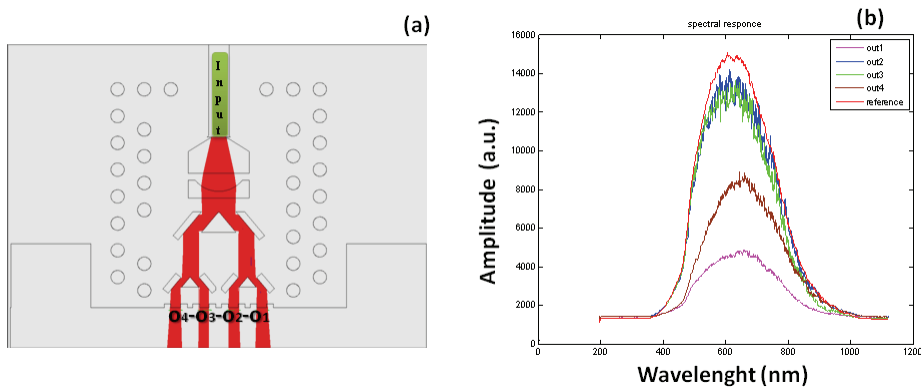


Fig. 3.30. TIR-based splitter. (a) Ray tracing simulation and (b) experimental spectral responses of each output.

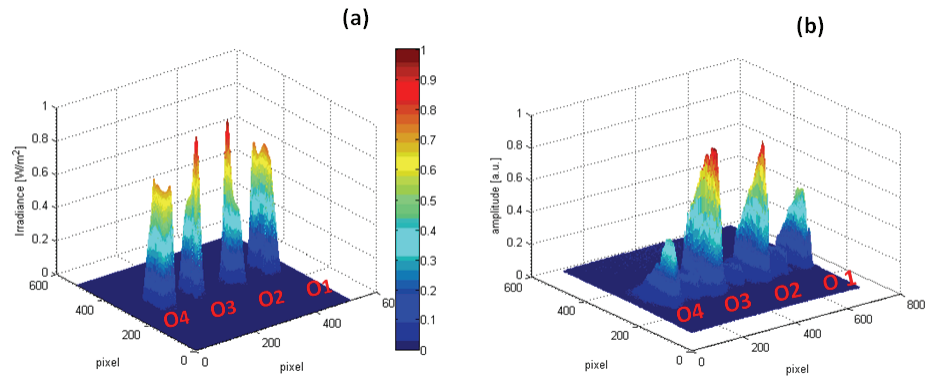


Fig. 3.31. Spatial visualization of the splitted beam from the right to the left side O4-3-2-1: (a) Simulated and (b) experimental.

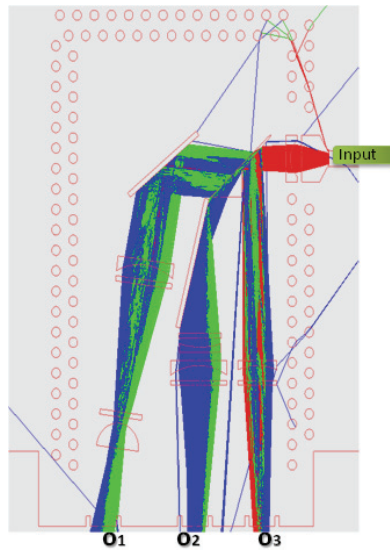


Fig. 3.32. Partial refraction-based splitter. Ray tracing simulation.

Such spatial light spots, due to splitting, is experimentally visualized by means of an objective (10X) positioned on the output surface of the splitters to capture the light coming from the output slits and projected onto a CCD array (Pixelfly, PCO imaging).

Splitter based on TIR

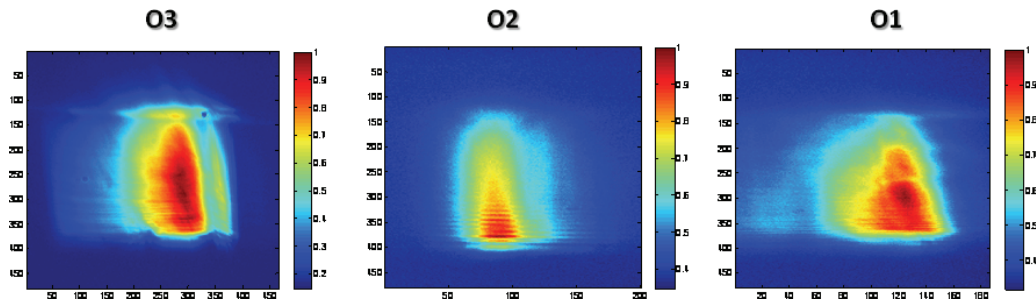


Fig. 3.33. Normalized experimental visualization of the spatial splitted beam for outlet O3, O2 and O1.

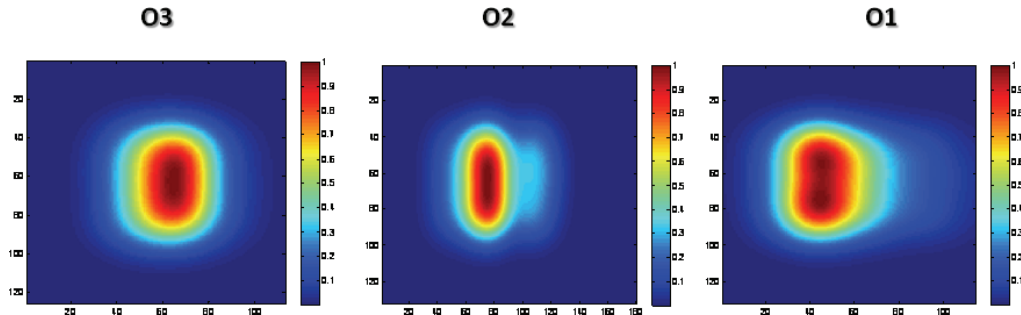


Fig. 3.34. Normalized spatial visualization of the simulated splitted beam for outlet O3, O2 and O1.

The simulation of the TIR splitter (Fig. 3.30(a)) shows how light coming from the optical fiber (Input) is collimated by the collimating lens. Then the input beam touches the first splitter S1 in TIR condition, that redirect it to the set of mirrors M1 and then again to the second set of splitter S2, S3, towards the output slits O1,2,3,4 through the mirrors M2,M3. The splitting is absolutely symmetrical and performs a division in four (1:4) of the input light beam. The analysis performed by the spectrophotometer shows how, in reality the inner outlets O2,3 collect higher power than the external ones (O1,4). The spectra also

show the transparency of the PDMS to all the wavelength of the light source by comparing the shape of the outlet spectra to reference (white light source). In Fig. 3.30(b) it is shown the spectral response related to each outlet versus the input wavelengths.

As additional analysis of the splitter device 1:4, a simulation of the light spots emerging from the output openings (surface O1,2,3,4) is shown in Fig. 3.31(a). It can be seen that the predicted profile for each output slit has an approximately rectangular shape corresponding to the slit size ($120 \mu\text{m} \times 70 \mu\text{m}$). Fig. 3.31(b) shows a normalized spatial profile in a color-coded 3D visualization consistent with the spectral response in Fig. 3.30(b). Such profile was extracted by images acquired through the objective and the CCD camera described before in the configuration setup. This visualization also show the differences between the external and the inner outlet performance. The differences between simulation and experimentation in Fig. 3.31 are based on slight misalliance of the input optical fiber position respect to the collimating lens.

Splitter based on partial refraction

The simulation of the splitter based on the partial refraction of the light beam clearly show the functional principle for the light splitting explained before (see Fig. 3.32). The light source is first collimated by the lens CLin and then divided in three by the asymmetric prism P1. Due to asymmetry of the splitter, the resulting beams are different in size and direction. Thus additional mirrors and lenses are used to model the output beams as desiderate. In particular the O1 beam is tilted of

an angle of 14° which is considered negligible. This result is evident looking on the light stain visualized during the experimentation by the CCD camera (see Fig. 3.33(a,b,c)). Simulated light spots emerging from the output openings (surface O1,2,3) is shown in Fig. 3.34(a,b,c). It can be seen that the predicted profile for each output slit has an approximately rectangular shape corresponding to the slit size ($120 \mu\text{m} \times 70 \mu\text{m}$). This visualization also highlights the differences between the three outlets. In particular the outlet O1 shows asymmetric features due to the tilted nature of the light beam.

3.4.5 Conclusions

The versatility offered by PDMS/air interfaces allow to introduce micro devices for light splitting. The presented micro-devices are capable to produce 1:4 and 1:3 beams. This property is interesting in microfluidic applications as for the monitoring and control of microfluidic spatial profiles especially of that involved in two-phase flow microfluidic systems (bubbles/droplets flow). The proposed devices can be used as external components (off-chip) but they also be integrated in a microfluidic platform (on chip approach). A successive study would be the experimental characterization of the devices' functionality for the monitoring of two-phase flow microfluidic systems and in particular for flow velocity measurements.

Nonlinear time series analysis of two-phase microfluidic flows

In this chapter we study by means of nonlinear analysis methods the complex dynamics of air bubbles carried by water and flowing in a microfluidic snake channel. Two kinds of input flow are considered: constant flow and periodic flow. A rich variety of dynamics was found from both flows, in relation to a wide experimental observation of bubbles' motion. Relation maps are identified, allowing the classification of dynamic flow patterns in terms of d-infinite and Largest Lyapunov exponent and to establish the couple Capillary number and Air Fraction (constant flow) or Capillary number and flow's frequency (periodic flow) as flow control parameters opening the way for the control of the bubble flow by signal processing.

4.1 Introduction

The manipulation of multiphase flows is a fundamental field of microfluidic systems. It enables the generation and manipulation of monodis-

persed bubbles [21][22] or droplets [59][58] of gas or liquid phase in a continuous liquid stream; these dispersions suggest new routes to the production of polymeric particles, emulsions and foams [66][16]. In this context the clear knowledge of involved microfluidic processes and the development of suitable control strategy are both critical points [31][49].

For small length scale the flow is almost laminar and a big effort is done to introduce methods for mixing reagents and also to classify a variety of flow patterns [54]. Two phase immiscible flow was exploited for an efficient mixing of samples. An example of mixing inside droplets was first introduced by Tice et al. [60][8]. They exploited the chaotic advection inside droplets to mix multiple reagents in isolated plugs, where winding microchannels were used to create unsteady fluid flow. This method allows transport of reagents with no dispersion and moreover chemical kinetic data acquisition. A successive study was performed by Sarrazin et al. [52] In this study it was developed a method of rapid mixing when two droplets of different reagents coalesce in a shifted way. Also in this study was necessary a bending channel to mix the substances efficiently.

Liquid-gas flow was introduced to simplify and copy with mixing processes [23][40]. When at the same time two laminar streams of liquids are co-injected in a microchannel, stretch and folding of segmented fluid are possible due to their hydrodynamic interactions with micro-bubbles.

In the study of microfluidic two-phase flow, another important is-

sue is the characterization of patterns' generation that can be assumed strictly related to the dynamics and characteristics of the bubbles'/droplets' flow [14]. Considering the case of two-phase flow driven by constant input stream, a great effort has done focusing the attention on transitional regimes and on the characteristics of the dispersed phase [16]. The main aim is to create dynamic and retroaction model for the control of these high nonlinear processes. In particular flow pattern formation is affected by several parameters (geometry and material of the microchannel, properties and flow rate of the fluid, etc...). One of the most important is the inner surface characteristics of microchannels (wettability) that control the shape of bubbles or droplets [16]. Moreover the conditions for monodispersity and polydispersity are investigated to have the desiderated foam topology, and coupling two microfluidic droplets emitters complex dynamic behaviors have found [2].

Mainly in all the experimental studies presented in literature the processes have been monitored through high speed CCD cameras and a successive image processing procedure has been developed for the extraction of parameters related to mixing of fluids both inside droplets or outside bubbles, droplets shape etc... Recently researches on droplets/bubbles formation addressing the potentiality of use a photo-diode monitoring system with the advantage of time series analysis for the extraction of volume, formation frequency and shape of droplets/bubbles [44]. Meanwhile nonlinear analysis of time series extracted from sequential images of a single micro-plug moving in a glass

capillary has proved the possibility of capturing the chaotic characteristics of plug motion under high switching frequency of a thermocapillary actuator [30]. As said before in the case of two phase flow driven by constant input, the wide literature available addresses extensively the problem of flow patterns generation and characterization meanwhile the study of immiscible two phase flow driven by periodic forcing is at an early stage. A recent work of Willaime et al. [65] shows experimentally how local periodic forcing may give rise to synchronized and quasiperiodic regimes of droplets' flow, organized into Arnold tongues. In this contest it is evident that the patterns formation are strongly influenced by input flow rate of fluids, and so they play a key role on process dynamics [31][49].

In this context the lack of theoretical frameworks and the high number of parameters involved in two-phase microfluidics lead the necessity of an experimental study supported by the nonlinear dynamic analysis methods [32]. Particularly in the present work we carried out an experimental study to investigate and quantify how the nonlinear behavior of bubbles' flow in a microchannel can be affected by constant or periodic input flows. The information on the *bubble flow* come from optical measures recorded by a photodiode-based circuits and converted into time series. Thus the aim is to understand the underlying nonlinear dynamics in relation to amplitude (constant flow) and frequency (periodic flow) of the input flow.

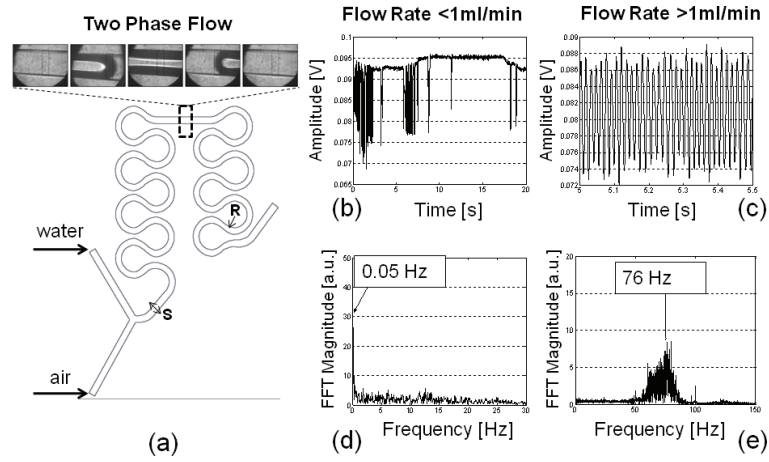


Fig. 4.1. (a) The microfluidic snake channel and the bubble flow pattern generation in the designed area. (b)-(c) Time series and (d)-(e) frequency spectra representative of bubbles passage respectively for $V_{air}=0.12$ ml/min, $V_{water}=0.63$ ml/min and for $V_{air}=1.2$ ml/min, $V_{water}=6.3$ ml/min.

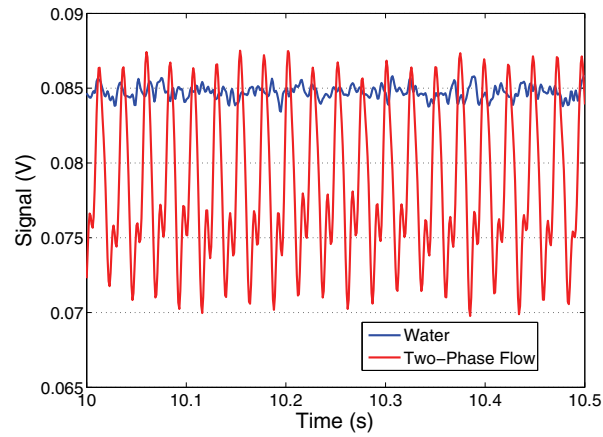


Fig. 4.2. Time signals related to two-phase flow dynamics ($V_{air}= 1.2$ ml/min, $V_{water}=2.26$ ml/min) and water flow ($V_{water}=2.26$ ml/min).

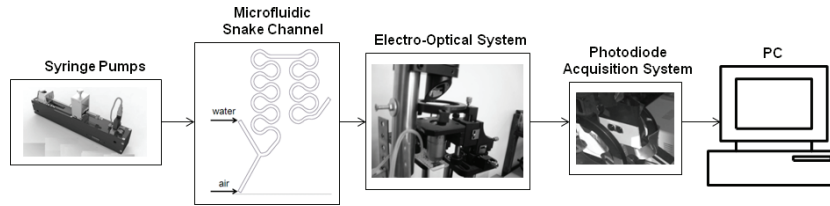


Fig. 4.3. Block representation of the experimental set-up: two syringe pumps are connected to the microfluidic channel inlets, the electro-optic system and the photodiode based circuit. A DAQ converts the light variation signals with a sample rate of 1 kHz to time series.

4.2 Experimental setup and campaigns

4.2.1 Constant input flow

Bubbles carried by deionized water were generated by tangential stress at the Y-junction of a snake microchannel made in COC (Cyclic Olefin Copolymer). It has section of $S=640 \mu\text{m}$ and internal radius of curvature of $R=1.28 \text{ mm}$ (Fig. 4.1(a))(Thinxxs, SMS0104). Constant flow rates (Syringe pumps, Nemesys) for air and deionized water was imposed at channel's inlets (Fig. 4.1(a)). The micrometric size of the microfluidic system requires an optical instrumentation for the image magnification so an *ad hoc* electro-optical system with x20 magnification objective was used. This optical system has allowed a parallel acquisition of the light intensity variation in a well defined area of the microchannel of $640 \mu\text{m} \times 935 \mu\text{m}$ (Fig. 4.1(a)), through a CCD system and a photodiode based circuit. The photodiode signals that average the light intensity in the designed area were then converted into a time series for a successive PC based analysis. The light intensity time series is strictly related to the bubble flow as highlighted in

the frame sequence of a bubble passage in the designed microchannel area reported in Fig. 4.1(a).

Four experimental campaigns were designed. Each experimental campaign consists of a set of 14 experiments in which one flow rate (V_{air} or V_{water}) is fixed and respectively the other is increased. In both experimental campaigns 1-2 flow rates are below 1 ml/min ($V \leq 1$ ml/min), while in both experimental campaigns 3-4 flow rates are one order of magnitude bigger ($V \geq 1$ ml/min).

Two examples of the light intensity time series extracted from the microfluidic process and their frequency spectra in both cases are shown in Fig. 4.1(b)-(d) for flow rate smaller than 1 ml/min ($V_{air}=0.12$ ml/min, $V_{water}=0.63$ ml/min) and, in Fig. 4.1(c)-(e) for flow rate bigger than 1 ml/min ($V_{air}=1.2$ ml/min, $V_{water}=6.3$ ml/min). Drastic changes can be noticed in both time series plots and frequency spectra. This allows to envision the possibility of flow patterns classification through time series analysis. A representative signal obtained from the bubbles' dynamics for $V_{air}=1.2$ ml/min and $V_{water}=2.26$ ml/min is compared to the time signal of only water flowing in the microchannel (see Fig. 4.2). It can be noticed that the bubbles' passage (red line in Fig. 4.2) change the intensity of the light due to absorption.

A schematic view of the experimental setup is shown in figure 4.3 while in details Fig. 4.4 shows a schematic view of flow rate variations in the four experimental campaigns: Campaign-1 ($V_{water}=0.15$ ml/min and $V_{air}=0.12-0.89$ ml/min); Campaign-2 ($V_{air}=0.12$ ml/min and $V_{water}=0.15-0.64$ ml/min); Campaign-3 ($V_{water}=1.5$ ml/min and

$V_{air}=1.2-8.99$ ml/min); Campaign-4 ($V_{air}=1.2$ ml/min and $V_{water}=1.5-6.4$ ml/min).

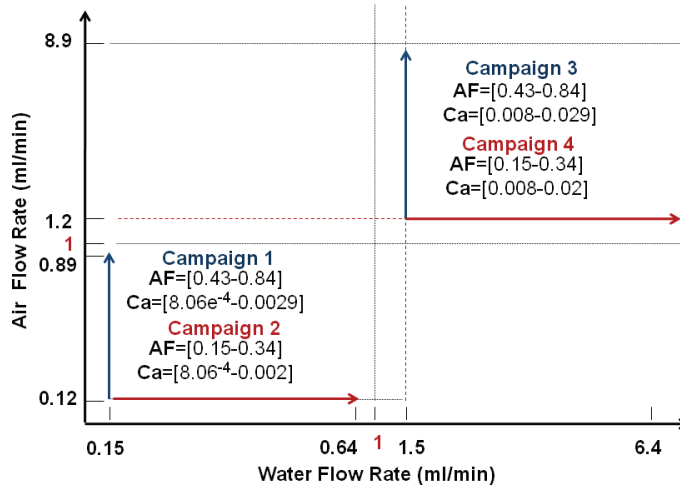


Fig. 4.4. Reconstruction in the Air Flow Rate - Water Flow Rate space of the four experimental campaigns for constant input flow: Campaign-1 (V_{water} fixed) and Campaign-2 (V_{air} fixed) with flow rates smaller than 1 ml/min; Campaign-3 (V_{water} fixed) and Campaign-4 (V_{air} fixed) with flow rates bigger than 1 ml/min.

All the 56 time series coming from the microfluidic experimentations were filtered with a low pass filter ($f_{cut}=20$ Hz for $V \leq 1$ ml/min and $f_{cut}=100$ Hz for $V \geq 1$ ml/min) and with a Notch filter to avoid unwanted components due to environmental light and electric noise.

4.2.2 Periodic input flow

The snake microchannel used is the same of the previous experimental campaign (constant flow) as well as the optical system (see Fig. 4.1(a)). Periodic flows for air and deionized water (following named as input

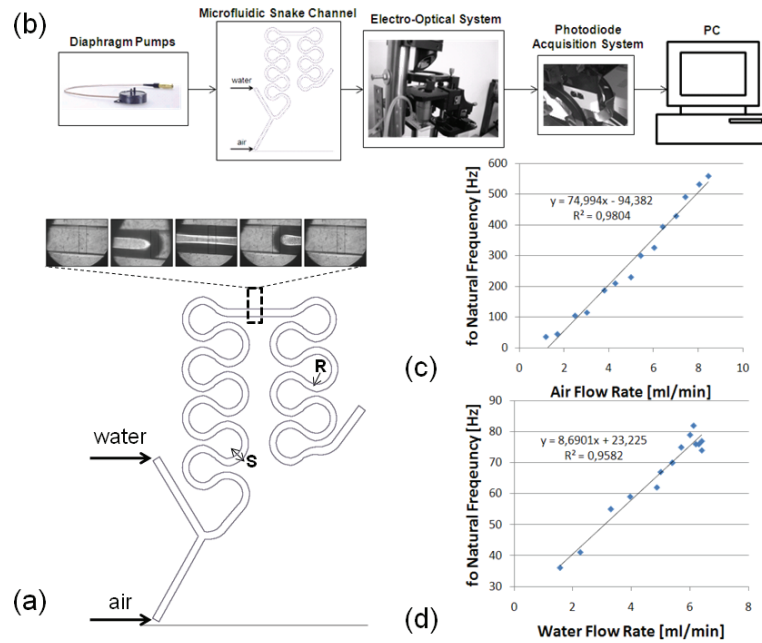


Fig. 4.5. (a) The microfluidic snake channel and the bubble flow pattern generation in the designed area. (b) Block diagram of the experimental setup. Natural frequencies of the two phase flow versus (c) air flow rate and (d) water flow rate.

flows) were imposed at channel's inlets (Fig. 4.5(a)) by means of two diaphragm pumps (TPS1304, Thinxxs). A schematic view of the experimental setup is shown in Fig. 4.5(b) while in Fig. 4.5(c)-(d) are shown the graphs of the natural frequencies versus the flow rates of the input fluids. The time series coming from the microfluidic experimentations for periodic input flow were filtered with a low pass filter ($f_{cut}=40$ Hz) and with a Notch filter to avoid unwanted components due to environmental light and electric noise. Fig. 4.6 shows the comparison between a time signal of the two-phase flow dynamics ($f_{water}=f_{air}=5$ Hz) and a signal obtained when the channel is filled with water. It is clear ob-

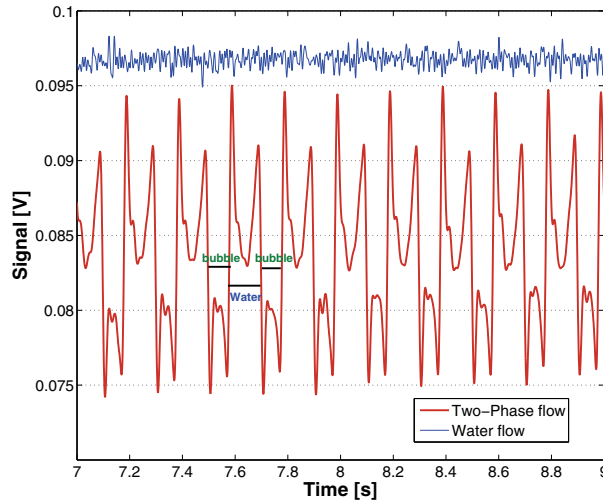


Fig. 4.6. Time signal of the two-phase flow for $f_{water}=f_{air}=5$ Hz (colored in red) and water flow (blue signal).

servicing Fig. 4.6 that the bubbles passage cause an absorption of light that decrease its intensity.

Two experimental campaigns were performed. Each experimental campaign consists of a set of 14 experiments in which one flow rate characterized by (f_{air}, V_{air}) or (f_{water}, V_{water}) is fixed and respectively the other is increased both in frequency and amplitude. It is worth to notice that the flow rate V_{fluid} is determined by controlling the frequency of the diaphragm pumps so we can considered as free parameters f_{air} and f_{water} . For all the experiments in Campaign-1 the frequency of water flow rate was fixed ($f_{water}=5$ Hz, $V_{water}=1.57$ ml/min) and the couple (f_{air}, V_{air}) was increased respectively in the ranges (5 Hz, 37 Hz) and (1.2 ml/min, 8.9 ml/min). Meanwhile in Campaign-2 the air flow

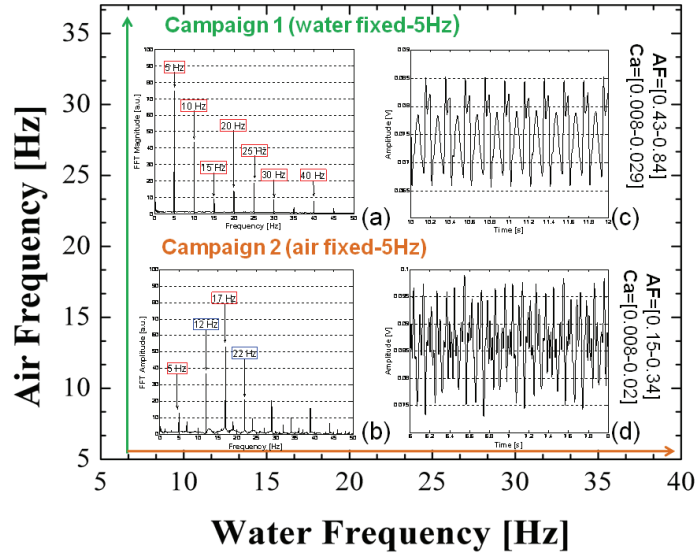


Fig. 4.7. Experimental Campaigns. In Campaign-1 $f_{water}=5$ Hz is fixed while f_{air} is varied; in Campaign-2 $f_{air}=5$ Hz is fixed and f_{water} is varied. (a) Typical Fourier power spectrum of the bubble flow and (c) time series dynamics for $f_{air}=5$ Hz and $V_{air}=1.2$ ml/min (Campaign-1). (b) Typical Fourier power spectrum and (d) time series dynamics for $f_{water}=7$ Hz and $V_{water}=2.26$ ml/min (Campaign-2).

rate frequency was fixed ($f_{air}=5$ Hz, $V_{air}=1.2$ ml/min) and the couple (f_{water} , V_{water}) was increased respectively in the ranges (5 Hz, 40 Hz) and (1.5 ml/min, 6.4 ml/min) (see Fig. 4.7). Two examples of Fourier frequency spectra and time series extracted from the microfluidic two phase flow process are shown in Fig. 4.7(a)-(c) for Campaign-1 ($f_{air}=5$ Hz, $V_{air}=0.12$ ml/min) and in Fig. 4.7(b)-(d) for Campaign-2 ($f_{water}=7$ Hz, $V_{water}=2.26$ ml/min). The frequency spectra show distinct peaks in both figures but only for fixed water flow ($f_{water}=5$ Hz, Campaign-1) peaks are mainly multiple values of f_{water} .

4.3 Dimensionless parameters

In microfluidic two-phase flow studies, two dimensionless parameters have been widely investigated for their influence in the control of mixing rate inside droplets [8] and in the characterization of flow patterns regime [14]; they are the Capillary Number (Ca) and the Air Fraction (AF). In particular being the microfluidic process largely dominated by the interfacial effects Ca enhances the relative importance of viscous to surface tension force meanwhile the AF highlights the fraction of the sample flow that is flushed in the micro-channel. Both parameters are evaluated in these experimental studies as follows [43]:

$$Ca = \frac{\mu(v_{air} + v_{water}) \cdot 0.5}{\sigma} \quad (4.1)$$

$$AF = \frac{V_{air}}{V_{air} + V_{water}}. \quad (4.2)$$

where μ is the dynamic viscosity of water, v is the typical velocity of the fluids, σ is the surface tension between air and water and V is the volumetric flow rate. The range of flow rates for the four designed experimental campaigns with constant flow rate leads to two ranges of variability for both Ca and AF as reported in Table 4.1. In our experimentation, for periodic flow, the range of chosen flow rate leads to the same range of capillary number (0.008, 0.029) for both campaigns and two ranges for the air fraction: (0.15, 0.34) for Campaign-2 and (0.43, 0.84) for Campaign-1.

Table 4.1. Capillary number and air fraction ranges for the experimental campaigns of constant input flow.

AF=0.43-0.84		AF=0.15-0.34		Ca=0.000806-0.0029		Ca=0.008-0.029	
Campaign 1	Campaign 2	Campaign 1	Campaign 3				
Campaign 3	Campaign 4	Campaign 2	Campaign 4				

4.4 Nonlinear time series analysis

Nonlinear time series analysis were applied to the experimental time series [32] in order to quantify the flow patterns and the bubbles' dynamics in terms of Largest Lyapunov exponent (LE) [1] and d-infinite parameter (d_∞) [7]. Lyapunov exponents are fully representative of the

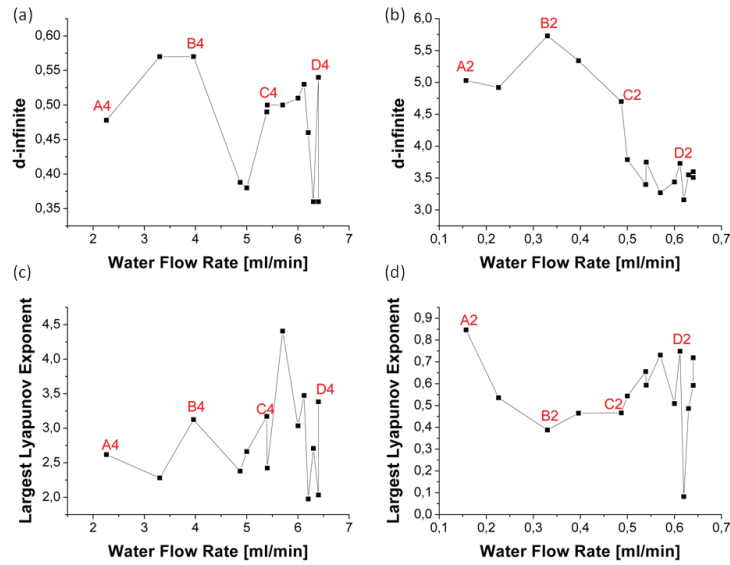


Fig. 4.8. Dynamics of the LE and d_∞ versus the varying water flow rate (air flow rate is fixed). (a) d_∞ versus water flow rate ($V_{water} \geq 1$ ml/min, Campaign 4), (b) d_∞ versus water flow rate ($V_{water} \leq 1$ ml/min, Campaign 2), (c) Largest Lyapunov Exponent versus water flow rate ($V_{water} \geq 1$ ml/min, Campaign 4), (d) Largest Lyapunov Exponent versus water flow rate ($V_{water} \leq 1$ ml/min, Campaign 2).

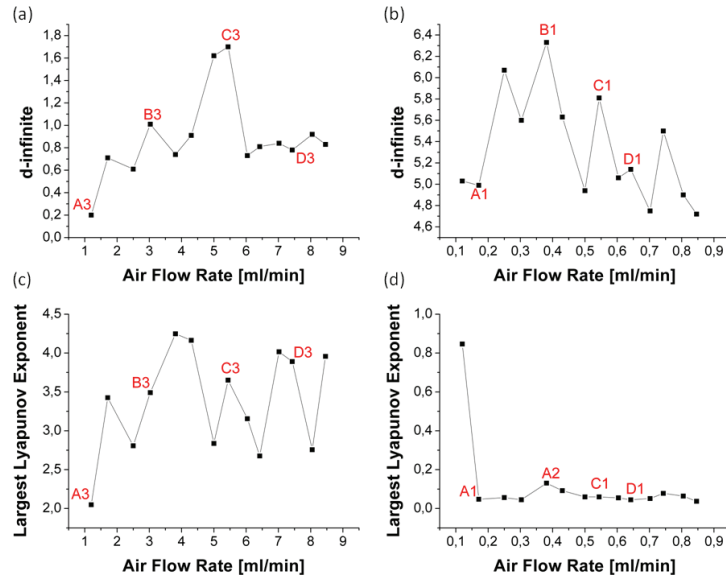


Fig. 4.9. Dynamics of the LE and d_∞ versus the varying air flow rate (water flow rate is fixed). (a) d-infinity versus air flow rate ($V_{air} \geq 1$ ml/min, Campaign 3), (b) d-infinity versus air flow rate ($V_{air} \leq 1$ ml/min, Campaign 1), (c) Largest Lyapunov Exponent versus air flow rate ($V_{air} \geq 1$ ml/min, Campaign 3), (d) Largest Lyapunov Exponent versus air flow rate ($V_{air} \leq 1$ ml/min, Campaign 1).

sensitivity to initial conditions (*stretching phase*) of a given nonlinear dynamical system, being positive for chaotic behaviors [56]. Often it is sufficient to establish the existence of at least one positive Lyapunov exponent to define chaotic dynamics [61]. Thus the Largest Lyapunov exponent quantify a degree of nonlinearity in the dynamical system while the d-infinity is sensible of both stretching and folding mechanism so it is not only a complementary measure to maximal Lyapunov exponent but also a robust parameter for time series corrupted by noise.

The relationship between Largest Lyapunov exponent λ and the divergence of j^{th} pair of nearest neighbors from a time series can be represented by the following relation [1]:

$$d_j(i) = C_j e^{\lambda(i\Delta t)} \quad (4.3)$$

where λ is the largest Lyapunov exponent and C_j is the initial separation between trajectories, i is the discrete time step and Δt the sampling period of the time series. Equation 4.3 is valid for a finite number of time-step after that the diverging curve saturates since the effects of *folding process* take place keeping all the trajectories bounded. Thus taking into account the evolution of the first order expansion of $d_j(i)$ and adding a second order term representative of the folding process, the asymptotic value d_∞ is defined as the non null fixed point of the following equation [7]:

$$d(i+1) = \Lambda d(i) - \Gamma d^2(i). \quad (4.4)$$

The Largest Lyapunov exponent is estimated through the finite size Lyapunov exponent method [1] and the d_∞ is expressed in terms of absolute value of d_∞ logarithm ($|\log(d_\infty)|$) [32]. It is worth to notice that the d_∞ obtained values are bounded in the range (0,1). Moreover the state space reconstruction was performed by the method of delays giving a geometrical identification of the microfluidic dynamics [32].

4.5 Results

4.5.1 Constant input flow

Detailed plots of dynamics of LE and d_∞ versus the varying flow rate (one flow rate is fixed) for all the experimental campaigns are shown in Fig. 4.8 and Fig. 4.9. In particular Fig. 4.8 reports the results for the Campaign 4-2 (air flow rate fixed) while Fig. 4.9 reports the results for the Campaign 3-1 (water flow rate fixed). At first sight comparing both parameter values of Campaigns for $V \geq 1$ ml/min (see figure Fig. 4.8(a) and Fig. 4.8(c)) with the Campaigns for $V \leq 1$ ml/min (see figure Fig. 4.8(b) and Fig. 4.8(d)) we can notice that for $V \geq 1$ ml/min the LE assumes values visible higher than in the first case. As expected the dynamic of the d_∞ parameter follows an inverse relationship respect to LE. This suggest that the nonlinearity of the bubble flow increase with the flow rate. Considering the nonlinear parameter trends in Fig. 4.9, we can assume the same results for the varying water flow rate: the nonlinearity of the flow increase with the flow rate.

To compare the results of all campaigns in a unique representation, the Largest Lyapunov Exponent and d_∞ were plotted versus the Capillary Number (Fig. 4.10) and the Air Fraction (Fig. 4.11). Capillary Number and Air Fraction are chosen as control parameters related to the input fluid flows. Both representations in Fig. 4.10 and Fig. 4.11 enhance the previous results. In Fig. 4.10 when the capillary number grows the dynamics of bubbles changes quickly toward high nonlinear dynamics as confirmed by the LE and d_∞ values, therefore we can iden-

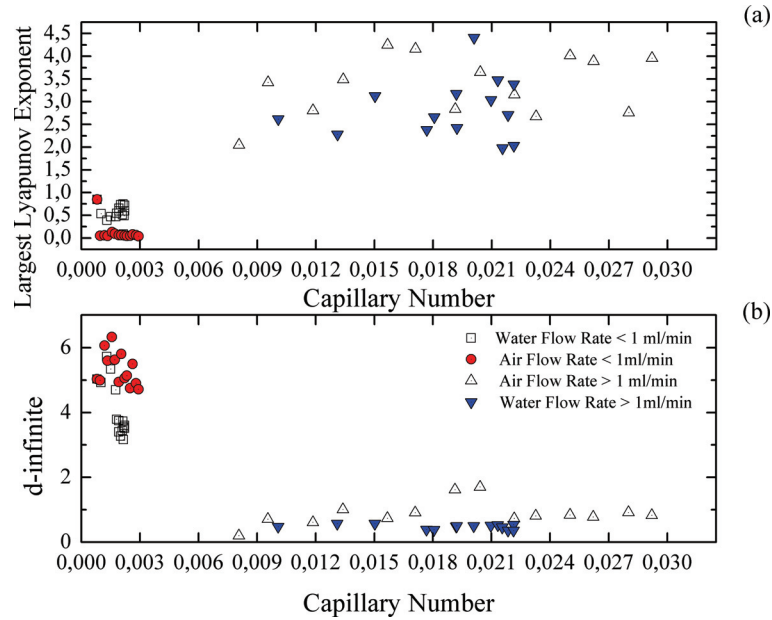


Fig. 4.10. (a) Largest Lyapunov exponent versus Ca . For $Ca \leq 0.003$ ($V \leq 1$) the dynamics of bubbles presents values in the range (0, 1) meanwhile for $Ca \geq 0.003$ ($V \geq 1$) the range is (2, 5). (b) d -infinite versus Ca . For $Ca \leq 0.003$ ($V \leq 1$) the dynamics of bubbles presents values in the range (0, 2) meanwhile for $Ca \geq 0.003$ ($V \geq 1$) the range is (3, 6).

tify a sort of bifurcation value in the range (0.003, 0.006) in which there is a jump in the values assumed by both LE and d_∞ . At the same time Fig. 4.11 allows to focus the attention on a second aspect which is the varying flow rate (air or water). With this representation it is possible to classify all four campaigns and we can identify on the y-axis two levels of values for both LE and d -infinite in relation to the campaigns for $V \leq 1$ ml/min and $V \geq 1$ ml/min. Furthermore the x-axis is referred to the proportion related to fluids' flow rates. Despite the Air Fraction is useful to discriminate all the experimental campaigns, it shows a limit if used for experiment design indeed, fixing an air fraction value

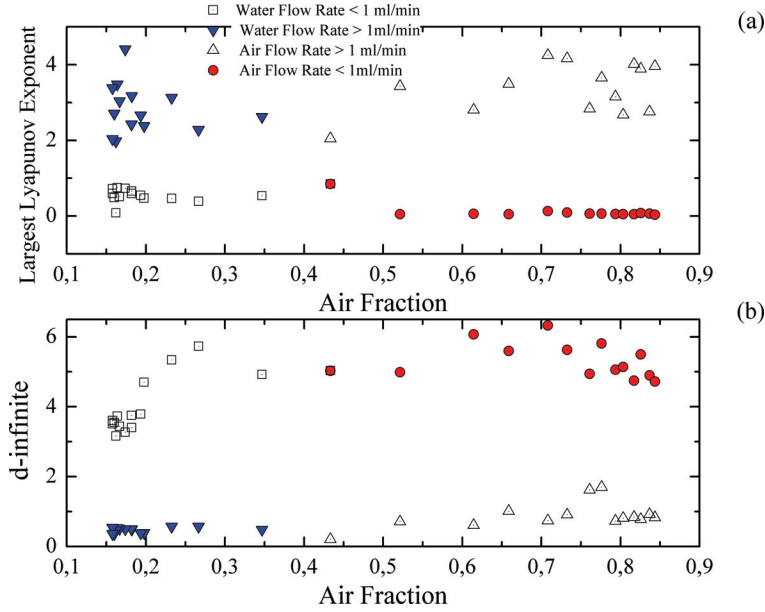


Fig. 4.11. Campaigns 2 and 4 have $AF \leq 0.4$ and Campaigns 1 and 3 have $AF \geq 0.4$. (a) Largest Lyapunov exponent versus AF. For $(V \leq 1)$ the dynamics of bubbles presents values in the range $(0, 1)$ meanwhile for $Ca \geq 0.003$ ($V \geq 1$) the range is $(2, 5)$. (b) d-infinite versus Ca. For $Ca \leq 0.003$ ($V \leq 1$) the dynamics of bubbles presents values in the range $(0, 2)$ meanwhile for $Ca \geq 0.003$ ($V \geq 1$) range is $(3, 6)$.

we could find different dynamics. For this reason in figure 4.12 it is proposed a further representation that takes into account both control parameters (Ca, AF) respectively in the x-axis and y-axis and in which values of nonlinear indicators (LE or d_∞) are coded through a color-map. In this space a set of 4 selected experiments are indicated (A_j, B_j, C_j, D_j) for each Campaign $j=1 \dots 4$.

In both Fig. 4.12(a)-(b) it is possible to distinguish four areas one for each campaign. Moreover for the selected experiments the state space representation was reconstructed from the light intensity time series.

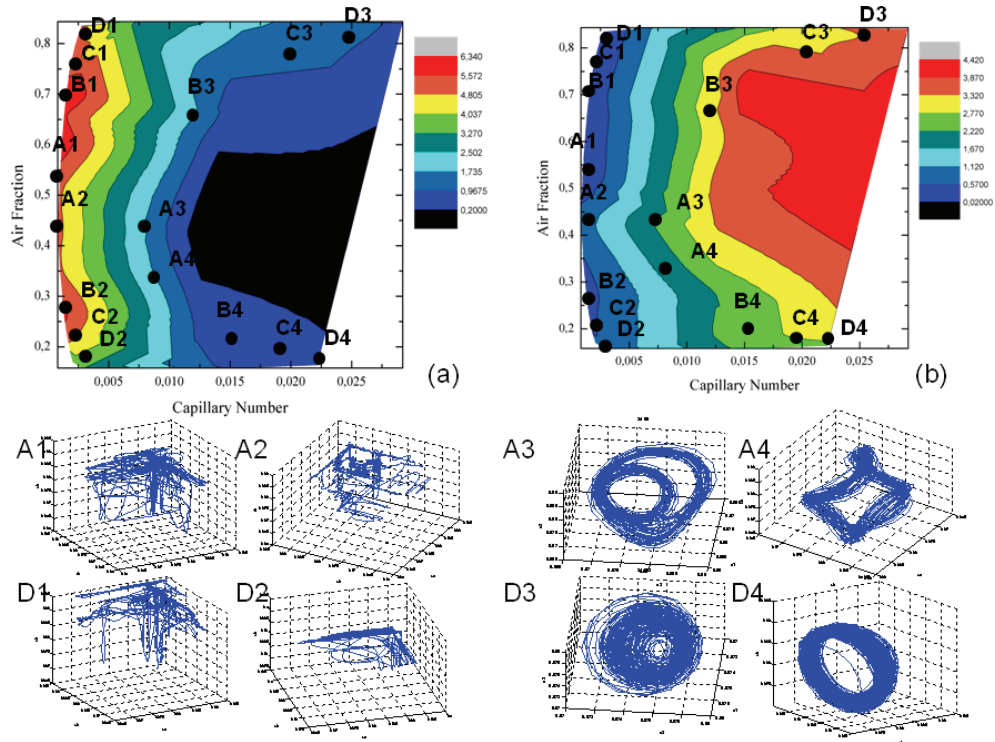


Fig. 4.12. Contour plot of (a) d -infinity versus Ca and AF . (b) LE versus Ca and AF . State space representation of eight selected experiments: A_1 ($V_{air}=0.17$ ml/min, $V_{water}=0.15$ ml/min), D_1 ($V_{air}=0.64$ ml/min, $V_{water}=0.15$ ml/min), A_2 ($V_{air}=0.12$ ml/min, $V_{water}=0.15$ ml/min), D_2 ($V_{air}=0.12$ ml/min, $V_{water}=0.61$ ml/min), A_3 ($V_{air}=1.2$ ml/min, $V_{water}=1.57$ ml/min), D_3 ($V_{air}=7.43$ ml/min, $V_{water}=1.57$ ml/min), A_4 ($V_{air}=1.2$ ml/min, $V_{water}=2.26$ ml/min), D_4 ($V_{air}=1.2$ ml/min, $V_{water}=6.4$ ml/min)

As examples the attractors obtained in relation to the experiments A_j - D_j ($j=1..4$) are reported in the bottom part of Fig. 4.12. The evidence in the difference of the state space representations is consistent with all the previous results (two classes: one for $V \leq 1$ ml/min and $V \geq 1$ ml/min) and enhances the sensitivity of bubble flow dynamics to the increment of the Capillary number and so the input flow rate.

4.5.2 Periodic input flow

Given the time series related to the bubbles' flow in the selected area, the signal processing procedure adopted for periodic flow is based on: Fourier analysis and nonlinear time series analysis.

Fourier analysis

As for Fourier analysis, we used the notation of f_{max} and A_{max} respectively for the resonance frequency and its amplitude. The Fig. 4.13(a) plots A_{max} versus the frequency of input varying flow for all experiments. For each campaign results were further classified taking into account if the frequencies of the input flows were multiple or not. It can be noticed that the amplitude A_{max} follows the same trend for both campaigns: A_{max} decreases with the input frequency, and the plateau region in the range (20 Hz, 33 Hz) can be related to the Ca trend (see Fig. 4.13(c)). Fig. 4.13(b) shows the comparison between the spectral response in terms of f_{max}/f_{input} versus the frequency of the varying input. It is worth to notice that for both campaigns f_{max}/f_{input} has a maximum of 1 ($f_{max}=f_{input}$) at low input frequencies and then decreases. Meanwhile a great difference is evident looking at the trends considering that Campaign-1 shows an exponential decay, while Campaign-2 a piece-wise linear function. In this representation, as expected, only Campaign-2 is affected by changes related to the Ca trend (see Fig. 4.13(c)).

In histograms (see Fig. 4.14 (a)-(b)) the results of both campaigns were grouped to polarize the attention on the output flow sensitivity considering if the frequency of the input flows is multiple or not.

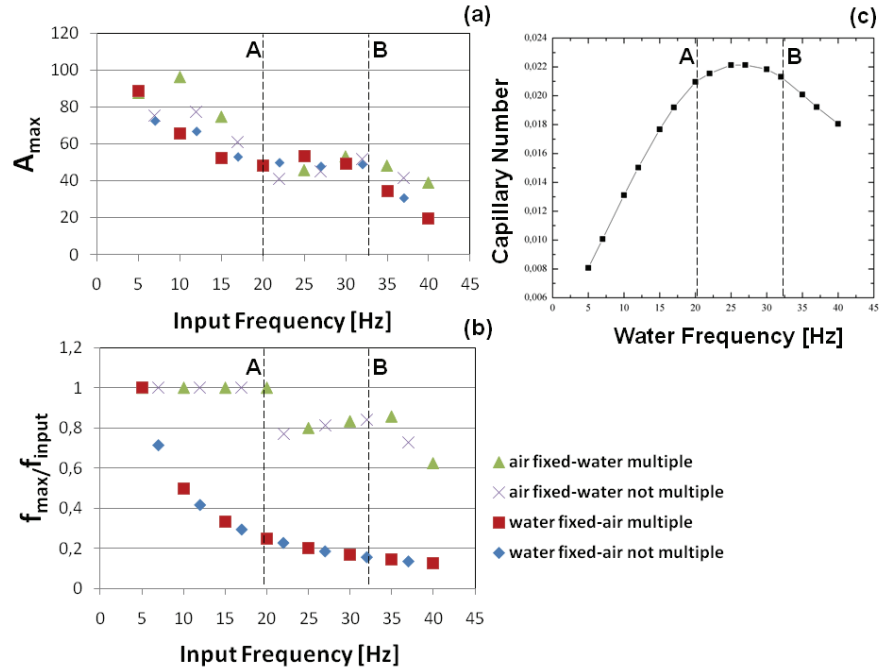


Fig. 4.13. (a) Amplitude A_{max} versus the frequency of varying input flow and (b) normalized resonance frequency f_{max} versus the frequency of varying input flow. (c) Capillary number versus water flow frequency. The strong slope changes are in point A and B.

In figure 4.14(a) we show the total number of components identified in each spectrum bigger than 10 arbitrary units. The number of frequency components is mainly the same. We can read a richness of spectra at low input frequencies for not-multiple experiments and at high input frequencies in all cases. This distinction can be enhanced in Fig. 4.14(b) where there are the number of occurrences of a specific frequency (as reported on the x-axis) in each spectrum of the output flow. It is worth to notice that a broad-band histogram will be obtained if the frequencies of the input flows are not-multiple.

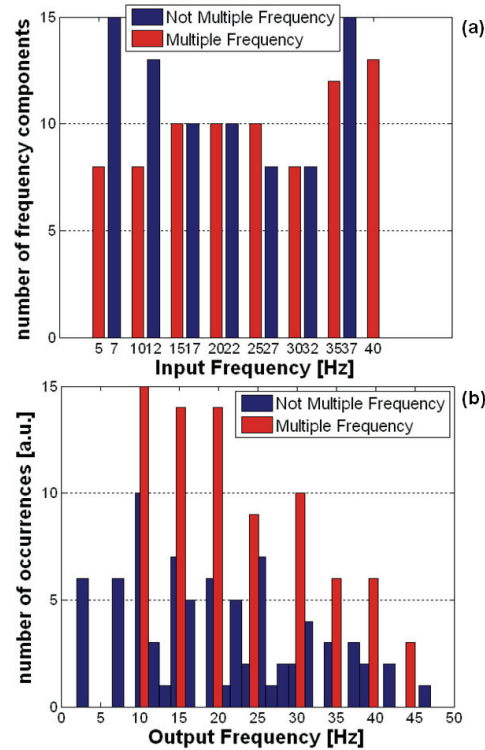


Fig. 4.14. (a) Number of frequency components versus input frequency .(b) Frequency occurrences in spectra of output flow. The classification is related if the input periodic flows (air and water) are multiple or not-multiple

Nonlinear time series analysis

The nonlinear analysis developed in this second phase clarifies the previous results and enhances the possibility to classify the two phase flow.

Figure 4.15 shows two nonlinear parameters (d -infinite and LE) versus input frequency. When the air flow rate and frequency are fixed the d -infinite values decrease with the frequency (Fig. 4.15(a)), while when the water frequency is fixed the d -infinite values are almost constant (Fig. 4.15(a)). In figure 4.15(b) the associated Largest Lyapunov ex-

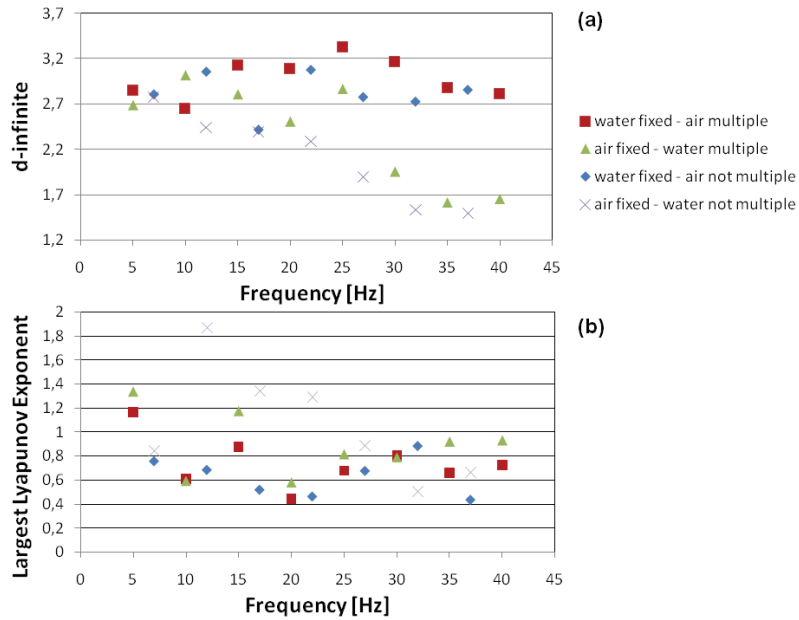


Fig. 4.15. (a) d-infinite versus flow rate frequency; (b) Largest Lyapunov exponent versus flow rate frequency.

ponents versus the input frequency show a trend that for all campaigns tend to collapse in the same curve for high input flow rate frequency. Comparing the two figure (Fig. 4.15(a)-(b)) it is evident that d-infinite parameter is more sensitive than Largest Lyapunov exponent in discriminating the bubbles' dynamics so d_∞ could represent a good candidate for the distinction of the bubbles' dynamics from time series. Figure 4.16 shows the same nonlinear parameters (d-infinite and LE) versus the AF. In Fig. 4.16(a) two regions are highlighted: air flow rate fixed ($AF \leq 0.4$) and water flow rate fixed ($AF \geq 0.4$). The same distinction is evident in Fig. 4.16(b).

In figures 4.17 and 4.18 it is proposed a further representation that

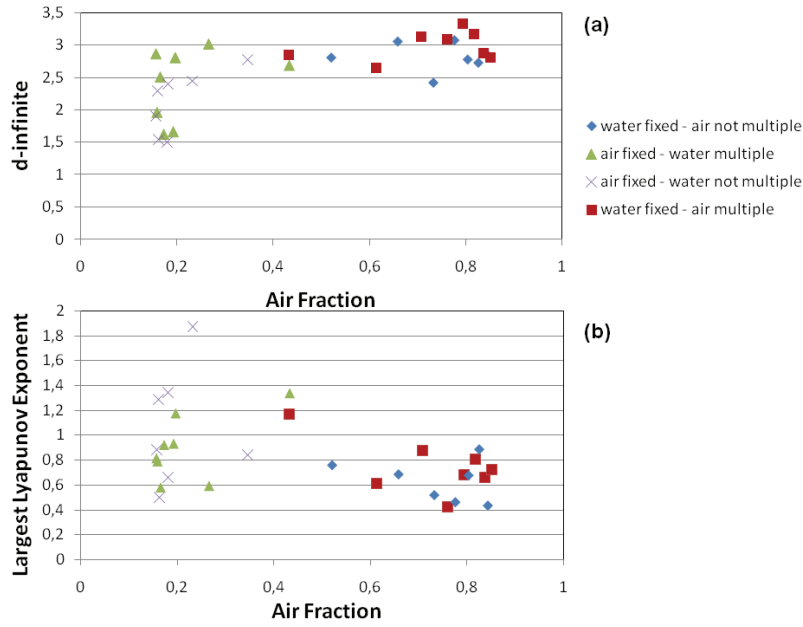


Fig. 4.16. (a) d -infinite versus AF; (b) Largest Lyapunov exponent versus AF.

takes into account the effects of both control parameters frequency and Air Fraction (f , AF) respectively in the x-axis and y-axis and in which values of nonlinear indicators (LE or d_∞) are coded through a color-map. Remembering that $1 < d_\infty < 0$ and in the plot it is reported $|\log(d_\infty)|$, we can assume that low values of d_∞ are associated to high level of nonlinearity. In Particular for Campaign-1 considering both d_∞ and LE, figure 4.17 indicates that high nonlinear dynamics is reached for low air flow rate frequency (5 Hz, 15 Hz) and for AF in the range (0.45, 0.55). The dots (A_1 , A_2 , A_3 , A_4 , A_5) are related to a set of 5 experiments selected for state space reconstruction (bottom inset in Fig. 4.17). All attractors show similar geometric characteristics. Meanwhile for Campaign-2 (air flow rate fixed) the phase diagram

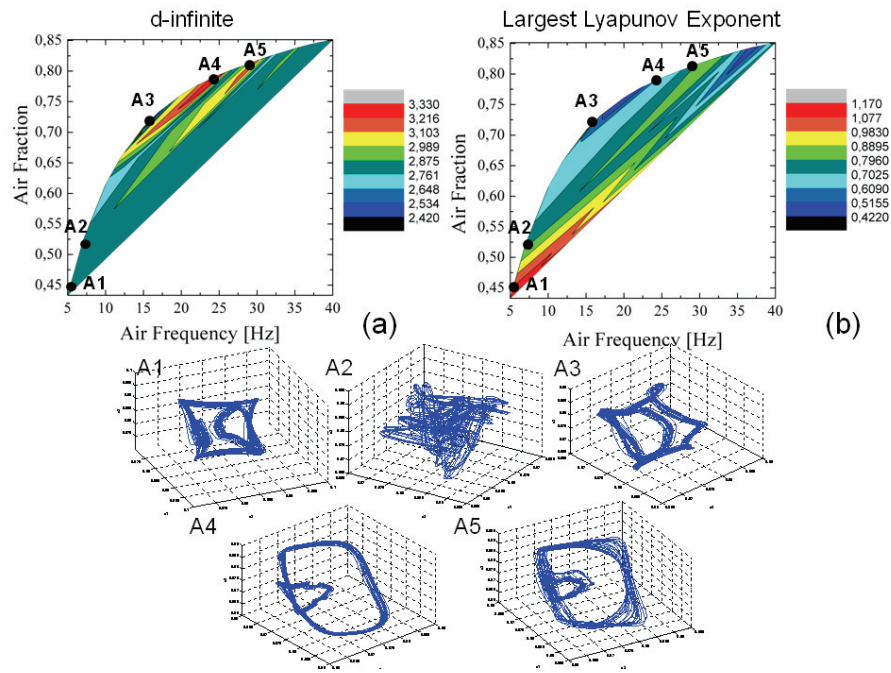


Fig. 4.17. Phase diagrams for Campaign-1 (water flow fixed). (a) d-infinite versus air flow frequency and AF; (b) Largest Lyapunov exponent versus air flow frequency and AF. A_1 , A_2 , A_3 , A_4 , A_5 are related to the state space reconstruction reported below.

in Fig. 4.18(a) shows a decreasing trend of the d-infinite as the frequency of the water flow rate increases. Taking into account both the d-infinite values (see Fig. 4.18(a)) and LE (see Fig. 4.18(b)) then higher nonlinearity in the dynamics of bubbles' flow are possible for water flow rate frequency in the range (12 Hz, 20 Hz) and AF in the range (0.15, 0.25). For the Campaign-2 a wider variety of dynamics is possible as it can be observed by the set of 3 experiments selected (A_1 , A_2 , A_3) for attractors reconstruction (bottom inset in Fig. 4.18). They different geometrical characteristics give an idea of the emerging nonlinear

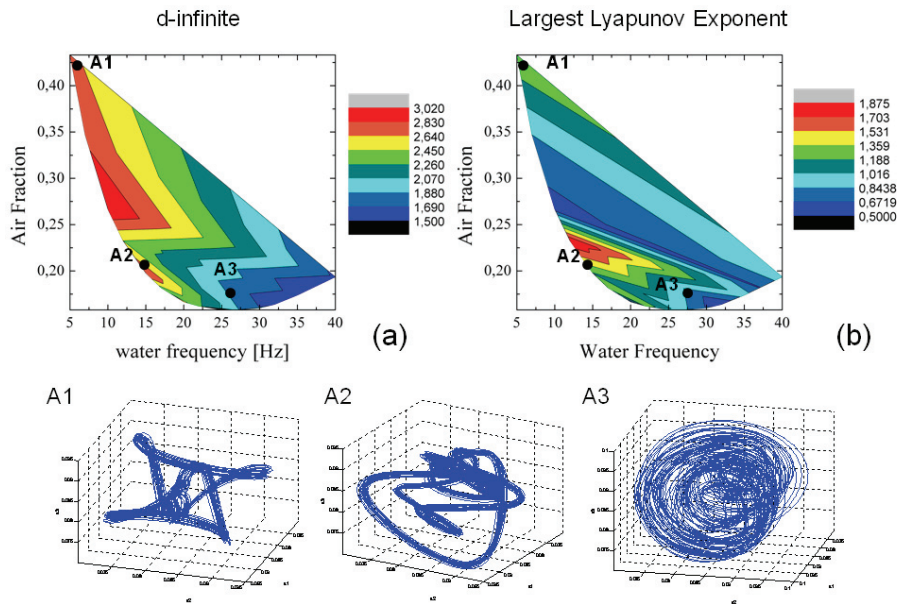


Fig. 4.18. Phase diagrams for Campaign-2 (air flow rate fixed), (a) d-infinite versus water flow frequency and AF; (b) Largest Lyapunov exponent versus water flow frequency and AF. A_1 , A_2 , A_3 , are related to the state space reconstruction reported below.

dynamics of bubbles by varying the water flow rate both in amplitude and frequency.

4.6 Conclusions

Droplets/bubbles formation is on the basic layer for the development of efficient Lab on a Chip systems. This study presents the potentiality of time series analysis to identify bubble dynamics in two-phase microfluidic processes. Reminding that process monitoring is a fundamental step in the development of an all-suffice and portable LOC

system, these results can represent great advantages both from its technological and information processing perspectives. It is widely recognized that the two-phase microfluidics involves nonlinear phenomena and the reconstructed phase diagrams represent an attempt to quantify and classify them. In particular it has been considered the evolution of two nonlinear parameters as the Largest Lyapunov exponent and the d-infinite versus parameters characteristic in the study of bubble flow, as Capillary Number, Air Fraction and frequency of the flow. These results simplify the identification of the bubbles' flow dynamics, allowing by fix a couple (Ca, AF) or (Ca, f) to derive its nonlinearity. It is important to underline that the experimental campaigns were designed assuming the input streams both for air and water to be constant flow and also periodic input flows. Moreover the present study could give an insight on the possibility to investigate on the inner bubble nonlinearity due to the mixing process directly through their flow dynamics. In this direction the Capillary number and Air Fraction could be consider as control input parameters that not only affect the mixing rate inside droplets but also their complex temporal dynamics in microchannel. The proposed identification could be exploited as control system method for bubble flow switching toward different flow patterns.

Two-phase flow identification

In this chapter, the dynamical model identification for the asymptotic time signals belonging to a microfluidic two-phase flow process is presented. The time signals are used to synchronize another system with known mathematical model: the Chua's oscillator. This system has been chosen for its simple mathematical structure and for the possibility, respect to other chaotic systems, of mapping various nonlinear experimental phenomena. Moreover genetic algorithm was exploited for parameters estimation of the Chua's oscillator in relation to an optimization index that takes into account the synchronization of master (microfluidic system) and slave system (Chua's oscillator).

5.1 Experimental microfluidic two-phase flow

Bubbles carried by deionized water were generated by tangential stress at the Y-junction of a snake microchannel made in COC (Cyclic Olefin

Copolymer). It has section of $S=640 \mu\text{m}$ and internal radius of curvature of $R=1.28 \text{ mm}$ (Fig. 5.1)(Thinxxs, SMS0104). Constant flow rates (Syringe pumps, Nemesys) for air and deionized water was imposed at channel's inlets. The micrometric size of the microfluidic system requires an optical instrumentation for the image magnification so an *ad hoc* electro-optical system with x20 magnification objective was used. This optical system has allowed a parallel acquisition of the light intensity variation in a well defined area of the microchannel of $640 \mu\text{m} \times 935 \mu\text{m}$ (Fig. 5.1), through a CCD system and a photodiode based circuit that converts light variations into voltage signals. The photodiode signals that average the light intensity in the designed area were then converted into a time series for a successive PC based analysis. A block scheme of the experimental setup is shown in Fig. 5.2. The light intensity time series is strictly related to the bubble flow as highlighted in the frame sequence of a bubble passage in the designed microchannel area reported in Fig. 5.1.

Therefore in the study here presented time series from the microfluidic two-phase flow process are considered representative of its dynamics that in the following we indicate as *bubble flow*. In particular we consider the experimental campaign in which the air flow rate V_{air} is fixed at 1.2 ml/min and the water flow rate V_{water} is increased progressively from 1.5 ml/min to 6.4 ml/min obtaining 14 experiments.

Bubble flows are recorded for a time period of 20 s. An example of time series and Fourier spectrum from the microfluidic *bubble flow* is shown in Fig. 5.3(a-b) obtained for input flow rate $V_{air}= 1.2 \text{ ml/min}$

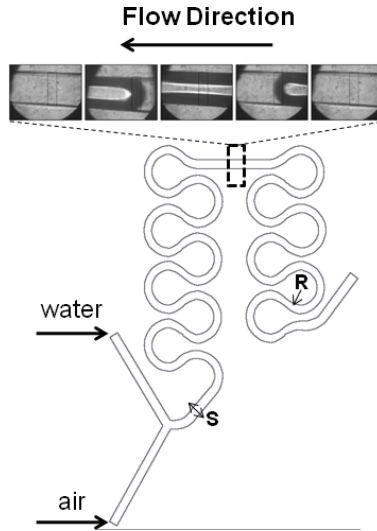


Fig. 5.1. The microfluidic snake channel and the bubble flow pattern generation in the designed area of $640 \mu\text{m} \times 935 \mu\text{m}$. The section of the microfluidic channel is $S=640 \mu\text{m}$ while the internal radius of curvature is $R=1.28 \text{ mm}$.

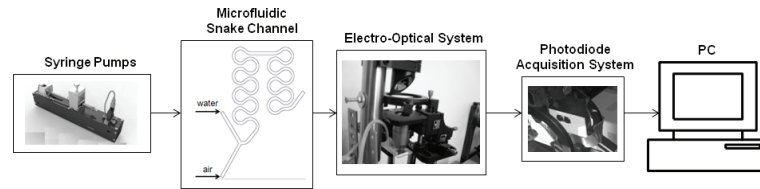


Fig. 5.2. Block representation of the experimental set-up: two syringe pumps are connected to the microfluidic channel inlets, the electro-optic system and the photodiode based circuit. A DAQ converts the light variation signals with a sample rate of 1 kHz to time series.

and $V_{water}=3.96 \text{ ml/min}$. The oscillating dynamics of the signal is related to the bubbles' passage in the specific location of the acquisition. For this example the Largest Lyapunov exponent is 3.12 while the d-infinite is -0.57. In a previous work [53] we have demonstrated that the two-phase flow process under study is nonlinear through nonlinear time

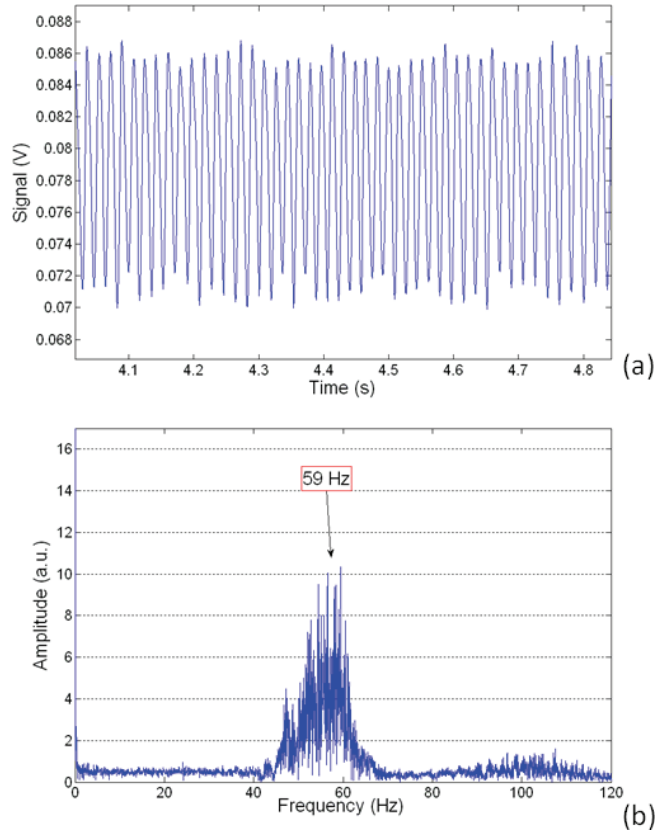


Fig. 5.3. (a) Time signal related to two-phase flow dynamics for air flow rate $V_{air}=1.2$ ml/min and water flow rate $V_{water}=3.96$ ml/min (red line). (b) Fourier spectrum of the signal.

series analysis and that the selected experimental campaign has Largest Lyapunov exponents in the same range. As visual approach, it is helpful to give a geometrical identification of the process under study. In Fig. 5.4 are depicted the state space reconstructions of the time series for the 6 selected experiments. They show a toroidal structure.

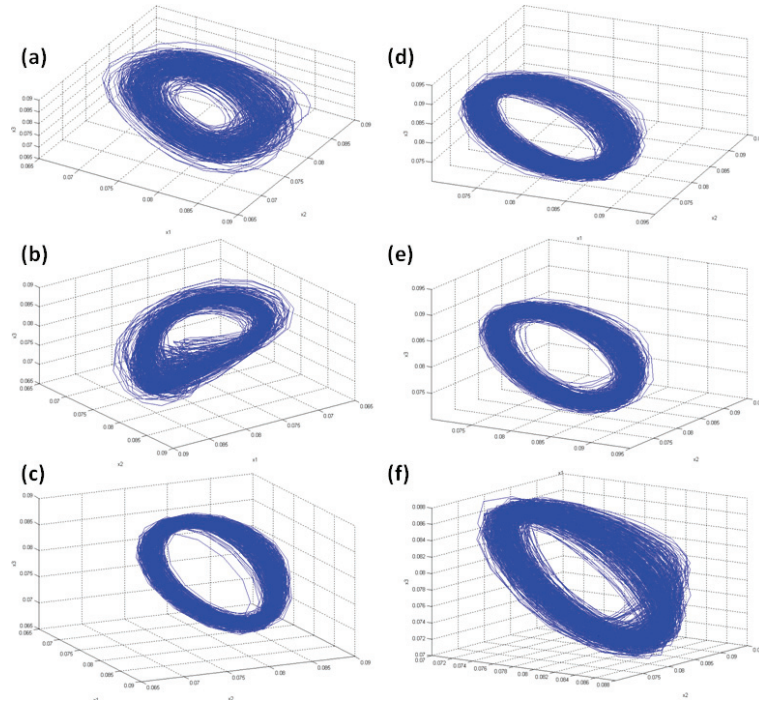


Fig. 5.4. Attractors of 6 microfluidic experiments:(a) $V_{air}= 1.2$ ml/min, $V_{water}= 3.3$ ml/min, (b) $V_{air}= 1.2$ ml/min, $V_{water}= 3.9$ ml/min, (c) $V_{air}= 1.2$ ml/min, $V_{water}= 5.3$ ml/min, (d) $V_{air}= 1.2$ ml/min, $V_{water}= 6$ ml/min, (e) $V_{air}= 1.2$ ml/min, $V_{water}= 6.4$ ml/min, (f) $V_{air}= 1.2$ ml/min, $V_{water}= 6.45$ ml/min.

5.2 The Chua's oscillator

In the study here presented the Chua's oscillator is chose for the similarity of its attractor (see Fig. 5.5) for $\alpha=1800$, $\beta=1000$, $\gamma=0$, $m_0=-1.026$, and $m_1=-0.982$ with the attractors reconstructed from the microfluidic experimental *bubble flow*. Moreover the state equations of Chua's system are topologically conjugate to a 21-parameter family of continuous odd-symmetric piecewise-linear equation in R^3 , so virtually every known third-order odd symmetric chaotic autonomous system with 3

equilibrium points can be modeled by a Chua's oscillator [39] having the same qualitative behavior. The dimensionless state equation of the Chua's oscillator are:

$$\begin{aligned}
 \frac{dx}{d\tau} &= k\alpha(y - x - f(x)) \\
 \frac{dy}{d\tau} &= k(x - y + z) \\
 \frac{dz}{d\tau} &= k(-\beta y - \gamma z), \\
 f(x) &= m_1 + \frac{1}{2}(m_0 - m_1) \{ |x + 1| - |x - 1| \}
 \end{aligned} \tag{5.1}$$

where x, y , and z are the state variables and $\alpha, \beta, \gamma, m_0$ and m_1 the system parameters. In Fig. 5.6 are represented the x (Fig. 5.6(a)), y (Fig. 5.6(b)), and z (Fig. 5.6(c)) state variables of the Chua's oscillator for the selected parameters: $\alpha=1800, \beta=1000, \gamma=0, m_0=-1.026$, and $m_1=-0.982$. For the identification purposes we considered the y state variable of the Chua's system to compare with the microfluidic time series in the optimization procedure because it presents an amplitude trend similar to the optical signal related to the *bubble flow*. The Fourier spectra of the state variables are shown in Fig. 5.7. Thus one advantage of Chua's oscillator over other systems is that it is the only known physical system whose mathematical model is capable of duplicating almost all experimentally observed phenomena, and which has been proved to be chaotic in a rigorous mathematical sense [39].

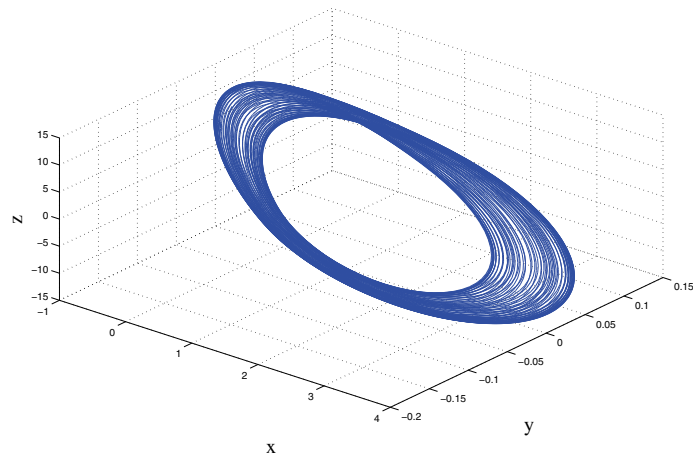


Fig. 5.5. Chua's attractor for $\alpha=1800$, $\beta=1000$, $\gamma=0$, $m_0=-1.026$, and $m_1=-0.982$.

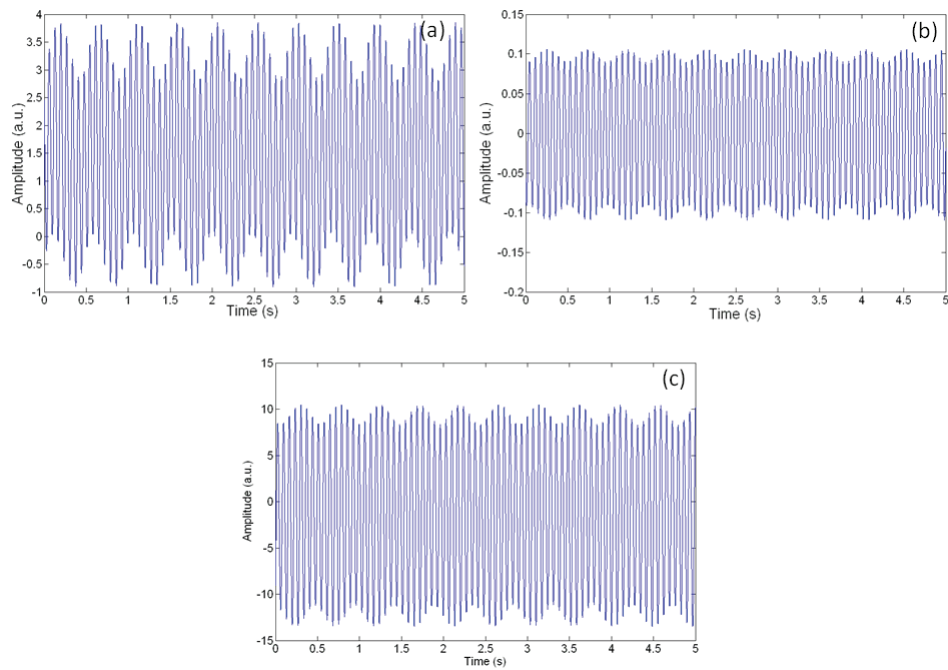


Fig. 5.6. Chua's time series for $\alpha=1800$, $\beta=1000$, $\gamma=0$, $m_0=-1.026$, and $m_1=-0.982$. (a) x state variable, (b) y state variable, (c) z state variable.

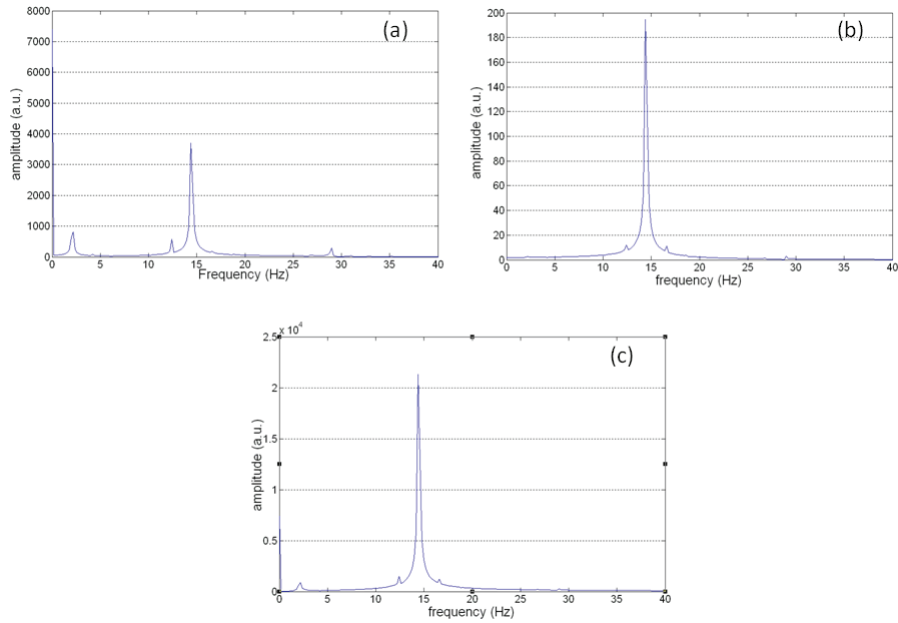


Fig. 5.7. Fourier spectra for (a) x state variable, (b) y state variable, (c) z state variable. The parameters of the systems are $\alpha=1800$, $\beta=1000$, $\gamma=0$, $m_0=-1.026$, and $m_1=-0.982$.

5.3 Microfluidic process identification

5.3.1 Synchronization of nonlinear systems

The concept of synchronization is ubiquitous in nonlinear systems [28]. The word comes from the greek roots $\sigma\nu\gamma$ (to share) and $\chi\rho\nu\nu\omicron\varsigma$ (time) meaning exactly "to share the same time". This concept was introduced in the 17th century by Christiaan Huygens (1629-1695), the inventor of pendulum clocks. Synchronization of chaotic systems, i.e. the regime in which two or more chaotic oscillators evolve following the same chaotic trajectory despite their different initial conditions, is a very interesting dynamical behavior studied under many points of view from secure communication systems to the transmission of digital sig-

nals [28]. However, when dealing with chaotic systems, synchronization is a non trivial concept. One of the chaos property was its sensitivity to the initial conditions, thus two identical systems starting from slightly different points in the state space evolve, in long-term, in a totally uncorrelated manner. Therefore, synchronization of *real chaotic systems* is a relevant problem, being the initial conditions not exactly known in experimental setups. Many schemes for achieving synchronization of coupled chaotic units are discussed in literature, in particular are relevant the seminal paper by Pecora and Carroll [45, 5]. Synchronization schemes are classified in two main classes: unidirectional or bidirectional coupling. In the former case, the global system is subdivided into two parts, a master, whose dynamics remains unchanged, and a slave, that will be forced to follow the master dynamics. In the latter case, both master and slave system are affected by the coupling effects toward a common behavior that is often different from their original dynamics. Furthermore, we distinguish four main classes of synchronized behavior. Complete (or identical) synchronization (CS) consists in a perfect matching of the two (or more) chaotic trajectories, in this sense the systems forget their initial conditions, though continue to evolve chaotically; phase synchronization (PS) occurs in oscillators when their phases are locked, while amplitudes remain almost uncorrelated; lag synchronization (LS) is somehow between PS and CS [46] and occurs when the two trajectories are locked both in phase and amplitude but with a finite time lag; finally, generalized synchronization (GS) is achieved when the dynamics of one of the coupled systems can be

expressed as a function of the other dynamics. Transitions through the four synchronizations have been observed with respect to the strength of the coupling [46].

A case of particular interest is when we deal with *experimental nonlinear time series* and we would estimate the parameters of a known model to investigate if the asymptotic time evolution of at least a state variable of the nonlinear model can be synchronized with the experimental data from the physical process [6]. If we consider *master-slave synchronization* first introduced by Pecora and Carroll [45], we can assert that the master synchronizes with the slave if for all the choices of initial states the following limits hold (5.2):

$$\begin{aligned} \lim_{t \rightarrow \infty} |x(t) - \tilde{x}(t)| &= 0 \\ \lim_{t \rightarrow \infty} |y(t) - \tilde{y}(t)| &= 0 \\ \lim_{t \rightarrow \infty} |z(t) - \tilde{z}(t)| &= 0 \end{aligned} \tag{5.2}$$

where x, y, z and $\tilde{x}, \tilde{y}, \tilde{z}$ are the solutions of respectively the slave and the master system considered as a third order system. In the case here considered the master system is the experimental time series (a single state variable) and the slave system is the Chua's system. The system that has to be synchronized (slave system) can be decomposed at least into two subsystems: a drive system and a stable response sub-system (*method of decomposition into sub-systems*) such that we can force the slave system with the desired state variable (driven variable). It has been demonstrated that the systems synchronize also in presence of noise [5]. The synchronization setup used in this work is shown in

Fig. 5.8. The Chua's system has been decomposed into two subsystems corresponding to the state variable y and the state variables (x,z) .

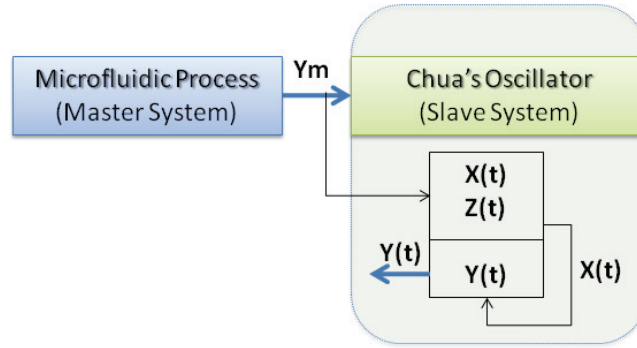


Fig. 5.8. Synchronization setup.

5.3.2 Parameters estimation via genetic algorithm

Once we have chosen the synchronization method it is fundamental to select an appropriate optimization method to select the best Chua's parameters so that the time series of the microfluidic process will be $y_m \approx y$. In order to achieve this an optimization index, used as fitness function, that takes into account the error between the y state variable of the Chua's oscillator and the time series y_m of the microfluidic process has been adopted:

$$I(\alpha, \beta, \gamma) = \sqrt{\sum_{k=0}^N (y_m - y(\alpha, \beta, \gamma))^2}. \quad (5.3)$$

The optimization method here presented is based on genetic algorithms (GA) in a standard form [24]. GA are an efficient and versatile instrumentation for global optimization of a function and furthermore

Table 5.1. Parameters of the Genetic Algorithm.

Number of individuals per subpopulations	Maximum number of generations	Generation gap	Precision of binary representation
20	20	0.9	20

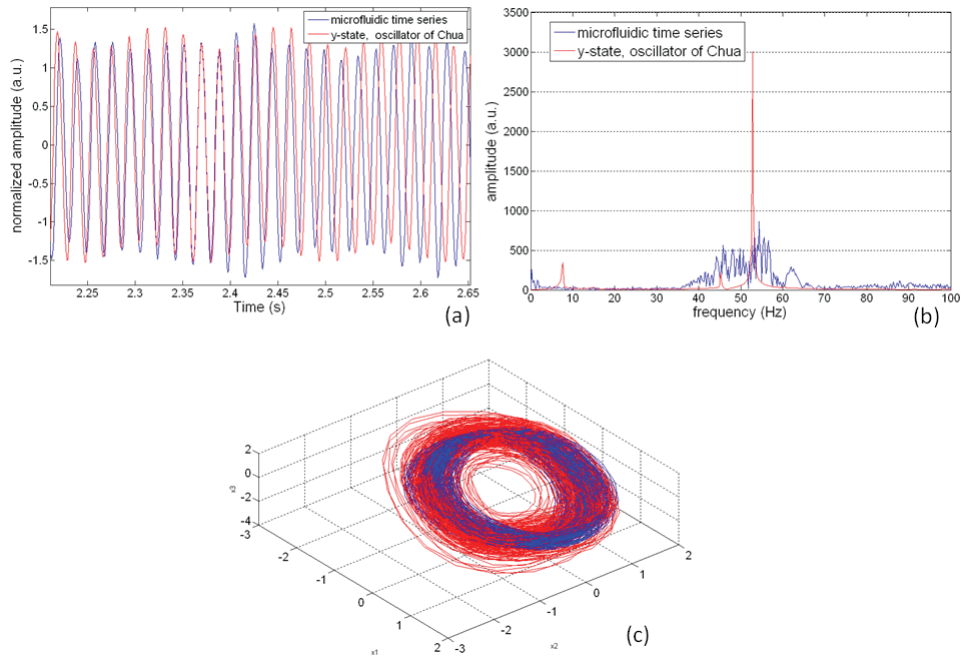


Fig. 5.9. (a) Time signals (b) Fourier spectra and (c) phase space reconstruction, of microfluidic time series for $V_{air}=1.2$ ml/min, $V_{water}=3.3$ ml/min (red line), and y-state variable of the Chua's oscillator (blue line).

are applicable in different engineering fields [24]. The easy implementation and power of genetic algorithms make them capable of optimizing also not convex functions. The peculiarities of a genetic algorithm are parallel processing of a population, that belongs to the function domain, such that the best characteristic information of each member of the population are transmitted and recombined with the others.

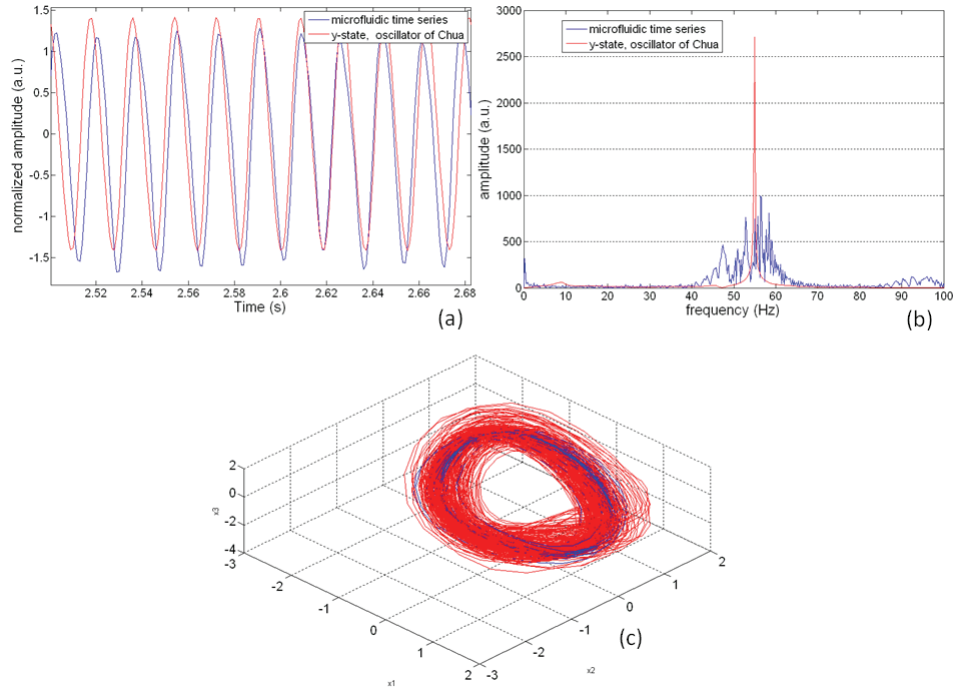


Fig. 5.10. (a) Time signals (b) Fourier spectra and (c) phase space reconstruction, of microfluidic time series for $V_{air} = 1.2$ ml/min, $V_{water} = 3.96$ ml/min (red line), and y -state variable of the Chua's oscillator (blue line).

The time series of the microfluidic process are used as master driving signal for the synchronization with a Chua's oscillator using the sub-system technique explained before. In particular the parameters m_0 m_1 are fixed and α , β and γ are set respectively in the range (1700,2000), (9000,11500), (0,1). Also the time step t_s was varied in the range (0.001,0.007). The response sub-system is simulated by using a Dormand-Prince method [15] with fixed time step. The parameters of the genetic algorithm for the optimization procedure are shown in Table 5.1.

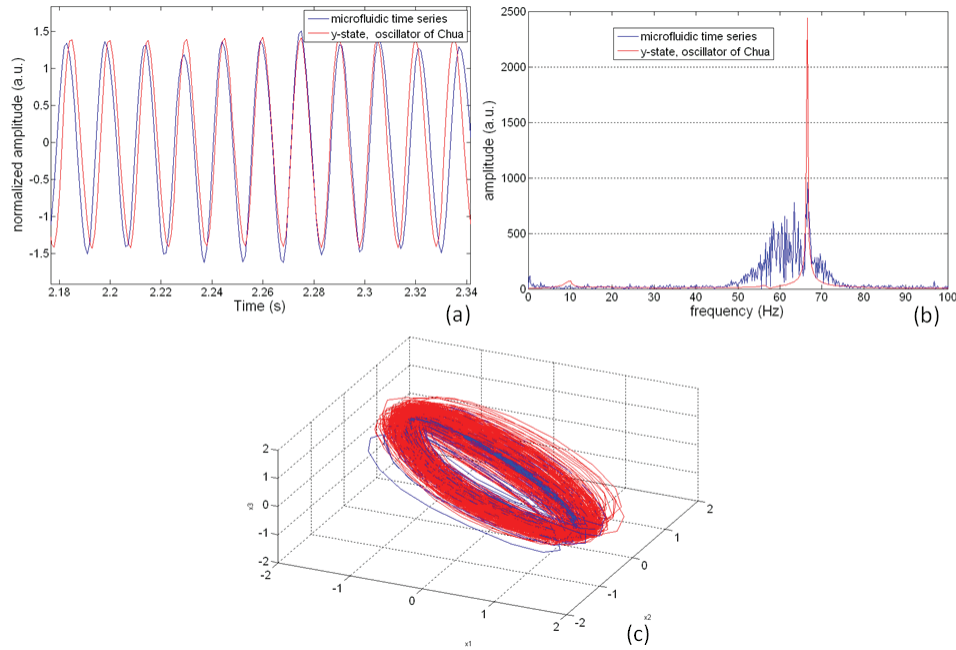


Fig. 5.11. (a) Time signals (b) Fourier spectra and (c) phase space reconstruction, of microfluidic time series for $V_{air}= 1.2$ ml/min, $V_{water}= 4.87$ ml/min (red line), and y-state variable of the Chua's oscillator (blue line).

5.4 Results

In this section some results for 4 selected time series of the optimization procedure for the identification of the microfluidic process are shown. It is worth to notice that complete synchronization is not achieved for all the microfluidic experiments. We encounter an alternation of phase synchronization (PS) and lag synchronization (LS). Thus we compared the time series, the Fourier spectra and the reconstructed attractors to show the effects of both synchronization and parameters estimation. Looking on Fig. 5.9(a) relative to the experiment $V_{air}= 1.2$ ml/min and $V_{water}= 3.3$ ml/min the time signals show consistence and LS is

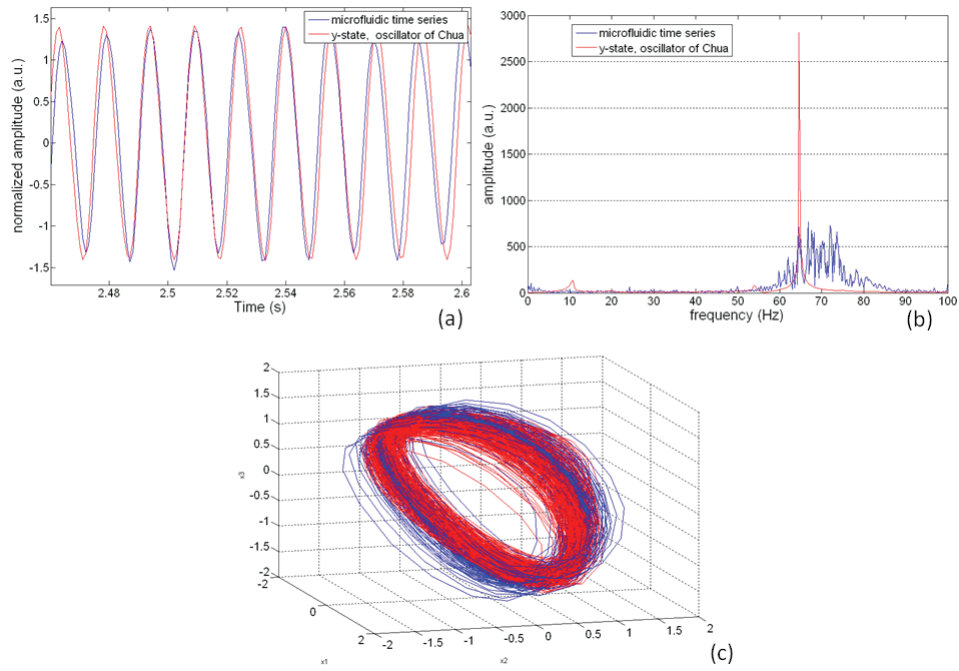


Fig. 5.12. (a) Time signals (b) Fourier spectra and (c) phase space reconstruction, of microfluidic time series for $V_{air}=1.2$ ml/min, $V_{water}=5.39$ ml/min (red line), and y-state variable of the Chua's oscillator (blue line).

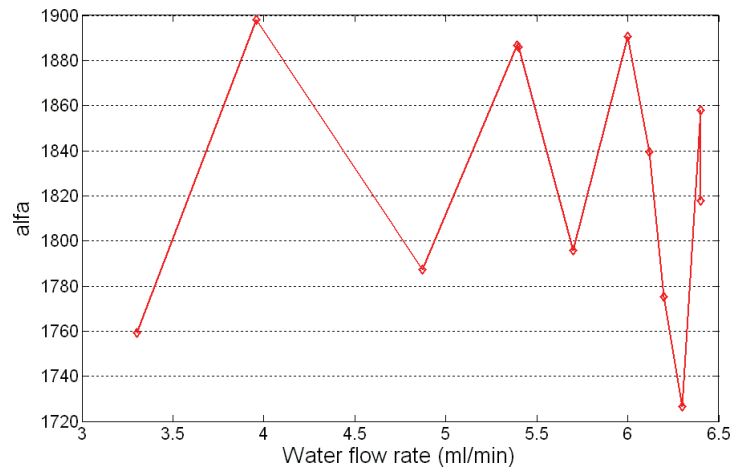


Fig. 5.13. α versus water flow rate.

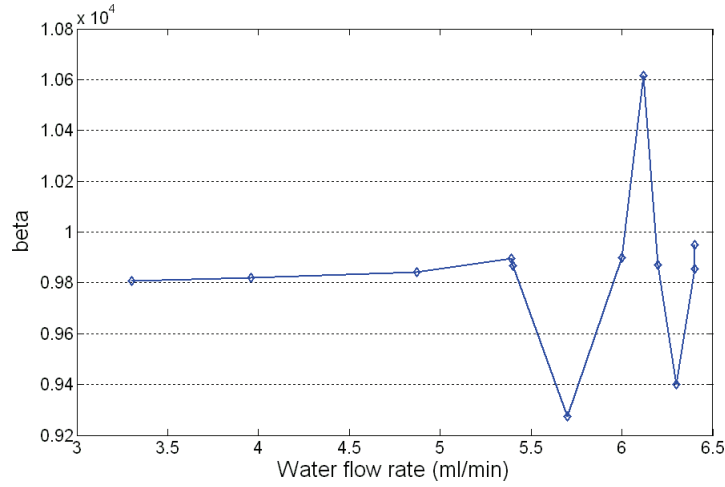


Fig. 5.14. β versus water flow rate.

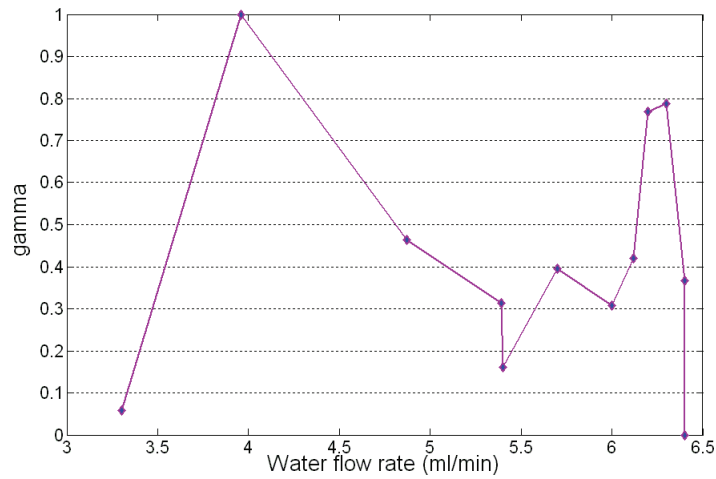


Fig. 5.15. γ versus water flow rate.

achieved. The Fourier spectrum of the Chua's system (see Fig. 5.9(b)) captures the main component of the experimental time series. This considerations are evident in phase space reconstruction in Fig. 5.9(c). The two attractors are not perfectly matched both in amplitude and phase. The same considerations can be done for the other time series: $V_{air} =$

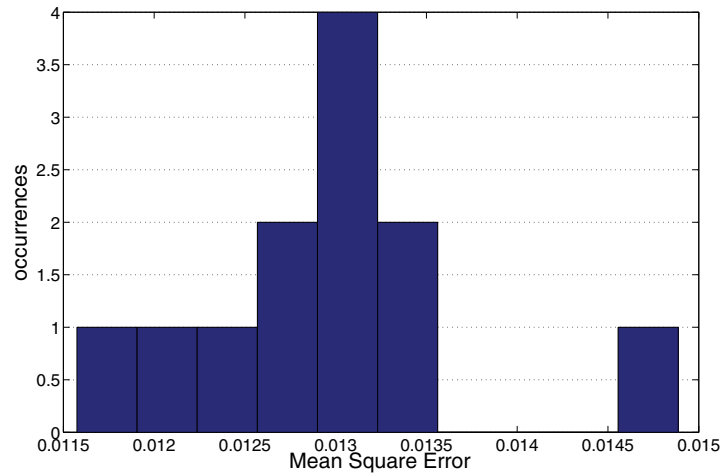


Fig. 5.16. Histogram of the mean square error between microfluidic time series and the y state variable used as fitness function.

1.2 ml/min and $V_{water} = 3.96$ ml/min in Fig. 5.10, $V_{air} = 1.2$ ml/min and $V_{water} = 4.87$ ml/min in Fig. 5.11, $V_{air} = 1.2$ ml/min and $V_{water} = 5.39$ ml/min in Fig. 5.12. A global view of the variability of the obtained parameters after the optimization procedure in relation to water flow rate changes is visible in Fig. 5.13 for α parameter in Fig. 5.14 for β and finally in Fig. 5.15 for γ parameter. In it worth to notice that the α parameter is more sensible than to the other parameters to water flow rate changes and so in the resulting *bubble flow* variations. Considering the mean square error for each time series the histogram in Fig. 5.16 is a good representation of the Gaussian errors' distribution. An error of the order of 10^{-2} is achieved for all the experiments.

5.5 Conclusions

In this work a new methodology for state identification of nonlinear experimental time series belonging to a microfluidic two-phase flow process has been presented. It is based on master-slave synchronization for chaotic system. The parameters of the Chua's model are estimated by the minimization of a suitable index by means of standard genetic algorithm procedure. The strength of this approach is that unknown nonlinear experimental phenomena could be identified using the presented procedure. On the contrary the limit remains model selection.

Concluding remarks

Since its emergence in the 1990s, microfluidics has become a powerful technique for a wide variety of applications in biotechnology, engineering, physics, and chemistry. By studying processes in channels with typical dimensions of tens to hundreds of micrometers, researchers can conduct controlled reactions while economizing on the consumption of possibly scarce materials. This PhD thesis deals with experimental studies for the control of two-phase microfluidic flows. Two-phase flows in microfluidics open new ways for the development of portable Lab on a Chip systems. Easy mixing, fast reaction time, cell encapsulation, no sample dispersion are some of the numerous advantages concerning two-phase flow systems.

A microfluidic system can be thought as a dynamical system with input, output and state variables. In particular, our attention focused on the development of experimental techniques and data analysis for two-phase flow identification. Data acquisition is not simple in microfluidics and big efforts have been done in the past to visualize and characterize the bubbles/droplets shape, flow patterns, etc. Thus in the context of

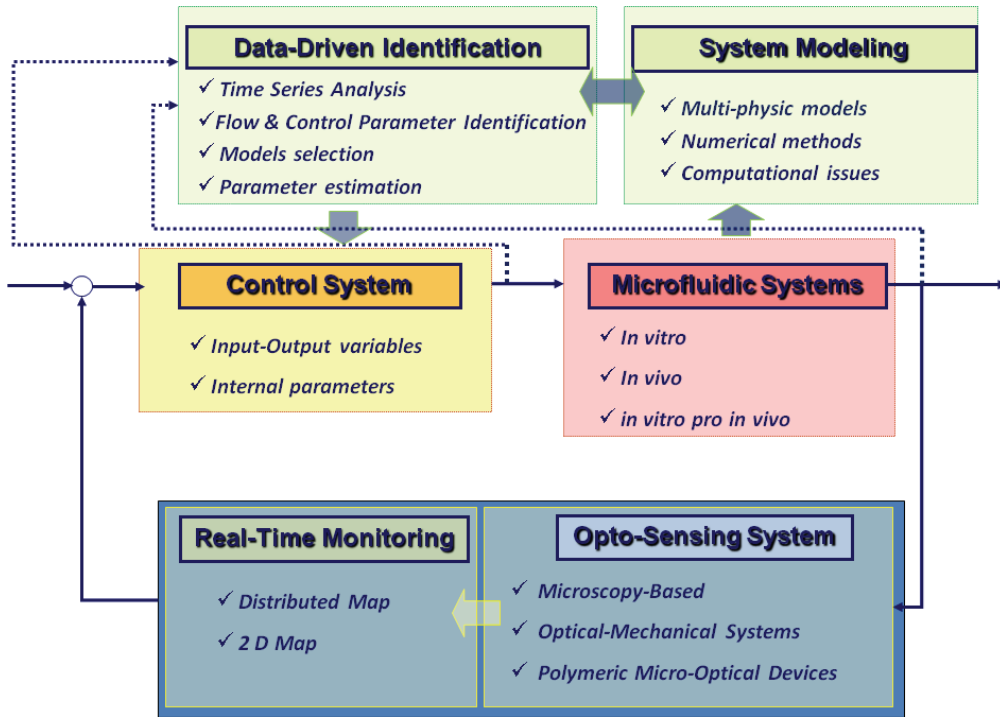


Fig. 6.1. Block diagram of the thesis' subjects.

monitoring systems has been presented the design of innovative polymeric micro-optical systems. They allows the reduction of bulky experimental apparatus toward on-chip and real-time monitoring systems. All the experimental analysis have been based on time series of optical information of the process under study. Moreover nonlinear time series analysis is exploited for the extraction of important parameters (divergence analysis, Lyapunov exponents) for the quantification and identification of the two-phase flow dynamics. The identified relation maps have allowed a back-box identification of the system (input flow rate, dynamics of two-phase flow). Synchronization has been also ex-

exploited for the identification of a nonlinear mathematical model in the perspective of control system implementation. It is worth to notice that the proposed framework is extensible to several microfluidic flows. The produced research can be summarized in the feedback control schema shown in Fig. 6.1.

Acknowledgements

“Semper ad maiora!”

My main Thanks go to my Family. Their invaluable Support and Love give me the strength to go ahead.

Thanks to Filippo, my Love, for being always beside me also in distances.

I Thank all the colleagues, great minds met for very short period, that allow me to believe in good Research. They taught me that Friendship can start immediately.

Last but not least, Thanks to my supervisors prof. Luigi Fortuna and prof. Maide Bucolo for the possibilities that they offered me.

References

1. E. Aurell, G. Boffetta, A. Crisanti, G. Paladin, A. Vulpiani, Predictability in the large: an extension of the concept of Lyapunov exponent, *J. Phys. A.*, 30, pp. 1-26 (1997)
2. V. Barbier, H. Willaime, P. Tabeling, Producing droplets in parallel microfluidic systems, *Phys. Rev. Lett. E.*, 74, pp. 046306-1-046306-4 (2006)
3. R. Barry, D. Ivanov, Microfluidics in biotechnology, *Journal of Nanobiotechnology*, 2:2, pp. 1-5 (2004)
4. R. Daw and J. Finkelstein, Insight: Lab on a chip, *Nature*, 442(7101), pp. 367-418 (2006)
5. S. Boccaletti, J. Kurths, G. Osipov, D. L. Vallardes, C. S. Zhou, *The synchronization of chaotic systems*, *Phys. Rev.*, 366, pp. 1-101 (2002)
6. N. Boccara, *Modeling Complex Systems*, Springer-Verlag, New York (2004)
7. A. Bonasera, M. Bucolo, L. Fortuna, M. Frasca, A. Rizzo, The d_∞ parameter to characterise chaotic dynamics. *Non linear Phenomena in Complex Systems*, 6, pp. 565-570 (2003)
8. M.R. Bringer, C.J. Gerdt, H. Song, J.D. Tice, R.F. Ismagilov, Microfluidic systems for chemical kinetics that rely on chaotic mixing in droplets, *Philos. T. Roy. Soc. A.* 362, pp. 1087-1104 (2004)
9. H. Bruus, *Theoretical Microfluidics*, Oxford Master Seies in Condensed Matter Physics, Oxford University Press (2008)
10. M. Bucolo, V.J. Cadarso, L. Esteve, A. Llobera, F. Sapuppo and F. Schembri, Disposable micro-electro-optical interface for flow monitoring in bio-microfluidics, *Proceed-*

- ings of the 12th Conference on Miniaturized Systems of Chemistry and Life Science microTAS08, pp. 1579-1581 (2008)
11. S. Camou, H. Fujita and T. Fujii, PDMS 2D optical lens integrated with microfluidic channels: principle and characterization, *Lab Chip*, 3:40-45 (2003)
 12. D.A. Chang-Yen, R.K. Eich and B.K. Gale, A monolithic PDMS waveguide system fabricated using soft-lithography techniques, *Journal of Lightwave Technology*, 23, pp. 2088-2093 (2005)
 13. V. Cristini and Y. Yung-Chieh, Theory and numerical simulation of droplet dynamics in complex flows-a review, *Lab on a Chip*, 4, pp. 257-264 (2004)
 14. T. Cubaud, C.M. Ho, Transport of bubbles in square microchannels, *Physics of Fluids*, 16, pp. 4575-485 (2004)
 15. J. R. Dormand, P. J. Prince, A family of embedded Runge-Kutta formulae, *Journal of Computational and Applied Mathematics*, 6, pp. 1926 (1980)
 16. R. Dreyfus, P. Tabeling, H. Willaime, Ordered and disordered patterns in two-phase flows in microchannels, *Phys. Rev. Lett.*, 90, pp. 144505-1-144505-4 (2003)
 17. J. Dbendorfer and R.E. Kunz, Reference pads for miniature integrated optical sensors, *Sensors and Actuators B Chemical*, 38, pp. 116-121 (1997)
 18. D.C. Duffy, J. Cooper McDonald, O.J.A. Schueller, and G.M. Whitesides, Rapid prototyping of microfluidic systems in poly (dimethylsiloxane), *Anal. Chem.*, 70, pp. 4974-4984 (1998)
 19. Eggers, Nonlinear dynamics and breakup of free-surface flows, *Rev. Mod. Phys.*, 69, pp. 865-929 (1997)
 20. Fluent 6.3.26 Documentation.
 21. A.M. Ganan-Calvo, J.M. Gordillo, Perfectly monodisperse microbubbling by capillary flow focusing, *Phys.Rev.Lett.*, 87, pp. 274501-274504 (2001)
 22. P. Garstecki et al., Formation of monodisperse bubbles in a microfluidic flow-focusing device. *Appl.Phys.Lett.*, 85, pp. 2649-2651 (2004)
 23. P. Garstecki, J. Fuerstman, M. Fischbach, S.K. Sia, G.M. Whitesides, Mixing with bubbles: a practical technology for use with portable microfluidic devices, *Lab on a Chip*, 6, pp. 207-212 (2006)
 24. D.E. Golbert, *Genetic Algorithms in Search, Optimization and Machine Learning*, Addison Wesley, (1989)

25. H. Golster, M. Linden, S. Bertuglia, A. Colantuoni, G Nilsson, and F. Sjoberg, Red blood cell velocity and volumetric flow assessment by enhanced high-resolution laser Doppler imaging in separate vessels of the hamster cheek pouch microcirculation, *Microvasc Res*, 58, pp. 62-73 (1999)
26. GRID web site: <https://grid.ct.infn.it/twiki/bin/view/PI2S2/UserTutorials>.
27. A.D. Griffiths, D.S. Tawfik, Miniaturising the laboratory in emulsion droplets. *Trends in Biotechnology*, 24, pp. 395-402 (2006)
28. M. Hesler, Synchronization Principles and Applications, ISCAS'94 Tutorials, pp. 314-327 (1994)
29. M. Imai and S. Sato, Optical Switching Devices Using Nonlinear Fiber-Optic, Photonics Based on Wavelength Integration and Manipulation Grating Coupler, IPAP Books 2, pp. 293-302 (2005)
30. Z. Jiao, N.-T. Nguyen, X. Huang, Chaotic motion of microplugs under high-frequency thermocapillary actuation. *J. Micromech. Microeng.*, 7, pp. 184-185 (2007)
31. M. Joanicot, A. Ajdari, Droplet control for microfluidics, *Applied Physics*, 309, pp. 887-888 (2005)
32. H. Kantz, T. Schreiber, *Nonlinear Time Series Analysis*, Cambridge University Press, Cambridge (2004)
33. K. B. Mogensen, Y. C. Kwok, J. C. T. Eijkel, N. J. Petersen, A. Manz, and J. P. Kutter, A Microfluidic Device with an Integrated Waveguide Beam Splitter for Velocity Measurements of Flowing Particles by Fourier Transformation, *Anal. Chem.*, 75(18), pp 4931-4936 (2003)
34. B. Kuswandi, Nuriman, J. Huskens, W. Verboom, Optical sensing systems for microfluidic devices: A review, *Analytica Chimica Acta*, 601, pp. 141-155 (2007)
35. L. D. Landau and E. M. Lifshitz, *Fluid Mechanics 2nd edition Course in Theoretical Physics*, Institute of Physical Problems, USSR Academy of Sciences, Butterworth-Heinemann, (2000)
36. M. Linden, H. Golster, S. Bertuglia, A. Colantuoni, F. Sjoberg, and G. Nilsson, Evaluation of enhanced high-resolution laser Doppler imaging in an in vitro tube model with the aim of assessing blood flow in separate microvessels, *Microvasc Res*, 56, pp. 261-70 (1998)
37. A. Llobera, S. Demming, R. Wilke, and S. Buttgenbach, Multiple internal reflection poly(dimethylsiloxane) systems for optical sensing, *Lab Chip*, 7, pp. 1560-1566 (2007)

38. A. Llobera, R. Wilke, S. Buttgenbach, Enhancement of the response of poly(dimethylsiloxane) hollow prisms through air mirrors for absorbance-based sensing, *Talanta*, 75, pp. 473-479 (2007)
39. R. N. Madan, *Chua's Citcuit: A Paradigm for Chaos*, World Scientific pub., vol. 1, Series B, Singapore (1993)
40. Mao, X., Juluri, B.K., Lapsley, M.I., Stratton, Z.S., Huang, T.J., Milliseconds microfluidic chaotic bubble mixer, *Microfluid Nanofluid*, 8, pp. 139-144 (2010)
41. M.D. Menger, M.W. Laschke, B. Vollmar, Viewing the microcirculation through the window: some twenty years experience with the hamster dorsal skinfold chamber, *Eur Surg Res*, 34, n.1-2, pp. 83-91 (2002)
42. K.B. Mogensen, Y.C. Kwork, J.C.T. Eijkel, N.J. Petersen, A. Manz, J.P. Kutter, A microfluidic device with an integrated waveguide beam splitter for velocity measurements of flowing particles by Fourier transformation, *Analytical Chemistry*, 75, pp. 4931-4936 (2003)
43. N.-T. Nguyen, S. Wereley, *Fundamentals and applications of microfluidics*, (ed.) Integrated Microsystems Series, Artech House (2002)
44. N.-T. Nguyen et al. Optical detection for droplet size control in microfluidic droplet-based analysis systems, *Sensors and Actuators B*, 117, pp. 431-436 (2006)
45. L. M. Pecora, T. L. Carroll, Synchronization in chaotic systems, *Phys. Rev. Lett.*, 64:8, pp. 821-824 (1990)
46. M. G. Rosenblum, A. S. Pikovsky, J. Kurths, From Phase to Lag Synchronization in Coupled Chaotic Oscillators, *Phys. Rev. Lett.*, 78:22, pp. 4193-4196 (1997)
47. F. Sapuppo, M. Bucolo, M. Intaglietta, L. Fortuna and P. Arena, Cellular Nonlinear Network: Real-Time Technology for the Analysis of Microfluidic Phenomena in Blood Vessels, *Nanotechnology*, IOP No.17, pp. S54-S63 (2006)
48. F. Sapuppo, M. Bucolo, M. Intaglietta, P. C. Johnson, L. Fortuna and P. Arena, An Improved Instrument for Real-Time Measurement of Blood Velocity in Microvessels, *Instrumentation and Measurement*, IEEE Transactions on, 56:6, pp. 2663- 2671 (2007)
49. F. Sapuppo, F. Schembri, L. Fortuna, M. Bucolo, Microfluidic circuits and systems, *Circuits and System Magazine IEEE*, 9, pp. 6-19 (2009)

50. F. Sapuppo, A. Llobera, F. Schembri, M. Intaglietta, V.J. Cadarso and M. Bucolo, A polymeric micro-optical interface for flow monitoring in biomicrofluidics, *Biomicrofluidics*, pp. 4:024108-1,024108-13 (2010)
51. F. Sapuppo, A. Llobera, F. Schembri and M. Bucolo, a Polymeric micro-optic device for the detection of microfluidic flow spatial profile, *Proceedings of the 14th Conference on Miniaturized Systems of Chemistry and Life Science microTAS10* (2010)
52. F. Sarrazin, L. Prat, N. Di Miceli, G. Cristobal, D.R. Link, D.A. Weitz, Mixing characterization inside microdroplets engineered on a microcoalescer, *Chemical Engineering Science*, 62, pp. 1042-1048 (2007)
53. F. Schembri, F. Sapuppo, M. Bucolo, Experimental Identification of Nonlinear Dynamics in Microfluidic Bubbles' Flow, (submitted to) *Nonlinear Dynamics*, Springer.
54. A. Serizawa, Z. Feng, Z. Kawara, Two-phase flow in microchannels, *Experimental Thermal and Fluid Science*, 26, pp. 703-714 (2002)
55. A. W. Snyder, J. D. Love, *Optical Waveguide Theory*, Chapman and Hall ISBN 0-412-09950-0, (1983)
56. J.C. Sprott, S. Wereley, *Chaos and Time-Series Analysis*, Oxford University Press, Oxford (2003)
57. Y. Sugii, S. Nishio, and K. Okamoto, In vivo PIV measurement of red blood cell velocity field in microvessels considering mesentery motion, *Physiol. Meas.*, 23, pp. 403-416 (2002)
58. Y.C. Tan, J.S. Fisher, A.I. Lee, V. Cristini, A.P. Lee, Design of microfluidic channel geometries for the control of droplet volume, chemical concentration, and sorting, *Lab Chip.*, 4, pp. 292-298 (2004)
59. T. Thorsen, R.W. Roberts, F.H. Arnold, S.R. Quake, Dynamic pattern formation in a vesicle-generating microfluidic device, *Phys.Rev.Lett.*, 86, pp. 4163-4166 (2001)
60. J.D. Tice, H. Song, A.D. Lyon, R.F. Ismagilov, Formation of droplets and mixing in multiphase microfluidics at low values of the reynolds and capillary numbers, *Langmuir*, 19, pp. 9127-9133 (2003)
61. J.M.T. Thompson, H.B Stewart, *Nonlinear Dynamics and Chaos*, John Wiley and Sons (1989)
62. M. Ursino, A. Colantuoni, and S. Bertuglia, *Microvasc. Res.*, 56:3, pp. 233 (1998)
63. H. Wayland, and P.C. Johnson, Erythrocyte velocity measurement in microvessels by a two-slit photometric method, *J. Appl. Physiol*, 22:2,, pp. 333-337 (1967)

64. G.M. Whitesides, The origins and the future of microfluidics, *Nature*, 442, pp. 368-373 (2006)
65. H. Willaime, V. Barbier, L. Kloul, P. Tabeling, Arnold tongues in microfluidic drop emitter, *Phys. Rev. Lett.*, 96, pp. 054501-1-054501-4 (2006)
66. S.Q. Xu et al., Generation of monodisperse particles by using microfluidics: control over size, shape, and composition, *Angew. Chem. Int. Ed.*, 44, pp. 724-728 (2005)

List of Figures

1.1	(a) Solution domain. (b) The superficial and volumetric mesh used in the model.	12
1.2	Coutour of air fraction in the two-phase flow simulation.	15
2.1	Schematic three-dimensional view of waveguide and propagation of light at different angles.	22
2.2	Two dimensional representation of light propagating from a source with a specific numerical aperture through a lens.	24

- 3.1 (a) Section of the device (with $L=2.5$ mm, $W=1$ mm and with thickness $T=120$ μm . S is the slit 70 μm . M is the 40° mirror; WG is the TIR optical waveguides (100 μm width). FL is the biconvex focusing lens (160 μm radius of curvature). F1 is the fiber optic insertion and self-alignment system (125 μm diameter). F2 is the fiber optic positioned in front of the slit. P is the pillar mirror. O is the output surface. I is the input surface. [(b) and (c)] Variations in the slit design with slit orientation angle at 40° . (b) $S=25$ μm and (c) $S=50$ μm . (d) Variation in the orientation of the FL according to the angle of the rays coming from the waveguide. 35
- 3.2 Micro-optic interface functional configurations. (a) 3D view of the device and of the direction of the optical information. (b) OW configuration. (c) IW configuration. 36
- 3.3 SEM images of the SU8 master with $120\mu\text{m}$ thickness and slit $S=70$ μm . (a) Picture of the entire functional geometry. (b) Details of the slit ($S=70$ μm) and of the mirror (M). (c) Details on the focusing lens (FL). 37
- 3.4 Static optical characterization for PDMS device in OW configuration ($S=70$ μm and thickness $T=120$ μm). (a) Ray tracing simulation of the light path. (b) Picture of the light path on the PDMS device. 41

3.5	Static optical characterization for PDMS device in IW configuration ($S=70 \mu\text{m}$ and thickness $T=120 \mu\text{m}$) Ray tracing simulation of the light path (only rays with a power of at least 70% of the source power).(b) Picture of the light path on the PDMS device.	42
3.6	Color-coded light spatial profile on surface I (Fig. 3.1(a)) for IW configuration. (a) Light profile found by ray tracing simulation.(b) Experimental light profile collected by a 10x objective and a CCD camera.	43
3.7	Ray tracing simulation for OW configuration with slit sizes (a) $S=25 \mu\text{m}$ and (b) $S=50 \mu\text{m}$ with tilted slit, and (c) $S=70 \mu\text{m}$ with straight slit.	43
3.8	Losses (dB) versus slit size: experimental and simulated.	44
3.9	Experimental setup for dynamic characterization of two-phase flow in a microfluidic device. Photographs of details in (a) upper view of the two-phase ethanol/air flow in the microfluidic device; (b) the micro-optic interface in the OW configuration positioned on the microfluidic mixer.	48
3.10	Light power dynamic response due to the bubble flow measured by the power meter.	49
3.11	In vivo flow monitoring system.	50
3.12	In vivo flow monitoring system photograph. Micro-optical interface on live hamster tissue for the acquisition of photometric signals.	50

3.13	Microcirculation fields under the polymeric device with digital $70 \times 70 \mu m^2$ slit. (a) Entire frame and region of interest (red square). (b) Frame sequence related to the region of interest at intervals of 200 ms.	51
3.14	Comparison between the normalized optical signals resulting from photodiodes acquisition and the digital slit obtained from image sequence analysis.....	51
3.15	Spectral components of the photodiode signal and of the time series extracted from the image sequence.	52
3.16	Input micro-optical device. The top figure shows four insertions for the input optical fibers, the collimating lenses ($CL_{1,2,3,4}$), the PDMS waveguides ($WG_{1,2,3,4}$), the air mirrors of length $97 \mu m$ ($M_{1,2,3,4}$) and the output slits ($S_{1,2,3,4}$). The slit size is $70 \mu m$. The bottom inset on the left depict the SEM check of the input device in the master while on the right the SEM indicates the particular structure of both mirrors and waveguides. ...	53

- 3.17 Output micro-optical device. This device merges four light paths coming from ($S_{1,2,3,4}$) in a unique beam by means of two stage merging (4x2 and 2x1). A block including two straight mirrors of length $275 \times 50 \mu\text{m}$ $M_{1,2}$ and a mirror prism MP ($250 \times 200 \mu\text{m}$) is needed to combine two light path in one. The light is then focused by a focusing lens (FL) toward the output optical fiber. The pillar mirrors with diameter of $100 \mu\text{m}$ (P) are used to protect the device from the out coming light. The SEM picture at the bottom depicts the structure of the device in the master. 54
- 3.18 Ray-tracing of the complete optical setup: four light beams of different wavelength are focused and redirected toward the microfluidic channel. The transparency of the microfluidic channel allows the rays to pass through the device. The out coming light is then collected and merged toward the output optical fiber. 55
- 3.19 Out coming light attenuation for each slit. The losses are calculated from experimentation and simulation by measuring the power of the light at the output fiber. The mismatching between the slits indicates a slight misalignment of the output fiber. It is also indicated by means of simulations the losses in case of perfect insertion of the output fiber. 58

3.20	Experimental setup for optical detection system in the microfluidic two-phase flow system.	59
3.21	(a) Particular of the experimental setup. The selected areas of the microfluidic device are sandwiched between the input and output optical device. (b) Slits' locations in the microchannel.	59
3.22	Typical output spectrum representing four peaks at different wavelengths. Each wavelength is representative of a slit's position in the microchannel: $slit_1$ - 405 nm, $slit_2$ - 470 nm, $slit_3$ - 525 nm, $slit_4$ - 639 nm.	60
3.23	Results of a two-phase flow experiment for constant input flow: air 5 $\mu\text{l/s}$ and ethanol 24 $\mu\text{l/s}$. The reference signals represent ethanol flowing at 24 $\mu\text{l/s}$	61
3.24	Signals related to bubbles' passage at two different velocities. The signals are recorded for the $slit_1$ associated to λ_1	62
3.25	Fitting of the maximum peaks in the data flow acquisition in S_1 for (a) sinusoidal, (b) square, and (c) saw-tooth air flow rate (ethanol flow rate is maintained fixed at 4 $\mu\text{l/s}$). The bubble flows for sinusoidal and square input are both fitted with a sinusoidal function, while the bubble flow for saw tooth generate a flow that can be fitted with two Gaussian functions.	63

3.26	Number of bubbles that flow in slit S_1 each 1 s for: (a) sinusoidal, (b) square, and (c) saw-tooth air flow rate. Number of bubbles that flow in S_1 each 2 s for: (a) sinusoidal, (b) square, and (c) saw-tooth air flow rate. The ethanol flow rate is maintained fixed at $4 \mu\text{l/s}$	64
3.27	Splitter based on TIR condition. (a) Design. The blue part indicates air while white PDMS. (b) SEM picture of the SU8 master.	71
3.28	Splitter based on partial refraction condition. (a) Design. The blue part indicates air while white PDMS. (b) Details on the prism P1 and functional principles. (c) SEM pictures of the master: upper part (on the right) including input system, lens CLin, prism P1, mirror M2, lens CL2 and CL3 and bottom part (on the left) including: mirror M1, and the lenses (CL1, CL2, FL2, CL3, FL3) to adjust the beams to the desiderate dimension and localization.	72
3.29	Experimental setup.	74
3.30	TIR-based splitter.(a) Ray tracing simulation and (b) experimental spectral responses of each output.	74
3.31	Spatial visualization of the splitted beam from the right to the left side O4-3-2-1: (a) Simulated and (b) experimental.	75
3.32	Partial refraction-based splitter. Ray tracing simulation.	75

3.33	Normalized experimental visualization of the spatial splitted beam for outlet O3, O2 and O1.	76
3.34	Normalized spatial visualization of the simulated splitted beam for outlet O3, O2 and O1.	76
4.1	(a) The microfluidic snake channel and the bubble flow pattern generation in the designed area. (b)-(c) Time series and (d)-(e) frequency spectra representative of bubbles passage respectively for $V_{air}=0.12$ ml/min, $V_{water}=0.63$ ml/min and for $V_{air}=1.2$ ml/min, $V_{water}=6.3$ ml/min.	83
4.2	Time signals related to two-phase flow dynamics ($V_{air}=1.2$ ml/min, $V_{water}=2.26$ ml/min) and water flow ($V_{water}=2.26$ ml/min).	83
4.3	Block representation of the experimental set-up: two syringe pumps are connected to the microfluidic channel inlets, the electro-optic system and the photodiode based circuit. A DAQ converts the light variation signals with a sample rate of 1 kHz to time series.	84
4.4	Reconstruction in the Air Flow Rate - Water Flow Rate space of the four experimental campaigns for constant input flow: Campaign-1 (V_{water} fixed) and Campaign-2 (V_{air} fixed) with flow rates smaller than 1 ml/min; Campaign-3 (V_{water} fixed) and Campaign-4 (V_{air} fixed) with flow rates bigger than 1 ml/min.	86

4.5	(a) The microfluidic snake channel and the bubble flow pattern generation in the designed area. (b) Block diagram of the experimental setup. Natural frequencies of the two phase flow versus (c) air flow rate and (d) water flow rate.	87
4.6	Time signal of the two-phase flow for $f_{water}=f_{air}= 5$ Hz (colored in red) and water flow (blue signal).	88
4.7	Experimental Campaigns. In Campaign-1 $f_{water}=5$ Hz is fixed while f_{air} is varied; in Campaign-2 $f_{air}=5$ Hz is fixed and f_{water} is varied. (a) Typical Fourier power spectrum of the bubble flow and (c) time series dynamics for $f_{air}=5$ Hz and $V_{air}=1.2$ ml/min (Campaign-1).(b) Typical Fourier power spectrum and (d) time series dynamics for $f_{water}=7$ Hz and $V_{water}=2.26$ ml/min (Campaign-2).....	89
4.8	Dynamics of the LE and d_{∞} versus the varying water flow rate (air flow rate is fixed). (a) d-infinite versus water flow rate ($V_{water} \geq 1$ ml/min, Campaign 4), (b) d-infinite versus water flow rate ($V_{water} \leq 1$ ml/min, Campaign 2), (c) Largest Lyapunov Exponent versus water flow rate ($V_{water} \geq 1$ ml/min, Campaign 4), (d) Largest Lyapunov Exponent versus water flow rate ($V_{water} \leq 1$ ml/min, Campaign 2).	91

- 4.9 Dynamics of the LE and d_∞ versus the varying air flow rate (water flow rate is fixed). (a) d_∞ versus air flow rate ($V_{air} \geq 1$ ml/min, Campaign 3), (b) d_∞ versus air flow rate ($V_{air} \leq 1$ ml/min, Campaign 1), (c) Largest Lyapunov Exponent versus air flow rate ($V_{air} \geq 1$ ml/min, Campaign 3), (d) Largest Lyapunov Exponent versus air flow rate ($V_{air} \leq 1$ ml/min, Campaign 1). 92
- 4.10 (a) Largest Lyapunov exponent versus Ca. For $Ca \leq 0.003$ ($V \leq 1$) the dynamics of bubbles presents values in the range (0, 1) meanwhile for $Ca \geq 0.003$ ($V \geq 1$) the range is (2, 5). (b) d_∞ versus Ca. For $Ca \leq 0.003$ ($V \leq 1$) the dynamics of bubbles presents values in the range (0, 2) meanwhile for $Ca \geq 0.003$ ($V \geq 1$) the range is (3, 6). 95
- 4.11 Campaigns 2 and 4 have $AF \leq 0.4$ and Campaigns 1 and 3 have $AF \geq 0.4$. (a) Largest Lyapunov exponent versus AF. For ($V \leq 1$) the dynamics of bubbles presents values in the range (0, 1) meanwhile for $Ca \geq 0.003$ ($V \geq 1$) the range is (2, 5). (b) d_∞ versus Ca. For $Ca \leq 0.003$ ($V \leq 1$) the dynamics of bubbles presents values in the range (0, 2) meanwhile for $Ca \geq 0.003$ ($V \geq 1$) range is (3, 6). 96

- 4.12 Contour plot of (a) d-infinite versus Ca and AF. (b) LE versus Ca and AF. State space representation of eight selected experiments: $A_1(V_{air}=0.17$ ml/min, $V_{water}=0.15$ ml/min), $D_1(V_{air}=0.64$ ml/min, $V_{water}=0.15$ ml/min), $A_2(V_{air}=0.12$ ml/min, $V_{water}=0.15$ ml/min), $D_2(V_{air}=0.12$ ml/min, $V_{water}=0.61$ ml/min), $A_3(V_{air}=1.2$ ml/min, $V_{water}=1.57$ ml/min), $D_3(V_{air}=7.43$ ml/min, $V_{water}=1.57$ ml/min), $A_4(V_{air}=1.2$ ml/min, $V_{water}=2.26$ ml/min), $D_4(V_{air}=1.2$ ml/min, $V_{water}=6.4$ ml/min) 97
- 4.13 (a) Amplitude A_{max} versus the frequency of varying input flow and (b) normalized resonance frequency f_{max} versus the frequency of varying input flow.(c) Capillary number versus water flow frequency. The strong slope changes are in point A and B. 99
- 4.14 (a) Number of frequency components versus input frequency .(b) Frequency occurrences in spectra of output flow. The classification is related if the input periodic flows (air and water) are multiple or not-multiple100
- 4.15 (a) d-infinite versus flow rate frequency; (b) Largest Lyapunov exponent versus flow rate frequency. 101
- 4.16 (a) d-infinite versus AF; (b) Largest Lyapunov exponent versus AF..... 102

- 4.17 Phase diagrams for Campaign-1 (water flow fixed).
 (a) d-infinite versus air flow frequency and AF; (b)
 Largest Lyapunov exponent versus air flow frequency
 and AF. A_1, A_2, A_3, A_4, A_5 are related to the state
 space reconstruction reported below. 103
- 4.18 Phase diagrams for Campaign-2 (air flow rate fixed),
 (a) d-infinite versus water flow frequency and AF; (b)
 Largest Lyapunov exponent versus water flow frequency
 and AF. A_1, A_2, A_3 , are related to the state space
 reconstruction reported below. 104
- 5.1 The microfluidic snake channel and the bubble flow
 pattern generation in the designed area of $640 \mu\text{m} \times 935$
 μm . The section of the microfluidic channel is $S=640$
 μm while the internal radius of curvature is $R=1.28 \text{ mm}$. 109
- 5.2 Block representation of the experimental set-up: two
 syringe pumps are connected to the microfluidic channel
 inlets, the electro-optic system and the photodiode
 based circuit. A DAQ converts the light variation
 signals with a sample rate of 1 kHz to time series. 109
- 5.3 (a) Time signal related to two-phase flow dynamics
 for air flow rate $V_{air}= 1.2 \text{ ml/min}$ and water flow rate
 $V_{water}=3.96 \text{ ml/min}$ (red line). (b) Fourier spectrum of
 the signal. 110

5.4	Attractors of 6 microfluidic experiments:(a) $V_{air} = 1.2$ ml/min, $V_{water} = 3.3$ ml/min, (b) $V_{air} = 1.2$ ml/min, $V_{water} = 3.9$ ml/min, (c) $V_{air} = 1.2$ ml/min, $V_{water} = 5.3$ ml/min, (d) $V_{air} = 1.2$ ml/min, $V_{water} = 6$ ml/min, (e) $V_{air} = 1.2$ ml/min, $V_{water} = 6.4$ ml/min, (f) $V_{air} = 1.2$ ml/min, $V_{water} = 6.45$ ml/min.	111
5.5	Chua's attractor for $\alpha=1800$, $\beta=1000$, $\gamma=0$, $m_0=-1.026$, and $m_1=-0.982$	113
5.6	Chua's time series for $\alpha=1800$, $\beta=1000$, $\gamma=0$, $m_0=-1.026$, and $m_1=-0.982$. (a) x state variable, (b) y state variable, (c) z state variable.	113
5.7	Fourier spectra for (a) x state variable, (b) y state variable, (c) z state variable. The parameters of the systems are $\alpha=1800$, $\beta=1000$, $\gamma=0$, $m_0=-1.026$, and $m_1=-0.982$	114
5.8	Synchronization setup.	117
5.9	(a) Time signals (b) Fourier spectra and (c) phase space reconstruction, of microfluidic time series for $V_{air} = 1.2$ ml/min, $V_{water} = 3.3$ ml/min (red line), and y-state variable of the Chua's oscillator (blue line).	118
5.10	(a) Time signals (b) Fourier spectra and (c) phase space reconstruction, of microfluidic time series for $V_{air} = 1.2$ ml/min, $V_{water} = 3.96$ ml/min (red line), and y-state variable of the Chua's oscillator (blue line).	119

5.11	(a) Time signals (b) Fourier spectra and (c) phase space reconstruction, of microfluidic time series for $V_{air} = 1.2$ ml/min, $V_{water} = 4.87$ ml/min (red line), and y-state variable of the Chua's oscillator (blue line).	120
5.12	(a) Time signals (b) Fourier spectra and (c) phase space reconstruction, of microfluidic time series for $V_{air} = 1.2$ ml/min, $V_{water} = 5.39$ ml/min (red line), and y-state variable of the Chua's oscillator (blue line).	121
5.13	α versus water flow rate.	121
5.14	β versus water flow rate.	122
5.15	γ versus water flow rate.	122
5.16	Histogram of the mean square error between microfluidic time series and the y state variable used as fitness fuction.	123
6.1	Block diagram of the thesis' subjects.	126